DEVELOPMENT OF HIGH STRENGTH Mg-Ni-Gd AND Mg-(Ni, Zn)-Gd-Li ALLOYS

A dissertation work

submitted in partial fulfillment of the requirements

for the award of the degree of

DOCTOR OF PHILOSOPHY

in

METALLURGICAL AND MATERIALS ENGINEERING

by

C. RAVIKANTH REDDY
(Roll No.715055)

Under the guidance of

Dr. BONTA SRINIVASA RAO

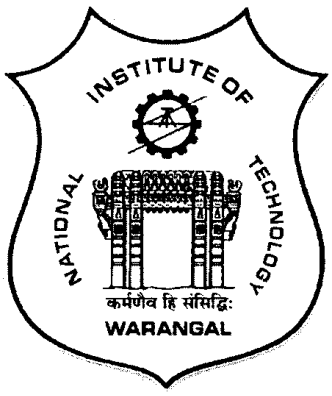

DEPARTMENT OF METALLURGICAL AND MATERIALS ENGINEERING
NATIONAL INSTITUTE OF TECHNOLOGY WARANGAL
JULY – 2023

To
My Family and Friends

Thesis Approval for Ph.D.

The thesis entitled **"Development of high strength Mg-Ni-Gd and Mg-(Ni,Zn)-Gd-Li alloys"** which is submitted by **Mr. C. Ravikanth Reddy (Roll No.715055)** is approved for the degree of **Doctor of Philosophy** in Metallurgical and Materials Engineering.

Examiner

_____

Supervisor

_____

Chairman

_____

Date: _____

DEPARTMENT OF METALLURGICAL AND MATERIALS ENGINEERING
NATIONAL INSTITUTE OF TECHNOLOGY
WARANGAL - 506 004 (T.S) INDIA

CERTIFICATE

This is to certify that the work presented in the thesis entitled **"Development of high strength Mg-Ni-Gd and Mg-(Ni,Zn)-Gd-Li alloys"** which is being submitted by **Mr. C. Ravikanth Reddy (Roll No.715055)** to National Institute of Technology Warangal in partial fulfilment of the requirements for the award of the degree of **Doctor of Philosophy** in **Metallurgical and Materials Engineering** is a bonafide work carried out under my supervision**.** To the best of our knowledge, the work incorporated in this thesis has not been submitted to any other university or institute for the award of any other degree or diploma.

Dr. Bonta Srinivasa Rao

Associate Professor and Thesis Supervisor
Department of Metallurgical and Materials Engineering
National Institute of Technology Warangal
Warangal-506 004

DECLARATION

This is to certify that the work presented in the thesis entitled **"Development of high strength Mg-Ni-Gd and Mg-(Ni, Zn)-Gd-Li alloys"** is a bonafide work done by me under the supervision of **Dr. Bonta Srinivasa Rao** and was not submitted elsewhere for the award of any degree. I declare that this written submission represents my ideas in my own words and where others' ideas or words have been included, I have adequately cited and referenced the original sources. I also declare that I have adhered to all principles of academic honesty and integrity and have not misrepresented or fabricated or falsified any idea / data / fact /source in my submission. I understand that any violation of the above will be a cause for disciplinary action by the Institute and can also evoke penal action from the sources which have thus not been properly cited or from whom proper permission has not been taken when needed.

(C. Ravikanth Reddy)

Acknowledgements

I take this opportunity to express my deep sense of gratitude and heartfelt thanks to my research supervisor **Dr. Bonta Srinivasa Rao**, Associate Professor, Department of Metallurgical and Materials Engineering, National Institute of Technology, Warangal for his wholehearted support, encouragement, guidance and patience during the research work. Without his untiring mentorship, constant inspiration, valuable discussions and suggestions, this thesis wouldn't have been possible. It was indeed a great honour and privilege to work under his supervision.

I am grateful to, **Prof. Bidyadhar Subudhi**, Director, NIT Warangal; **Prof. N.V. Ramana Rao** and **Prof. T. Srinivasa Rao,** former Directors, NIT Warangal for giving me an opportunity to carry out research work in the institute.

My sincere thanks and appreciation to the Doctoral Scrutiny Committee members, **Prof. T. Mahesh Kumar** (Chairman), **Dr. R. Arockia Kumar** (Associate professor), **Dr. Ajoy Kumar Pandey** (Associate professor), Department of Metallurgical and Materials Engineering, and **Prof. A. Kumar**, Department of Mechanical Engineering, NIT Warangal for their helpful suggestions, remarks and periodical review of my research progress.

I am thankful to **Dr. N. Kishore Babu**, Head of the department and **Prof. N. Narasaiah**, former Head of the Department, for his continuous encouragement, valuable advice and support. I would also like to express my gratefulness to **Prof. M. K. Mohan**, **Dr. C. Vanitha,** for their help in various ways during the research work. I sincerely acknowledge the financial support provided by the institute during the entire period of doctoral research study.

It is my privilege to express a sense of gratitude to **Mr. M. Ramakrishna, Dr. Koppoju Suresh**, scientists at ARCI, Hyderabad for allowing me to conduct FESEM characterization. **Mrs. Anjali and Mrs. Prasanthi**, Research scholars ARCI Hyderabad for helping me to carry out the experiments.

I would like to thank Mr. Jude Benedict from Fatima ITI, whose technical expertise made our experimental ideas feasible. I thank technical staff **Late Miss. G. Ramya**, for helping me to carryout Scanning Electron Microscopy analysis**.** I also thank **Mr. G. Savvaiah**, Mechanic A grade (Retired), **Mr. Fayaz**, **Mr. Nandu, Mr. G. Srinivasulu (XRD)** and other technical and office staff

of Metallurgical and Materials Engineering Department, NIT Warangal for their help during this research work.

I also wish to thank all my friends, especially to **Mr. Ashish Srivastav, Mr. Kiranchand, Dr. Sravan, Dr. Venkateswara Reddy**, **Mr. S. Siva Kumar**, **Dr. Harsha Praneeth, Dr. Umme Thahira Khatoon, Mr. Diwakar Nalam, Dr. E. Obulapathi, Mr. V. Ganesh, Mr. Vignesh, Dr. Siva Bejugama, Dr. Sai Mahesh, Dr. Raju, Dr. Katti Bharath, Dr. Bheekya Naik** and **Dr. Jyothi** for their pleasurable company, valuable assistance and tremendous moral support.

Finally, I express my profound gratitude to my family who were patient and supportive throughout my life.

(C. RAVIKANTH REDDY)

July 2023

Abstract

Mg-alloys, in spite of being the lightest structural metal, finds sparse industrial application due to low strength resulting from dismal values of critical resolved shear stress (CRSS) coupled with poor workability caused by its hcp structure devoid of sufficient independent slip systems. Grain refinement, alloying additions, and synthesizing composites aid in boosting mechanical properties. It is known that the Li addition to magnesium improves the formability of the alloy but at the cost of diminishing strength. The addition of transition elements along with rare earth elements formed a new type of phases called long period stacking ordered (LPSO) phases that effectively improved the strength without compromising the ductility of the alloys. Hence, in this thesis, efforts were made to synthesize low-density, high-strength, and ductile Mg-alloys using Li, Ni, Zn, and Gd as alloying elements via different processing routes, i.e., casting and powder metallurgy.

Ni and Gd were selected as alloying additions due to their prolificacy towards forming LPSO phases. The effect of Li on the microstructural and mechanical properties of Mg-0.5Ni-2.5Gd (at. %) alloy was studied by varying Li content, from 0-25 at.%. The alloys were processed through casting in vacuum induction melting furnace and then hot extruded. In as-cast state, a eutectic phase consisting of α-Mg and Mg_3Gd phase is present along the dendritic boundaries of α-Mg, Mg_3Gd, and LPSO phases. In addition, high Li-containing alloys such as 15 and 25 at. % Li alloys contain β-Li phase as well, and its volume fraction is a direct function of Li content. The volume fraction of the LPSO initially increases up to 5 at. % Li and subsequently reduces. Extrusion at 400 ℃ led to grain size refinement due to dynamic recrystallization, eliminating the dendritic and eutectic network and forming lamellar LPSO/ blocky LPSO and Mg_3Gd particles. High yield strength of 302 MPa, ultimate strength (UTS) of 347MPa, and 5% elongation was achieved in the 5 at. % Li alloy whereas a YS of 167 MPa, UTS of 188 MPa, and a tensile ductility of 37.5% were attained in 25Li alloy.

To further enhance the precipitation/formation of LPSO phases even at high Li contents of 15, 23, and 30 at. %, a small amount of Zn was added, which induced formation of lamellar LPSO phases in 15 and 23 at. % Li alloys, whereas some blocky LPSO phase fraction was observed in the 30 at. % Li alloy. The alloys were cast, and solutionized at 510 ℃ for 48 h, which increased the amount of the LPSO phase compared to the cast alloys. Hot extrusion at 200 or 300ºC led to

dynamic recrystallization of matrix grains and refinement and uniform distribution of LPSO and Mg_3Gd phases. A high UTS of 320 MPa and 18% elongation is attained with 15Li alloy extruded at 200 ℃. The alloys extruded at 200 ℃ performed better than the ones extruded at 300 ℃ due to the fine grain size and uniformly distributed second-phase particles. 30Li alloys exhibited initial strain hardening and after a critical amount, strain softening behavior at both the extrusion temperatures. This can be attributed to the dislocation annihilation by a dynamic recovery, owing to the presence of soft β-Li phase and lack of sufficient distribution of precipitates in the matrix.

This investigation aims to achieve a YS of >600 MPa for a magnesium alloy. Introducing thermally stable and coherent secondary phases would boost the strength at elevated temperatures. A master alloy comprised of Ni and Gd was cast, and the compositions of $Mg_{98.82}Ni_{0.59}Gd_{0.59}$ and $Mg_{97.56}Ni_{1.22}Gd_{1.22}$ (at. %) were formulated using ball milling for 150 hours. Consolidation through sintering with 5, 7, and 9 h of exposure at 550 ℃ and subsequent extrusion at 500 ℃ resulted in the formation of Mg_5Gd, Mg_2Ni, Gd_2O_3 and MgO phases. The extruded samples possessed a high strength of 804 MPa and 3.75% elongation which can be attributed to ultra-fine grains and dispersoid strengthening by homogeneously distributed second-phase particles in the 100–200 nm range.

The development of a high-specific strength Mg alloy has been attained via different processing routes and an exhaustive evaluation of the microstructure and mechanical properties has been carried out.

Keywords: Mg-Li alloys, hot extrusion, Mg-Ni-Gd, Mg_3Gd, LPSO phases, Dynamic recrystallization, high strength Mg alloys.

Index

LIST OF FIGURES

LIST OF TABLES

1

Introduction

1.1 Introduction

Magnesium is the sixth most abundant element, comprising 2% of the Earth's crust. It is the lightest structural metal known, with a 1.738 g/cm^3 density. Magnesium has limited ductility at room temperature because of its hexagonal close-packed structure with lattice parameters at 20 ℃ as a = 0.32 *nm*, c = 0.52 *nm*. In addition, pure magnesium doesn't have the necessary strength levels required for a majority of structural applications [1]. Hence, alloying additions were made to improve strength and tune ductility of these alloys. Magnesium alloys possess the least density (<1.8 g/cm^3) among all structural metals and alloys, superior specific strength and stiffness, exceptional dimensional stability, high damping capacity and high recycling ability [2,3]. Although magnesium-based alloys are extensively used in the cast form, most of the cast Mg-based alloys have lower specific strength and elongation to failure compared to aluminum alloys and steels [4-7]. On the other hand, some wrought Mg alloys exhibit higher specific strength and

elongation to failure values than these materials. In general, the strengths of typical Mg alloys that are candidates for structural applications are graphically presented vis-à-vis other structural alloys in **Figure 1.1** [7]. It has been observed that the strength and stiffness of Mg base alloys fall within similar ranges as that of conventional structural alloys. Owing to these special attributes and due to the fact that lightweight structures are desirable for fuel economy and lower emissions, the activities pertaining to the R&D of magnesium-based alloys have significantly risen worldwide in the last decade [8-10]. Magnesium based alloys are now deemed as significantly desirable materials in automobile, aircraft, and electronic consumer products [3]. In the automobile industry, magnesium alloys have been used for the inner door panels and seat frames [11]. Several other automotive firms use magnesium in varied parts of cars, from body frames to engine blocks to instrumental panels [12].

To further reduce the density, Mg-Li alloys were pioneered in the 1960s when NASA created multiple Mg-Li-Al (LA141 and LS141A) alloys in the form of sheets, extrusions, and castings, mainly for use in aerospace and military applications [13]. LA141A has been most successfully commercialized. The room temperature elastic modulus of LA141A is 42 GPa, and the density is only 1.35 g/cm^3. Mg-Li alloys possess greater formability and resistance to vibration when compared to commercially available wrought Mg-Al-Zn (AZ-series) alloys. The mechanical behavior of LA141A alloy leaves a lot to be desired, as evidenced by its low yield and tensile strength values. The casting of Mg-Li alloys is also a challenging task. The challenges arise from the high reactivity of Mg and extreme reactivity and volatility of Li, along with differences in melting point and density of Li, Mg, and other alloying additions. Several strategies have been used to achieve homogeneity [14]. Solid solution strengthening and precipitation hardening are instrumental in improving strength of Mg-Li alloys. Al (2.7 g/cm^3) and Zn (7.13 g/cm^3) are the most common alloying additions, and accordingly, Mg-Li-Al (LA-series), Mg-Li-Zn (LZ-series) and Mg-Li-Al-Zn (LAZ-series) alloys have been developed [15-18]. Several thermo-mechanical processes like hot extrusion have also been tried to improve the strength of these Mg-Li alloys [19-22].

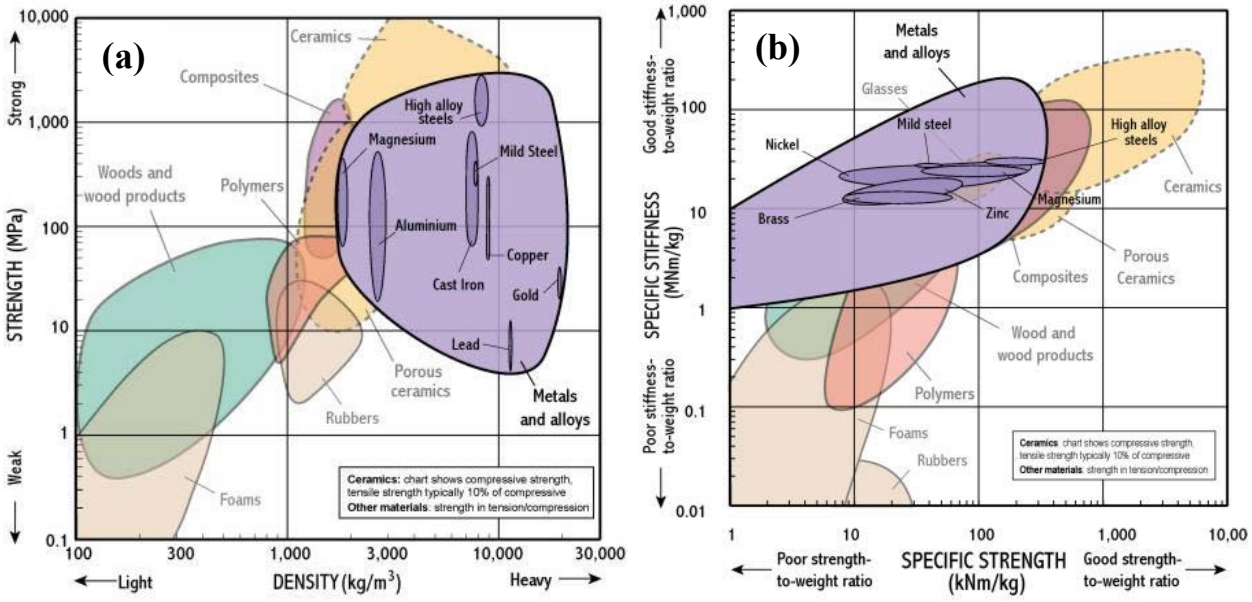

Figure 1.1 (a) strength vs density for different classes of materials. (b) Specific stiffness versus specific strength for different materials. [7].

The strategies to enhance mechanical properties of Mg-alloys involve by choosing a proper processing route and/or by choosing proper alloying elements or making composite materials. A plethora of processing routes have been adopted for producing magnesium-based alloys and composites. All these processes can be categorized into two primary approaches: solid state or powder metallurgical (PM) route and liquid phase or ingot metallurgical (IM) route. The choice of the desired processing route is crucial in deciding or manipulating the microstructures and the corresponding behavior of the resultant alloys or composites. Solid-phase approaches present more scope for refining characteristic microstructure, generating metastable phases, and developing high-strength materials than the liquid-phase processing routes.

Majority (>90%) of the magnesium alloy structural components are produced by the casting. The cast products, however, have their inherent shortcomings [5]. Apart from other factors, relatively coarse grains are the limiting factors in tailoring optimum properties in cast Mg alloys. In the conventional magnesium cast alloys, a grain size of the order of 50-200 μm could be obtained. There have been numerous investigations to overcome these limitations. Conventional processing techniques like rolling, extrusion, forging etc. could easily lead to grain sizes ~ 15-20 μm [23]. Owing to the importance of fine grain size, a parallel effort has been made by researchers working in the development of cast magnesium alloys by grain refining

agents, e.g., Zr, to reduce the grain size to a similar level [24]. However, wrought magnesium alloys witness a greater spectrum of applications than cast alloys of the same composition due to their high strength levels (**Figure 1.2**) [25]. It is now accepted that suitably processed wrought magnesium alloys display better properties than their cast counterparts. Moreover, there have been indications for further grain size reduction through modern wrought processing techniques. This has led to a spurt in research activities in the wrought processing of magnesium alloys, especially concerning grain size reduction [26-34].

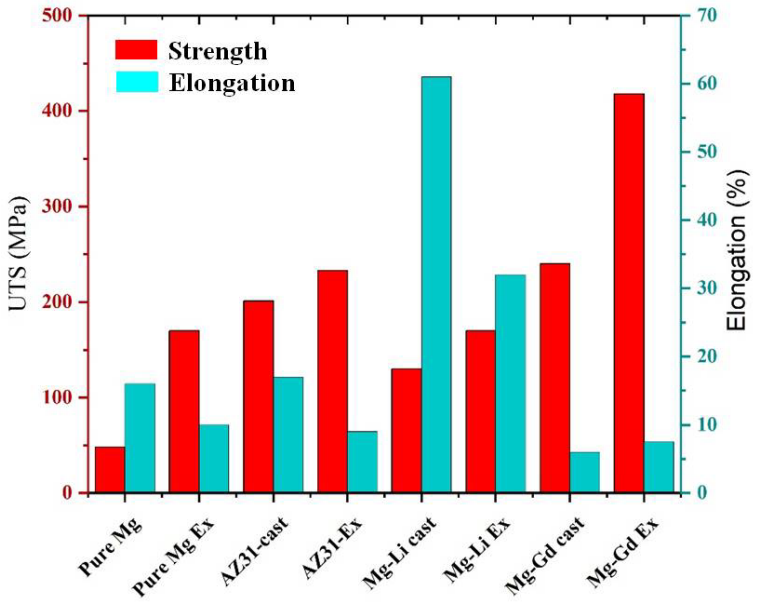

Figure 1.2 Mechanical property comparison between cast and wrought magnesium alloys

Addition of rare earth (RE) elements have been instrumental in weakening the texture and improving the deformability of Mg [35,36]. Moreover, the hard eutectic phases generated during casting and metastable phases induced by specific heat treatment procedures play a cardinal role in enhancing the strength of the alloy [37,38]. The increment in strength is generally attained through a solid solution strengthening mechanism coupled with a precipitation hardening mechanism [39,40]. These alloys in cast or wrought format do find use in niche areas of automotive industry [41,42]. The Mg-RE phase diagrams indicate that every single rare earth metal behaves differently when added as the dominant alloying element. Hence, several studies have been conducted to evaluate the influence of processing parameters and certain alloying

additions on microstructure and texture and their subsequent consequences with regards to the mechanical properties of such alloys [41-43].

One prominent milestone in understanding the strengthening mechanisms prevalent in Mg-based alloys is the discovery of a long-period stacking ordered (LPSO) structure, and it has received considerable attention as a new type of strengthening phase in high-strength Mg alloys. Kawamura *et al*. [44] reported an Mg-Zn-Y alloy with a high yield strength of 610 MPa and 6% elongation, ascribing the result to precipitation strengthening due to the formation of novel precipitates, i.e., LPSO phase and grain refinement. Subsequently, many investigations regarding the formation of these LPSO structures have been conducted on the Mg-Zn-RE (RE=Y, La, Ce, Pr, Sm, Nd, Dy, Ho, Er, Gd and Tm) alloys. Several types of LPSO structures, including 6H, 10H, 14H, 18R, and 24R [45], in these alloy systems were produced by different methods such as rapid solidification, powder metallurgy [44], melt spun [46,47], Cu-mold casting and induction melting [48] and conventional casting techniques. Similarly, replacing Zn with other transition metals (TM) such as Ni, Cu, and Co gave rise to these LPSO structures [49-51].

A combination of LPSO phase formation during casting or heat treatment and hot working operations improved the mechanical properties of these Mg-TM-RE alloys. Hot working operations such as hot extrusion processing resulted in the formation of a bimodal microstructure comprising of coarse deformed grains (Mg and LPSO) and sub-micron sized dynamically recrystallized (DRXed) grains, that possess a large number of secondary precipitates. The DRXed grains were located along the original grain boundaries. DRXed grains are also observed in the boundaries of the LPSO/Mg structure, where the boundary of the LPSO particles acts as a DRX nucleation site due to the stored high energy at the matrix and particle interface [52]. Processing parameters like temperature and extrusion ratio need to be optimized in order to achieve good grain refinement in these alloys.

1.2 Motivation of the present work

The primary goal of the present work is to develop a Mg alloy with a yield strength of 600 MPa or more. To achieve this goal, alloying elements (Ni, Zn, and Gd) are chosen to form the LPSO phase while processing and the resultant LPSO phase is also resistant to growth at higher temperatures due to sluggish diffusion. The mechanical properties can be improved by dispersion of secondary phases like Mg_3Gd and LPSO phases. Gadolinium and Nickel are added

to form LPSO phases that assured strength and ductility. Zinc is a suitable alloying element for enhancing the percentage of LPSO phase and facilitates their formation through solutionizing and aging heat treatment. Since the densities of these alloying elements are high, there is an increase in the overall density of the material. In order to reduce the density and also to impart sufficient ductility to the resultant alloys, Li has been chosen as one of the major alloying elements. Depending on the amount of Li, the microstructure changes from α-Mg, dual-phase microstructure (α-Mg & soft β-Li), and β-Li [53]. The presence of β-Li increases ductility greatly. Both casting and powder metallurgy routes are explored. Since Li content affects the strength and significantly improves the ductility of the Mg alloys, the processing and optimization of Mg-Li alloys is pursued through the casting route. The wrought Mg-Li-based alloys with improved strength and ductility through the casting process and high-strength Mg composite through mechanical alloying (powder metallurgy) are investigated through this work. The path to achieving the primary goal of yield strength >600 MPa has been structured into three following objectives.

1. To study the effect of Li on the formation of LPSO phases and the resultant mechanical properties of the alloy system Mg-0.5Ni-2.5Gd-xLi (0, 1, 5, 10, 15 and 25 at. %).
2. To study the microstructure and mechanical properties of Mg-0.5Ni-0.5Zn-2Gd-xLi (15, 23 and 30 at. %) alloys prepared by casting and extrusion processes.
3. To develop a high-strength Mg-Ni-Gd alloy through a powder metallurgy route.

1.3 Organization of the thesis

Chapter 1 gives a brief introduction of the thesis and the objectives. **Chapter 2** provides a detailed overview of the Mg alloys in relation to the effect of alloying elements and processing routes on the evolution of microstructure and mechanical properties. This chapter also discusses the previous works on the relevant Mg alloy systems, new phases that aid in their improvement of strength and ductility. Finally, concludes with the scope of work envisioned from the gaps in the literature for this thesis.

Chapter 3 describes the experimental procedure used in the thesis. Initially, the preparation of master alloy NiGd through Vacuum Arc Re-melting furnace was described, which is followed by the preparation of molten melts and casting of Mg-0.5Ni-2.5Gd-xLi (x = 0, 1, 5,

10, 15 and 25 at. %) and Mg-0.5Ni-0.5Zn-2Gd-xLi (x = 15, 23, and 30 at. %) alloys using Vacuum Induction melting furnace. Some of the alloys were vacuum sealed under argon atmosphere and solutionized at high temperatures. The cast or solutionized samples were subsequently hot extruded at various temperatures using a high-strength die steel and at an extrusion ratio of 16:1 using a hydraulic press. Also, two Mg-Ni-Gd alloys were prepared by powder processing route, where Mg powder and NiGd intermetallics were milled using a planetary ball mill to reduce the crystallite size to nanometer levels. Subsequently, the powders were consolidated using a hot compression machine at high temperature for various holding times and thereafter hot extruded at 500 ℃ to achieve a good dense material. Phase analysis was carried out using X-Ray Diffraction technique and microstructural characterization was performed using Scanning Electron Microscope and Transmission Electron Microscopy techniques. The densities of the hot extruded alloys were measured using Archimedes principle. Finally, the mechanical properties were measured using Vickers hardness and tension/compression tests.

The low density of Mg-Li alloys shows considerable promise for different applications in the automotive and aerospace industry. However, the major challenge is improving these alloys' strength by suitable addition of alloying elements and achieving the desired microstructure (LPSO phases in the current study). Achieving uniform composition is also challenging due to the difference in the densities of different alloying elements and due to the difference in the melting points. Therefore, low melting NiGd intermetallic, Pure Mg, Li, and Gd has been used to prepare the Mg-0.5Ni-2Gd-xLi (x = 0, 1, 5, 10, 15 and 25 at. %) alloys using vacuum induction melting furnace. Accordingly, **Chapter 4** discusses the processing of these alloys by vacuum induction melting furnace and subsequently by hot extrusion technique to remove the casting defects such as casting porosity. The effect of Li content on the evolution of LPSO phases and dynamic recrystallization of matrix grains were thoroughly analyzed using a scanning electron microscope and transmission electron microscopy. The densities and mechanical properties of the alloys were carried out to understand the relation between the microstructure and mechanical properties.

Formation and uniform dispersion of lamellar or particles of LPSO phase in the matrix is very much essential to increase the strength by precipitation hardening or dispersion

strengthening to achieve enhanced properties. Since Zn was found to be a good alloying element that will promote the LPSO formation by suitable heat treatment, 0.5 at. % Zn was added to the high Li containing Mg-0.5Ni-2Gd-xLi (x= 15, 23 and 30 at. %) alloys. **Chapter 5** describes the effect of solutionizing treatment and subsequent hot extrusion at different temperatures on the evolution of microstructure. Detailed microstructural analysis was conducted to understand the type, size, shape, and distribution of secondary phase particles and their impact on mechanical properties.

One of the problems with the casting and hot working route is that it is very difficult to achieve nano-grain structure in the final alloys. The grains tend to grow at high-temperature processing to reduce the grain boundary energy. One of the ways to achieve the nanostructure is by processing the alloys through the powder metallurgy route. Since Li is very difficult to process due to its volatility and reactivity, only Mg-Ni-Gd alloys were prepared by mechanical alloying and subsequent consolidation. Hence, **Chapter 6** discusses the development of high-strength Mg-Ni-Gd alloys through mechanical alloying, consolidation of powders using hot compression under vacuum at high temperatures for various times, and subsequent processing by hot extrusion at elevated temperatures. 5 mm rods were successfully produced by optimizing the process parameters and the microstructure and mechanical properties were evaluated in detail.

The present work has resulted in the development of high-strength Mg-Li alloys and Mg-Ni-Gd alloys, which have been analyzed in considerable detail. The major conclusions are summarized in **Chapter 7**, along with the plan for future work is also presented.

References:

[1] Polmear, I. J. "Magnesium alloys and applications." *Materials science and technology* 10.1 (1994): 1-16.

[2] Kainer, Karl U., ed. *Magnesium alloys and technology*. John Wiley & Sons, 2003.

[3] Edgar, R. L. "Magnesium alloys and their application." *KU Kainer Pub., France* 3.8 (2000).

[4] Mukai, Toshiji, et al. "Ductility enhancement in AZ31 magnesium alloy by controlling its grain structure." *Scripta materialia* 45.1 (2001): 89-94.

[5] Baker, Hugh. *ASM specialty handbook: magnesium and magnesium alloys*. Ed. Michael M. Avedesian. Vol. 274. Materials Park, OH: ASM international, 1999.

[6] Mukai, T., et al. "Experimental study of a structural magnesium alloy with high absorption energy under dynamic loading." *Scripta materialia* 39.9 (1998): 1249-1253.

[7] Polmear, Ian, et al. *Light alloys: metallurgy of the light metals*. Butterworth-Heinemann, 2017.

[8] Hai, D. V., et al. Finite Element Simulation of Sheet Forming Process for Magnesium Wrought Alloys. *Advanced Materials Research*, *11*, (2006): 413-416.

[9] Aghion, E., et al. "The art of developing new magnesium alloys for high temperature applications." *Materials Science Forum*. Vol. 419. Trans Tech Publications Ltd, 2003.

[10] Mordike, B. L., and T. Ebert. "x201C; Magnesium: Properties-Applications-Potential&# x201D." *Mater. Sci. Eng. A* 302 (2001).

[11] Monteiro, W. A., S. J. Buso, and L. V. Silva. "Application of magnesium alloys in transport." *New features on magnesium alloys* (2012): 1-14.

[12] Alves, H., et al. "Environmental behavior of magnesium and magnesium alloysd." *Materials Technology* 16.2 (2001): 110-126.

[13] Prabhu, T. Ram, Srikanth Vedantam, and Vijaya Singh. "Magnesium alloys." *Aerospace Materials and Material Technologies: Volume 1: Aerospace Materials* (2016): 1

[14] Maria J. Balart, Jayesh B. Patel, Zhongyun Fan, "Melt protection of Mg-Al based alloys", Metals, Vol. 6, 2016, pp. 131

[15] Dong, Hanwu, et al. "Evolution of microstructure and mechanical properties of a duplex Mg–Li alloy under extrusion with an increasing ratio." *Materials & Design* 57 (2014): 121-127.

[16] Meng, Xiangrui, et al. "Microstructures and properties of superlight Mg–Li–Al–Zn wrought alloys." *Journal of alloys and compounds* 486.1-2 (2009): 722-725.

[17] Zou, Yun, et al. "Improvement of mechanical behaviors of a superlight Mg-Li base alloy by duplex phases and fine precipitates." *Journal of Alloys and Compounds* 735 (2018): 2625-2633.

[18] Wei, Zhen, et al. "Achieving high strength in a Mg–Li–Zn–Y alloy by α-Mg precipitation." *Materials Science and Engineering: A* 846 (2022): 143272.

[19] Zhou, Gang, et al. "Microstructure and strengthening mechanism of hot-extruded ultralight Mg-Li-Al-Sn alloys with high strength." *Journal of Materials Science & Technology* 103 (2022): 186-196.

[20] Li, Xiaoqiang, et al. "Reducing the yield asymmetry in Mg-5Li-3Al-2Zn alloy by hot-extrusion and multi-pass rolling." *Journal of Magnesium and Alloys* 9.3 (2021): 937-949.

[21] Zhang, Yang, et al. "Microstructure and tensile properties of as-extruded Mg–Li–Zn–Gd alloys reinforced with icosahedral quasicrystal phase." *Materials & Design (1980-2015)* 66 (2015): 162-168

[22] Zeng, Zhuoran, et al. "Magnesium extrusion alloys: a review of developments and prospects." *International Materials Reviews* 64.1 (2019): 27-62.

[23] Agnew, S. R., and J. A. Horton. "TM lillo, DW Brown, Enhanced ductility in strongly textured magnesium produced by equal channel angular processing." *Scr. Mater* 50 (2004): 377-381.

[24] Wang, S. C., and C. P. Chou. "Effect of adding Sc and Zr on grain refinement and ductility of AZ31 magnesium alloy." *Journal of Materials Processing Technology* 197.1-3 (2008): 116-121.

[25] Pérez-Prado, María Teresa, J. A. Del Valle, and Oscar Antonio Ruano. "Achieving high strength in commercial Mg cast alloys through large strain rolling." *Materials letters* 59.26 (2005): 3299-3303.

[26] Yang, Zhong, et al. "Review on research and development of magnesium alloys." *Acta Metallurgica Sinica* 5.21 (2008): 313-328.

[27] Kettner, Michael, et al. "The InnMag Project–Processing Mg for Civil Aircraft Application." *Advanced Engineering Materials* 9.9 (2007): 813-819.

[28] Bohlen, Jan, Dietmar Letzig, and Karl Ulrich Kainer. "New perspectives for wrought magnesium alloys." *Materials Science Forum*. Vol. 546. Trans Tech Publications Ltd, 2007.

[29] Luo, Alan A., Anil K. Sachdev, and Diran Apelian. "Alloy development and process innovations for light metals casting." *Journal of Materials Processing Technology* 306 (2022): 117606.

[30] Gardinger, R., and P. Stolfig. "Magnesium Technology 2003." (2003): 231.

[31] Slooff, F. A., et al. "Constitutive analysis of wrought magnesium alloy Mg–Al4–Zn1." *Scripta Materialia* 57.8 (2007): 759-762.

[32] Wu, L., et al. "Twinning–detwinning behavior during the strain-controlled low-cycle fatigue testing of a wrought magnesium alloy, ZK60A." *Acta materialia* 56.4 (2008): 688-695.

[33] Ben-Hamu, G., D. Eliezer, and K. S. Shin. "The role of Si and Ca on new wrought Mg–Zn–Mn based alloy." *Materials Science and Engineering: A* 447.1-2 (2007): 35-43.

[34] Riemelmoser, Franz O., et al. "Micro-Alloyed Wrought Magnesium for Room-Temperature Forming." *Advanced Engineering Materials* 9.9 (2007): 799-802.

[35] Matsuda, M., et al. "Variation of long-period stacking order structures in rapidly solidified Mg97Zn1Y2 alloy." *Materials Science and Engineering: A* 393.1-2 (2005): 269-274.

[36] Inoue, Akihisa, et al. "Novel hexagonal structure of ultra-high strength magnesium-based alloys." *Materials Transactions*43.3 (2002): 580-584.

[37] Gao, Yan, et al. "Comparison of microstructure in Mg–10Y–5Gd–0.5 Zr and Mg–10Y–5Gd–2Zn–0.5 Zr alloys by conventional casting." *Journal of Alloys and Compounds*477.1-2 (2009): 374-378.

[38] Yamada, Kentaro, et al. "Alloy development of high toughness Mg-Gd-Y-Zn-Zr alloys." *Materials transactions* 47.4 (2006): 1066-1070.

[39] Apps, P. J., et al. "Precipitation reactions in magnesium-rare earth alloys containing yttrium, gadolinium or dysprosium." *Scripta Materialia* 48.8 (2003): 1023-1028.

[40] Nie, J. F., and B. C. Muddle. "Characterisation of strengthening precipitate phases in a Mg–Y–Nd alloy." *Acta Materialia* 48.8 (2000): 1691-1703.

[41] Chino, Yasumasa, et al. "Novel equilibrium two phase Mg alloy with the long-period ordered structure." *Scripta materialia* 51.7 (2004): 711-714.

[42] Zhu, Y. M., A. J. Morton, and J. F. Nie. "The 18R and 14H long-period stacking ordered structures in Mg–Y–Zn alloys." *Acta Materialia* 58.8 (2010): 2936-2947.

[43] Itoi, T., et al. "A high-strength Mg–Ni–Y alloy sheet with a long-period ordered phase prepared by hot-rolling." *Scripta materialia* 59.10 (2008): 1155-1158.

[44] Kawamura, Yoshihito, et al. "Rapidly solidified powder metallurgy Mg97Zn1Y2Alloys with excellent tensile yield strength above 600 MPa." *Materials Transactions* 42.7 (2001): 1172-1176..

[45] Abe, E., et al. "Long-period ordered structure in a high-strength nanocrystalline Mg-1 at% Zn-2 at% Y alloy studied by atomic-resolution Z-contrast STEM." *Acta Materialia* 50.15 (2002): 3845-3857.

[46] Matsuda, M., et al. "Variation of long-period stacking order structures in rapidly solidified Mg97Zn1Y2 alloy." *Materials Science and Engineering: A* 393.1-2 (2005): 269-274.

[47] Amiya, Kenji, Tetsu Ohsuna, and Akihisa Inoue. "Long-period hexagonal structures in melt-spun Mg97Ln2Zn1 (Ln = lanthanide metal) alloys." *Materials Transactions* 44.10 (2003): 2151-2156..

[48] Zhu, Y. M., Allan James Morton, and J. F. Nie. "The 18R and 14H long-period stacking ordered structures in Mg–Y–Zn alloys." *Acta Materialia* 58.8 (2010): 2936-2947.

[49] Leng, Zhe, et al. "Microstructure and mechanical properties of Mg–9RY–4Cu alloy with long period stacking ordered phase." *Materials Science and Engineering: A* 580 (2013): 196-201.

[50] Mi, Shao-Bo, and Qian-Qian Jin. "New polytypes of long-period stacking ordered structures in Mg–Co–Y alloys." *Scripta Materialia* 68.8 (2013): 635-638.

[51] Pérez, Pablo, et al. "Development of high strength alloys in the Mg-Ni-Y-RE system." *Materials Science Forum*. Vol. 567. Trans Tech Publications Ltd, 2008

[52] Yu, Zijian, et al. "Microstructural evolution and mechanical properties of Mg–11Gd–4.5 Y–1Nd–1.5 Zn–0.5 Zr alloy prepared via pre-ageing and hot extrusion." *Materials Science and Engineering: A* 624 (2015): 23-31.

[53] A.A. Nayeb-Hashemi, J.B. Clark, and A.D. Pelton, The Li-Mg (Lithium-Magnesium) System, *Bull. Alloy Phase Diagrams*, 1984, 5(4), p 365–374.

2

Review of Literature

2.1 General Background of Magnesium:

The lightweight feature of magnesium renders it a promising starting material for developing novel alloys with a high strength-to-weight ratio. The average density of 1,740 kg/m^3 as possessed by the magnesium alloys is lower than that of aluminum alloys by 36%. Also, Young's modulus of 45 GPa is much less than that of aluminum alloys by about 65%; hence they are mechanically more viable than Aluminium alloys to fabricate lightweight components [1]. Various studies point towards the fact that the overall weight savings that could be attained by using Mg-based materials in place of Al-based ones would result in fuel savings of around 20–30 % without any apparent changes in design. Due to its unique features of strength, bioactivity and biocompatibility, and non-toxicity, magnesium has been deemed as a magic material for use in biomedical applications; however, its extensive use is impeded by its high reactivity.

The element magnesium is the second member of the alkaline earth metals and has been said to possess a holohedral hexagonal arrangement with an axial ratio of 1.64 [2]. The hexagonal structure imparts limited ductility and minimal formability at ambient temperatures, consequently impeding the usage of magnesium wrought products. The crystal structure also causes the mechanical behaviour of magnesium components to be highly directional. In other words, they exhibit mechanical anisotropy due to different critical resolved shear stress (CRSS) values of various slip systems and due to their limited number. In crystalline materials, the formability of a material is attributed to the number of active slip systems; thermally activating additional slip planes is the most widespread approach for improving the deformability of a material. Hence, hot working is preferred for inducing higher ductility and malleability in magnesium based alloys as a result of the activation of additional slip systems by reduction of CRSS values of the slip systems at high temperatures.

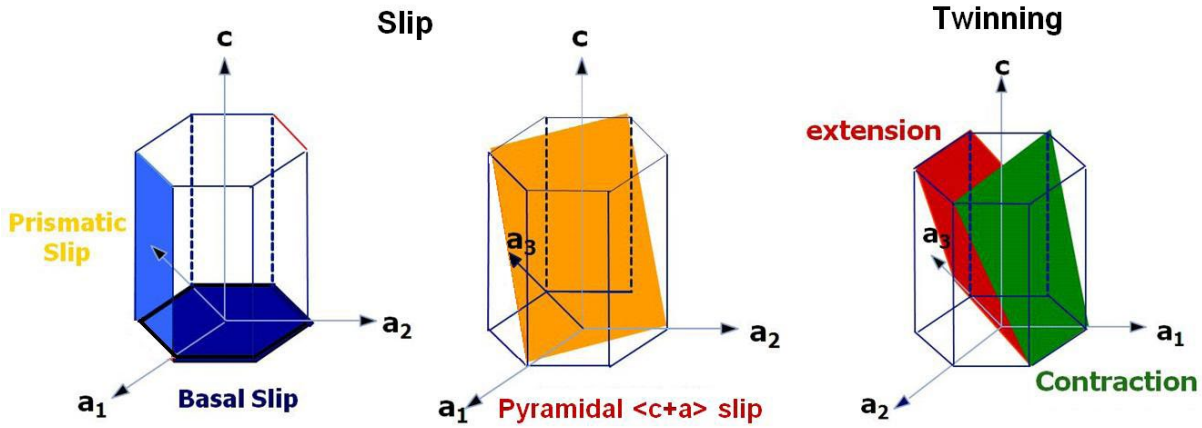

Figure 2.1. Schematic representation of deformations systems in HCP [3].

Recently, the focus has shifted to developing lightweight materials having multiple properties, including ambient and high-temperature strength, good formability, and creep. To achieve these properties, several strategies such as grain size reduction, controlling the defects (such as stacking faults & twins, etc.), alloying element additions, precipitation of new phases, and by introducing ceramic/carbon/ separate master alloy-based hard reinforcing phases/particles resulting in metal matrix composites by incorporating superior strength and rigidity of the reinforcement [4]. The induction of such particles or phases in the metal matrix facilitates the attainment of superlative mechanical performance while at the same time ensuring isotropic

behaviour (in some instances) via simple production techniques. When the size of the reinforced particles was in the micron scale, several demerits surfaced, the prominent among them being the reduced ductility and toughness when compared to the unreinforced matrix and excessive tool wear while machining. These demerits were successfully countered by reducing the size of the reinforced phases to nano-scale, thereby giving birth to a new class of composites, namely, the metal matrix nanocomposites, which possess higher strength and hardness along with superior ductility and toughness at both ambient and elevated temperatures as compared to their counterparts with micron-scale reinforcements [5]. The most prominent merit of such nano-composites is that the improvement in mechanical behaviour can be achieved by lesser composition (<3 %) of reinforcements, as compared to that for micron-scale particle reinforced composites (>>10 %) [6].

2.2 Methods to enhance the strength of Mg alloys:

The following paragraphs elucidate the various strengthening mechanisms at play in strengthening the Magnesium alloys.

2.2.1 Orowan strengthening:

Closely spaced hard particles/phases dispersed in the matrix hinder the motion of dislocations. In micron-sized secondary phase-reinforced alloys, Orowan strengthening is limited due to coarse reinforcement particles and large inter-particle spacing [7]. In cast alloys with reinforcement phases/particles of 5 μm or more, Orowan strengthening is secondary [8]. The Orowan mechanism is the most prominent strengthening mechanism in composites with highly dispersed fine particles [9]. The presence of uniformly dispersed ultrafine insoluble particles can significantly boost creep resistance, albeit for a volume percent as less as 1 %, as a result of the Orowan bowing mechanism, resulting in the formation of dislocation loops which can be attributed to the presence of nano-scale dispersoids as dislocation lines pass across the obstacles [10]. The increase in the critical resolved shear stress (CRSS) of a slip system due to dispersoids is given by

$$\Delta\tau = \frac{1}{2\pi\,\lambda\sqrt{1-\upsilon}}\,ln\,\frac{d_p}{r_0} \qquad \text{(Eq. 2.1)}$$

Where, Δτ is the increase in CRSS of the selected slip system due to precipitation strengthening,

ν, the Poisson ratio,

λ, the effective planar inter-particle spacing,

d_p, the mean planar diameter of the precipitate,

2.2.2 Enhanced dislocation density:

Matrix and reinforcement phases being different compositions possess distinct coefficients of thermal expansion; subsequently, it gives rise to thermal stresses in the vicinity of particles during thermal processing, which is capable of causing plastic deformation, generally at the interface, thereby increasing the density of dislocations in the region [11]. The mismatch in the elastic modulus and work hardening during deformation of the matrix and secondary phase acts as another source of plastic strain and the consequent boost in number density of dislocations [12].

With respect to the load bearing effect, the adhesion at the matrix-reinforcement interface causes the load on the matrix to be shared with the reinforcement, thereby improving the load-bearing capacity of the material. Yield stress (σ) that results from dislocation forest strengthening according to the Taylor hardening law, can be presented as follows [13]:

$$\sigma = M\alpha\mu b\sqrt{\rho} \qquad \text{(Eq. 2.2)}$$

Where, M = Taylor factor

α = Empirical Constant for Cell-forming dislocation distribution

μ = Shear Modulus

b = Burgers Vector

ρ = dislocation density

2.2.3 Grain refinement:

Reinforced nanoparticles, on being added to a molten matrix, can give rise to highly refined and equiaxed microstructure, acting as initiation points for heterogeneous nucleation. Habibnejad- orayem et al., [14] in one of his works has concluded that, during the recrystallization process, the mobility of thermally activated grain boundaries is impeded by the nanoparticles, which is also termed as the nanoparticles pinning effect.

$$\sigma_y = \sigma_{y0} + \frac{k}{\sqrt{d}} \qquad \text{(Eq. 2.3)}$$

Where, σ_y = Yield Stress

σ_{y0}= Friction Stress

d = average grain size

k = Constant (Locking Parameter)

Moreover, the plastic deformation of Mg-based materials is also affected by texture (orientation of crystallites). Gradation in texture as a result of the addition of nanoparticles activates the non-basal slip planes, which in turn enhances the ductility and strength [15]. The various deformation modes that a material is susceptible to are activated as per the critically resolved shear stress, which depends upon the Schmid Factor, which subsequently is determined by texture within the bulk of the material. [16]. The crystal texture is subject to change when casting, deformation, welding, and heat treatments are being carried out on the material. In Mg-castings, all possible textures occur with equal frequency, whereby random crystal orientation occurs, resulting in the overall isotropic behaviour of the material [17]. As far as wrought Mg-based materials are concerned, highly ordered texture evolution is observed, which causes the material to behave anisotropically [18]. An optimal texture development can ensure appreciable room temperature deformation characteristics.

2.2.4 Alloying:

2.2.4.1 Long Period Stacking Ordered Phases (LPSO):

A substantially influential event concerning the knowledge of the strengthening mechanisms prevalent in Magnesium alloys is the discovery of the long-period stacking ordered (LPSO) structure. This secondary phase is solely responsible for the combination of superior mechanical properties, including high strength along with ductility. In the early 2000s, Kawamura et al. [19] put forward a study showing that YS of 610 MPa and ductility of 6% for an Mg alloy could be achieved by warm extrusion of helium atomized powders at 573 K having grain sizes ranging from 100 nm–150 nm. Their detailed study points towards the fact that a hitherto unexplored phase termed the LPSO has aided in precipitation strengthening of the alloys, which in turn translates into exceptional mechanical properties [20]. The earliest reports of the LPSO phase in Magnesium alloys were published by Luo et al. [21] They reported the presence of an X-phase in Mg-Zn-Zr-RE cast alloys, having an 18R structure. Using X-ray diffraction and HRTEM, they concluded that the 18R structure had a lattice parameter of 4.68 nm with an arrangement of ABABCACACABCBCBCABA.

Most researchers have made common observations pertaining to the preferential nucleation of LPSO phases along grain boundaries. Formation of LPSO is associated with the diffusion transformation of solute atoms (like Y and Zn) and the eventual growth into the interior of the grain along the basal plane. [22]. LPSO hence is not just ordered structurally but also chemically. LPSO structure formation is likely to be affected significantly by both heat treatment and the nature of solute atoms, specifically the atomic radii and the mixing enthalpies of the atom pairs. It has also been noted that the processing route and temperature play a significant role in forming the LPSO phases. For example, Nishida et al. [23] had noted in one of his articles that the 6H LPSO phase found to exist in the rapidly solidified ribbon annealed up to 773 K, was not found to occur in the rapidly solidified powders of $Mg_{97}Zn_1Y_2$ alloy annealed at 823 K.

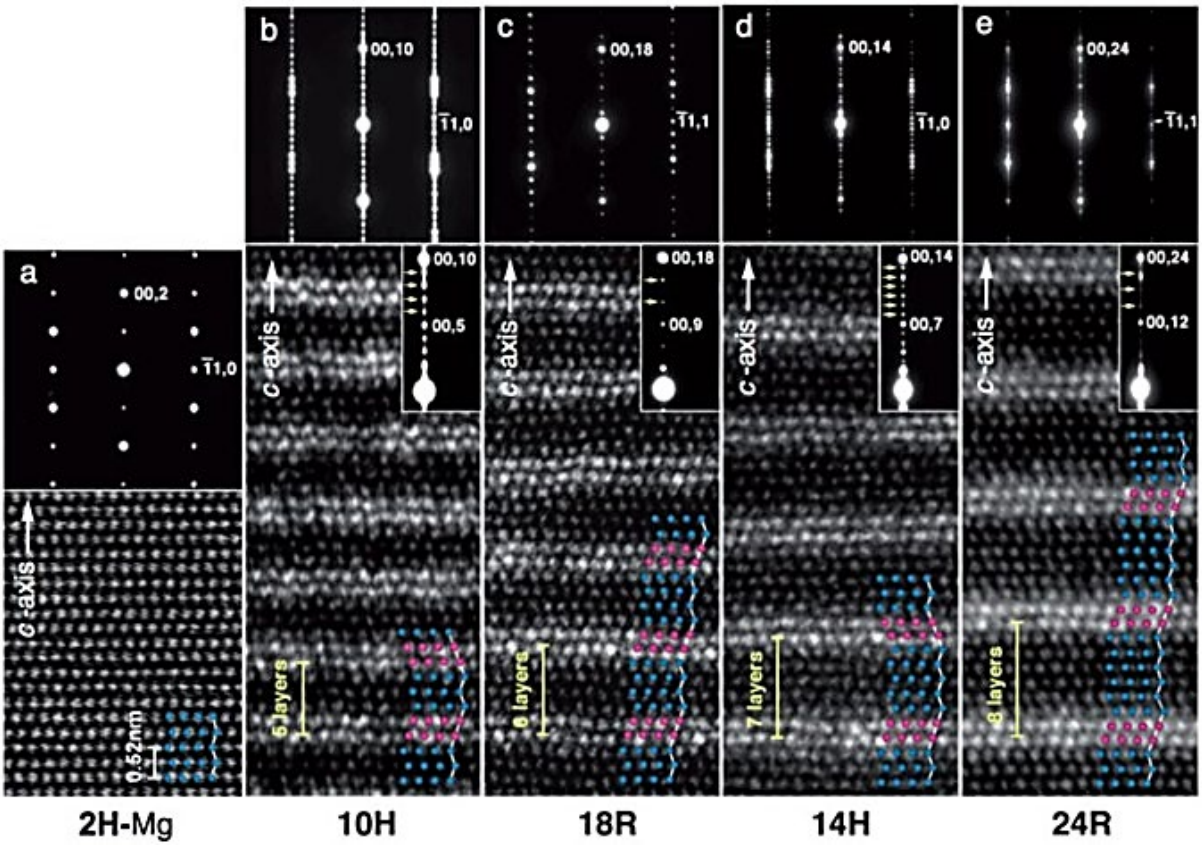

Figure 2.2 Electron Diffraction patterns of different types of LPSO phases [24].

Multiple varieties of LPSO Phases were segregated depending on the alloying elements, processing routes and heat treatment temperatures [25]. LPSO faults were found to be prevalent in a multitude of Mg–XL– XS systems, comprising Mg, a larger alloying element XL (Y, Gd, Tb, Dy, Ho, Er, Tm), and a smaller alloying element XS (Zn, Al, Cu, Co, Ni) [26]. The 18R structure with rhombohedral structure and 18 layers per periodic unit is initially formed. After annealing, the 18R structure transforms into the 14 H structure with hexagonal symmetry [27]. The complete structures of these phases were inferred quite recently, first by Zhu et al., for Mg–Y–Zn [28], and second, by Egusa and Abe, in the case of Mg–Y–Zn and Mg–Er–Zn ternary systems [29], possessed binary Mg–XL planes adjacent to ternary face centred Mg-Y-Zn planes, with a gradual variation in constitution along the c-axis. The 14H and 18R LPSO phases differ from each other in terms of the number of hexagonal magnesium planes; it has five hcp-magnesium planes, while 18R was found to have four.

The LPSO structures prevalently found in the alloys belonging to the Mg–Y–Zn system fall under five categories: 6H, 10H, 14H, 18R and 24R. Among this, the 6H structure is generated during rapid solidification. The LPSO phases found in Mg–Y–Zn alloys fall under the classification of multi-stacking fault structures comprised of basal stacking faults. The various LPSO phases and their stacking variations have been enumerated and listed out in Table 2.1.

Table 2.1 Types of LPSO phases categorised based on stacking order.

LPSO Structure	**Types of Stacking**	**Designation**
6H	ABCBCB	6H1
	ABACAB	6H2
10H [32]	ABACBCBCAB	
14H [32]	ACBCBABABABCBC	14H1
	ABABABACBCBCBC	14H2
	ABABABACACACAC	14H3
	ABACBCBCBCABAB	14H4
	ABABCACACACBAB	14H5
18R	ACBCBCBACACACBABAB	18R1 [30]
	ABABABCACACABCBCBC	18R2 [31]
24R	ABABABABCACACACABCBCBCBC	

From the literature, it can be inferred that Zn turns out to be an indispensable element for forming LPSO in Mg-RE alloy systems. Inoue et al., [33] noted the absence of LPSO in the melt-spun alloys in Mg-Al-Y, Mg-Y and Mg-Zn alloys, but adding Zn into Mg-Y results in the formation of 6H LPSO fault. This phenomenon was explained by Gao et al., [34] as resulting from the lack of stacking faults in alloys. Yamada et al., [35] stated that LPSO phases occurred in Mg-Gd-Y-Zn-Zr alloys only for Zn addition in the range of 0.3 wt.% to 1.0 wt.%.

Researchers investigating Zn-free systems like Mg-Dy-Nd and Mg-Gd-Nd could not verify the occurrence of LPSO phases during any precipitation sequences [36,37] thereby implying that the presence of Zn and Rare earth is a prerequisite for the formation of LPSO. However, very few ternary systems like Mg-Y-Cu [38] and Mg-Y-Ni [39], were found to have

LPSO phases and can be attributed to the size of the substituted atom. In the Mg-Y-Cu system, the atomic size of Cu is close to that of Zn, and in Mg-Y-Ni, the atomic radius of Ni is larger than Zn but is still lower than that of Yttrium. Moreover, the enthalpies of mixing for every atomic pair in Mg-RE, Zn-RE and substituting elements Cu-RE and Ni-RE are negative, resulting in the generation of LPSO structures [40].

In yet another work, Hagihara et al., [41] has observed the LPSO phase in $Mg_{97}Zn_1Y_2$ extruded alloy with superior mechanical properties. Grain-boundary strengthening due to the highly refined Mg-matrix phase and fiber-like reinforcement provided by the LPSO phase is primarily responsible for the alloy's high strength at room temperature and was noted to be effective even at 200ºC, thereby maintaining the high values of strength even at elevated temperatures. However, the alloy's yield stress experiences a dip at 300ºC, which can be explained by the increased operation frequency of non-basal slip in the magnesium-matrix grains. A few researchers have surmised that the $Mg_{97}Y_2Zn_1$ (at. %) alloy resembles a metal matrix composite wherein LPSO reinforces the matrix [42]. The LPSO phase was found to have a higher Young's modulus of 67 GPa compared to that of the magnesium matrix with a corresponding figure of 40 GPa [43]. Unlike magnesium grains, the LPSO phase behaves linearly in the elastic domain. Post yield, it was noted that the internal strain rises compared even with the {1010} and {1120} planes, thereby proving that the LPSO is subjected to a higher load than the applied stress. It reconfirms the assumption that a fraction of the load on magnesium grains is transferred to the LPSO, specifically from 250 to 350 MPa, owing to its comparatively higher Young's modulus. Above 350 MPa, the capacity of the LPSO to carry the load transferred by the magnesium matrix experiences a decline which can be attributed to the subsequent fragmentation of the LPSO resulting in its disintegration.

The inelastic deformation of $Mg_{12}ZnY$ processed via directional solidification encompassing an 18R LPSO structure was researched by Hagihara et al., [44]. The (0001) <1120> basal slip with a CRSS of 10–30 MPa was deemed to be dominant for deformation. Ingots of $Mg_{88}Zn_5Y_7$ (at %) were produced via vacuum induction melting in graphite crucibles. Rectangular specimens of 2x2x5 mm dimensions were cut by EDM. The transformation of LPSO from 18R to 14H was not confirmed in the directionally solidified crystals when annealed below 450 ºC for 3 h. The LPSO grains in directionally solidified alloy possess plate-like shapes.

They are around 100 mm in thickness and possesses a length of about a few millimetres. Along the longitudinal section, the plate-like grains were aligned along the growth direction, whereas, in the transverse section, the grains were randomly distributed. Small amounts of $Mg_3Zn_3Y_2$, or W-phase as the second phase, were formed along the grain boundaries of LPSO. The (0001) <1120> basal slip has been deemed to be the dominant deformation mode in LPSO. Recently, Itoi et al. reported the development of Mg–TM–Y alloys (TM = Cu or Ni) with LPSO structures and exhibiting superior mechanical properties [45]. Structural characterization confirmed the presence of a couple of LPSO phases: 18R and 14H [46-50].

2.2.4.2 Effect of Li on Mg:

Magnesium possesses less formability as it lacks the required number of independent slip systems mandatory for the Von Mises theorem for homogeneous plastic deformation. Lithium enhances the machinability of magnesium [51]. Li addition reduces the c/a ratio of the hexagonal matrix, which allows for multiple slip systems to be activated [52]. This subsequently leads to an increase in Peierls stress for basal slip compared to prismatic slip, thereby activating prismatic slip [53]. Evaluation of texture and Transmission Electron Microscopy lead to the surmise that lithium addition increases gliding of <c+a> dislocations on {11-22} pyramidal planes [54]. The {11-22} <11-23> dislocations facilitate extra slip modes and fulfill von Mises criteria, thereby resulting in increased formability related to the addition of lithium.

According to the Mg-Li phase diagram (Fig. 2.1) [55], Mg has an HCP structure (α phase) up to 5.5 wt.% Li, HCP α phase along with BCC β phase for Li between 5.5 wt.% to 10.5 wt.%, and entirely BCC β phase above 10.5 wt.% Li. There is a eutectic point at 7.9 wt.% Li at 588 °C. Li in solid solution up to 5.5 wt. % in Mg lowers c/a ratio of hexagonal system from 1.624 to 1.60, which increases the feasibility for activation of non-basal slip [51]. The single α phase of Mg-Li alloy encounters substantial hinderance during processing at room temperature by cold rolling, extrusion, ECAP, etc. The BCC β phase and the HCP α phase coexist for Li content in the range of 5.5 to10.5 wt%. The amount of β phase is proportional to the content of Lithium, which subsequently boosts formability. Beyond 10.5wt% of Li, the crystal structure transforms to BCC, rendering the alloy extremely ductile.

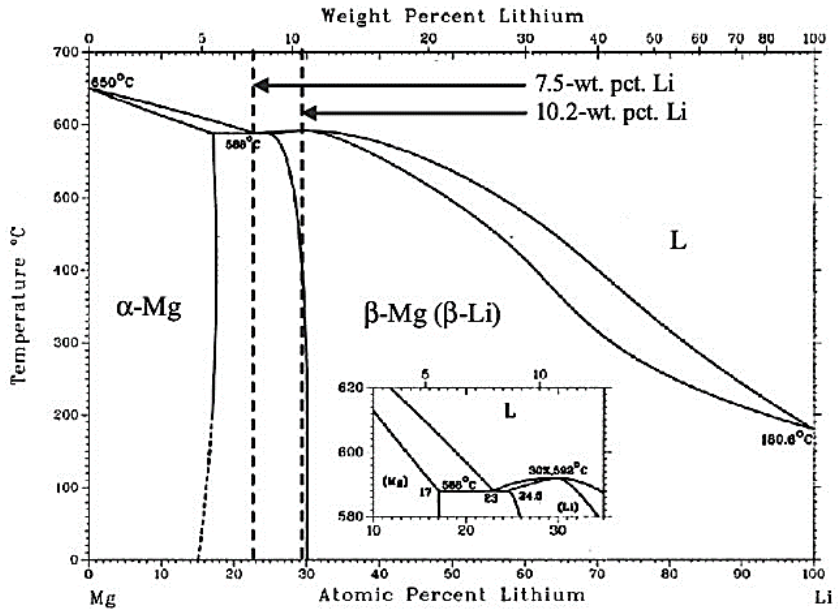

Figure 2.3 Mg-Li binary phase diagram [56]

Kim et al. [57] reported that α phase could nucleate within the β phase as a result of decrease in solubility of Mg in β phase as temperature drops below (α+β)/β boundary. They reported that two types of morphologies are formed during casting. The morphology varies according to the wt.% of Li, which involves two types of the solidification process, one in which solidification takes place through the α+β region and the other process which involves cooling through the β phase succeeded by α+β phase. The former process leads to the generation of a globular structure, whereas the latter process results in the creation of a lath type of structure. Wrought processing of globular-type microstructure at room temperature is difficult, leading to surface cracks. However, the dual-phase lath-type microstructure can be processed at room temperature to achieve better strength and ductility.

Lee and Jones [58] investigated tensile and strain hardening behavior of α, β and (α+β) based Mg-Li alloys, which exhibited typical stress-strain behaviour, as depicted in **Figure. 2.4**. From these curves, it is clear that the addition of 1.2 wt. % Li to pure Magnesium increases the proof stress and strain hardening rate, which are attributed to the solid solution strengthening mechanism.

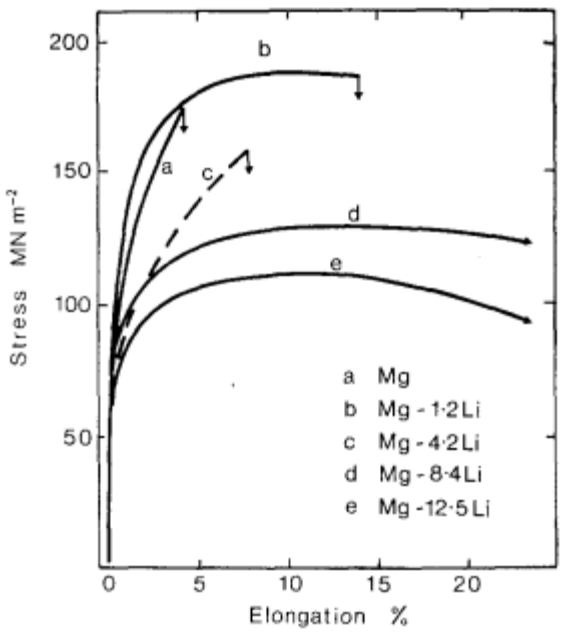

Figure 2.4 Strain hardening behavior reported beyond 1.2 wt. % of Li in Mg alloys. [58]

As Li content is increased to 4.2 wt.%, the proof stress is lowered, and the strain hardening rate is also lessened. Hauser et al. [52], also inferred that increase in Li content led to the introduction of prismatic slip along with basal slip. A discontinuous yielding behavior (Portevin-Le Chatelier effect) was found to occur in 4.2 wt.% Li alloy and is depicted by a broken line. The change in microstructure from HCP to BCC, as Li content increases from 8.4 wt.% to 12.5 wt.%, is bolstered by a boost in ductility. The α+β dual region renders the optimum blend of strength and ductility, which is essentially a function of the fraction of α and β phases in the alloy. The strength can be attributed to the presence of a hard α phase, and the ductility can be attributed to the soft β phase.

2.3 Processing Methods:

Various processing approaches used to develop magnesium alloys are broadly categorized into (i) Liquid phase processing and (ii) Solid phase processing. The preliminary motive is to ensure a relatively small grain size and homogeneously distributed secondary phase particles, which is necessary to attain required mechanical performance.

2.3.1 Liquid Phase processing:

Most liquid phase methods to prepare magnesium alloys were categorized into one of the following processes: sand casting, die casting, squeeze casting, stir casting, semi-solid metal casting, and spray forming [8, 59, 60, 61]. Magnesium is conventionally casted within mild steel crucibles prior to fabricating cast or wrought components. There are several advantages in preparing alloys through liquid phase processing, like, the ability to attain a near-net shape, facilitating superior production rates. Machining can be minimized. Extremely intricate patterns could be manufactured using die casting along with ensuring finish, precision and strength.

Magnesium being highly reactive, is extremely susceptible to all forms of corrosion, including oxidation. As far as oxidation is concerned, magnesium forms an oxide which adheres to the surface like that in the case of Aluminium, but unlike in the case of alumina, Magnesium oxide accelerates the oxidation. The kinetics of oxidation are expedited exponentially with increase in temperature, especially during melting and casting of magnesium. The melting initiates around 650^{o}C, and the increase in the oxidation kinetics is so pronounced that by 850 °C, the exposed surface of the molten metal gets rapidly oxidized causing it to immediately catch fire. This phenomenon necessitates the cautious implementation of inert atmospheres or fluxes to ensure minimal oxidation and to prevent wastage of molten metal. Recent preparations have seen a rise in the usage of vacuum induction melting to ensure a casting ingot free from impurities and oxidation. This method was formulated to regulate grain size by heating the molten bulk of the metal to a temperature of around 850 ℃ for about 0.5 hours, following which the metal was rapidly cooled by pouring it into the mold. While involving highly reactive metals like Li, induction melting under an inert atmosphere proves to be a suitable choice [62, 63]. Vacuum arc melting is also used to prepare the master alloys necessary for the Mg alloy preparation.

2.3.2 Solid Phase processing:

The major challenge in developing metal matrix nanocomposites is ensuring uniform distribution of the secondary phase particles within the matrix via an economically viable processing route. The processing routes for the development of magnesium-based nano-composites are categorised as ex-situ routes, wherein the reinforcements are first produced and then added to the matrix, and in-situ routes, in which the reinforcement is developed in-situ processing, preliminarily via controlled reactions [64]. Ex situ routes can be categorized into

solid-state and liquid-state routes. Liquid state processes are relatively simple and present the possibility of obtaining near-net shape objects on a mass-produced scale. However, such routes present challenges regarding nanoparticle dispersion due to the probability of agglomeration and suppressed wettability in the molten matrix, which adversely affect mechanical properties [65].

Solid-state approaches for mass production of nano-composites include powder metallurgy routes. Matrix/reinforcement wetting issues prevalent in liquid and semi-solid routes are significantly diminished [66]. Powder metallurgy processes are also capable of producing near-net shape objects. This approach can incorporate a higher concentration of reinforcements while presenting the flexibility to generate matrix/reinforcement systems and/or phases not achievable by conventional casting, specifically metastable phases [6]. The main demerits include inviable economics and extensive porosity associated with the end product, which mandates subsequent follow-up processes to ensure densification and negate porosity like extrusion, rolling, or forging.

Powder Metallurgy approaches normally consist of multiple stages: a blending of matrix and reinforcements; compaction of the blend by cold press; degassing of the compact to expel volatile matter such as lubricants, moisture, and gases, followed by consolidation of green compacts by different processes like direct sintering, hot isostatic pressing (HIP), hot extrusion or cold sintering [67], Severe plastic deformation approaches like equi-channel angular pressing (ECAP), high-pressure torsion. [68].

In traditional powder metallurgy, blending aims to combine powders without initiating material transfer among the components. However, during high-energy milling, reinforcement particles are introduced into the matrix by means of solid-state bonding. In mechanical alloying, for instance, matrix and alloying elements/reinforcement are fused together by a series of processes that involve cold welding, fracturing, and re-welding of the particles [69]. The metallic alloy is strengthened via grain size refinement and dispersion of nanoparticles. During mechanical alloying, some amount of powders is sealed within a container along with the grinding media, preferably under argon or some other inert gas, and then agitated at high speeds for a pre-specified duration. Dense materials like stainless steel or tungsten carbide are generally preferred as the milling media and velocity of the balls determine the kinetic energy they imparted to the powders. The main parameters affecting the morphology and composition of the composite powder include ball-to-powder ratio, milling time, speed of rotation, the material of

the vial and balls, milling medium etc. A process control agent is added during milling to minimize cold welding and consequent agglomeration. Methanol, stearic acid, and paraffin may be used as PCAs [70]. During this persistent deformation, refinement of the intrinsic structure of the powders may occur at the nanoscale, resulting in the generation of nanostructured powders

The phenomena of grain refinement resulting from mechanical alloying has been explained and explored in detail by Fecht et al. [71]. It starts with localized deformation in shear bands possessing high number density of dislocations; this is succeeded by annihilation and recombination of dislocations, thereby generating nanometre-scale sub-grains at the end of the process. Thirdly, the sub-grain boundary is converted into high-angle grain boundaries having arbitrary and discrete orientations. During the process, the risk of contamination of powders due to wear of ball and vial material and disintegration of the process control agents needs to be carefully monitored and mitigated [72]. The milled powders obtained after milling can also be introduced as reinforcements for casting processes.

2.3.3 Hot Extrusion:

Hot extrusion is one of the thermo-mechanical processes to improve the mechanical properties of the Mg alloys through densification of the material and a few phenomena that influence the microstructure. The deformation that happens during extrusion was observed to impact a myriad of features in the microstructure like grains, secondary phases, precipitates etc. Deformation of metals by varied approaches results in the generation of thermodynamically unstable microstructure comprised of deviations from ideal arrangement of crystals, such as defects, dislocations, sub-grains etc. The internal energy inherent within the microstructure can be decreased by three main phenomena: recovery, recrystallization and grain growth. Lowering of energy via recovery happens by means of removing point defects along with annihilating and rearranging dislocations via glide, climb and cross-slip. When the phenomenon of recovery occurs simultaneously along with deformation, it is termed as dynamic recovery. The annealing stage prior to recrystallization devoid of grain-boundary-migration can be designated as recovery. The second stage, namely recrystallization both static and dynamic, refers to generation and mobility of high-angle grain boundaries caused by the accumulated energy of deformation or temperature [73]. The third, grain growth is defined as the migration of grain boundaries resulting in the reduction of grain boundary area [74,75]. The development of

magnesium and its alloys is viable and is conducted at elevated temperature wherein dynamic recrystallization (DRX) is thermodynamically favored.

Extrudability refers to the ease with which an alloy can be extruded. It is affected by mainly two parametres:1) the pressure needed to begin extrusion and 2) the resistance against surface-defects, both of which can impede the extrusion-speed and subsequently productivity. A material with favorable extrudability should be capable of being extruded under low extrusion load with high extrusion speed, and still be able to retain excellent surface finish and precise geometrical tolerance devoid of defects [1]. The extrudability of Mg based alloys are substantially lesser than that of Al based alloys [76].

The limited extrudability of certain Mg based alloys like AZ61, ZK60, and high RE-containing alloys, is sometimes also due to their high strength. In such a case, the press cannot extrude the alloys through a die at low temperatures; hence, they ought to be processed at relatively greater temperatures with low speed. If the speed of extrusion exceeds a discrete magnitude, cracks might develop across the outer surface of the extruded sample. This phenomenon is termed as hot shortness [77]. Hot shortness is also deemed to occur if peak temperature within the die becomes greater than the solidus temperature of the alloy or melting point of any inherent secondary phase/particles [78]. Tensile stresses on the surface of the extrudite give rise to transverse cracks on the periphery. The alloy is under a state of triaxial stress within the die, which subsequently transforms into solely tensile stress along the walls, as the sample is extruded out [1]. As tensile strength of Mg alloy drops substantially with an increase in temperature [79], transverse cracks will be generated if the tensile stress along the periphery is greater than the strength of the alloy at that specific temperature.

Multiple methodologies have been implemented to improve the extrudability of Mg based alloys. Lower alloying additions generally result in superior extrudability, since Mg alloy with lesser alloying additions tends to be softer upon extrusion, resulting in subdued extrusion temperature and greater speeds. As far as thermomechanical processing is concerned, homogenization of Mg-alloy pellets prior to extrusion can boost extrudability. For instance, homogenized AZ31 billets can be extruded over a relatively wider range of extrusion conditions when compared to cast AZ31 billets [76]. Moreover, the development of transverse cracks owing to tensile stress on the periphery, can be suppressed by application of optimal lubricants on the die-walls. This in turn lowers friction between the die-wall and the periphery of the billet, and

negates the issue of resultant increase in temperature [1]. The most commonly used lubricants include but are not limited to compounds with minimal thermal conductivity such as Molybdenum di-sulphide, grease, oil, and graphite [1].

2.3.3.1 Extrusion in Powder Metallurgy:

Extrusion of metal powders to near final shape, usually for specimens with a weight less than 2 kg, plays a significant role compared to other processes in powder metallurgy. The extrusion of finished or semi-finished products obtained by the powder route is necessary when melting and casting cannot be implemented to process the material. Moreover, extrusion helps in achieving extremely fine grains and finely distributed precipitates [80]. Extrusion is also instrumental in attaining a uniform distribution of minute inclusions to achieve dispersion hardening.

The powder particulates are individually deformed parallel to extrusion direction during extrusion at temperatures near the recrystallization point, and due to the high thermal energy associated with the process, the surface area is increased. Oxides and other surface films on the surface break up, and new reactive metallic surfaces are exposed and susceptible to chemical interactions/metallurgical bonding. The powder is compressed and compacted during extrusion, and the newly formed surfaces are bonded together by pressure welding. Even in the case of powders with a low density, such as that of magnesium-based alloys, total compaction, and completely porosity-free material are obtained by extrusion if particles can be sheared sufficiently. It has been stated beyond doubt that the workability of magnesium alloys is limited or even not possible at temperatures below 200–225 ℃ [81].

There are various strategies for extruding metallic powders depending on the powder composition, morphology, inherent porosity, densification characteristics, and intended properties. The powder can be directly added and extruded; in some cases, the powder is cold compacted and then subjected to extrusion. In yet another approach, the powder is sealed within a capsule and extruded after the completion of degassing of the said capsule. The various approaches are elaborated upon in the following paragraphs [82]:

Addition of loose powder: The die in which the powder was taken, was shaken gently to ensure close packaging before the extrusion was carried out. The powder being loosely filled has a density of not more than 50% of the theoretical density due to the huge number of interstices

within the powder. Hence, a relatively long container is preferable. The extruding ram first compresses and compacts the powder before the start of the actual extrusion process. It can be used only rarely, and that too for very few powders [1].

Pre-compaction of the Powder outside the Press: Green compacts are subjected to cold isostatic pressing, particularly in the case of angular particles or flakes. These compacts are physically so rugged and stable that they do not break up upon handling before extrusion. The powder filled into a preformed die is subjected to a uniformly applied load, which raises the powder density from 35-50% of the apparent density to 70-85%. The risk of failure by fracture of the pre-compacted billet can be further minimized by sintering followed by extrusion.

Encapsulation of the Powder before Extrusion: Usually, the metallic powder is filled and compacted in a metal capsule, after which it is evacuated, often at higher temperatures, and then vacuum sealed before the commencement of extrusion. This approach is implemented upon powders that are highly susceptible to react with air and extrusion lubricants and also to ensure the protection of operators from toxic materials while handling, such as Be and U. It eliminates the risk of fracture of green compacts with round powders which present difficulty in being compacted in the form of a billet. It also helps to ensure improved lubrication and friction behavior with respect to the die. It assists in minimizing excess flow stress during extrusion, keeping the base material away from the die and the zone of severe shear deformation. This is preferably used for materials that exhibit low ductility [83]. High-purity materials need to be handled and processed in a clean room with meticulous cleaning of the can and evacuation at a high temperature. The main demerit of this process is that the can material adheres to the surface of the extruded product and is normally difficult to remove. [84].

A billet derived from extruding a metallic powder generally is lower in density than a cast billet. A longer billet is hence required for the same weight. During extrusion, the ram initially compresses the yet partially compacted powder before the particles experience shear deformation and friction with each other in the entry zone to the die and within the die itself. The intergranular bonding on the newly formed surface occurs as a result of a combination of friction and pressure welding. It occurs at a much faster rate than conventional sintering processes. The extrusion process gives rise to a better bond between individual particles as compared to sintering. [85].

The variation in the load profile during the extrusion of powders is drastically distinct from that of cast billets because there is a far, gradual increase in compaction load during the initial part of the ram movement. A limited inhomogeneity of the flow in the deformation zone should be sufficient for the structures to conform to each other but not so high so as to subject the composite material to unacceptable internal stresses. The composite components should be capable of flowing as a bulk under process-specific stress conditions. Extrusion as a process incorporates the three basic prerequisites so as to ensure drastic improvement in material properties: a) compressive deformation b) large strains in one operation c) flexibility to influence deformation zone by die design. In direct hot extrusion with lubrication, the deformation developing in the material flow through conical dies is virtually covered by the die cone. In case of large die opening angles, it curves into the billet. The lubrication minimizes the friction to such an extent so as to allow for the assumption that the friction has negligible influence on the material flow [86]. Katrak et al. has meticulously reported that magnesium alloys, as a whole, are slower to extrude than aluminum alloys by a fraction of 1/3 to 2/3 [83].

Mullera et al., [86] carried out the indirect extrusion of multiple Mg-alloys after preheating them up to 250ºC and 350ºC at an extrusion ratio of 30. The ram speed was varied from 0.5 mm s^{-1} and 3 mm s^{-1}. The extruded samples were cooled in the air. It was surmised that elongation to fracture decreases with increasing temperature. The tensile yield stress increases as speed decreases and extrusion temperature increases. The trials at different temperatures and with different speeds show that the extrusion forces decrease as billet temperature increases. The peak force is the limiting parameter if more complicated profiles with high extrusion ratios are to be extruded. An increase in temperature and a decrease in extrusion speed leads to lower extrusion forces; it specifically lowers the maximum force at the start of extrusion.

The powder metallurgical approach has been implemented by previous works [88] not only to boost the mechanical properties but also to enhance the dismal corrosion resistance of magnesium owing to its highly ionic character. Pure magnesium produced via powder metallurgy was compacted at pressures ranging from 100 MPa to 500 MPa at various temperatures. Duarte et al., [89] have synthesized Mg-CeO_2 composites via powder metallurgy, having reinforcements with volume fractions of 1%, 2%, and 4%. The temperature used was 620ºC for a time of 6h. These materials were characterized using light microscopy, SEM and EDS, and the Vickers micro-hardness test. The samples containing 4% of reinforcements

attained the highest values of densification and hardness, at the same time exhibiting a homogeneous dispersion of reinforcements and few defects. It has also been concluded that recrystallization and grain growth impede the attainment of high-strength composites; hence, shorter sintering times are implemented.

2.4 Scope of Work

From the literature survey, it was perceived that Mg-Ni-Gd system was not thoroughly investigated in terms of alloys produced with LPSO phases. The Li inclusion into the system would make it a potential alloy for various applications like automobile parts and drones due to its impressive specific strength. So, it was decided to study the effect of Li on the LPSO phase formation by varying the Li content, possibly at different extrusion temperatures. To further establish the optimum amount of Li to be used to maintain a balance between strength and ductility. The dual phase Mg-Li alloys so far have not included a synergetic effect of various strengthening mechanisms like grain size refinement, dispersion strengthening through second phase particles and LPSO phases and solid solution strengthening. An attempt is made to address this absence and to explore the possibilities in designing alloys with a good specific strength has been made in this work.

It was also understood that the powder metallurgy route for the development of high strength magnesium alloys has not yet been fully explored. Among the different approaches available in powder metallurgy, a significant amount of work has been done on the rapid solidification of powders, but not much work has been yet done on mechanical alloying. So it was decided to implement mechanical alloying of magnesium powders with rare earth based master alloys owing to the capability of mechanical attrition in producing metastable phases and intermetallic phases. This work aims to focus on exploring the probability of formation of long periodic stacking order phases in Zn-devoid alloy systems. The powders derived after milling would be hot extruded after subjecting them to various heat treatment procedures.

The microstructural changes and phase evolution after each subsequent phase would be characterised by X-Ray Diffraction, SEM and TEM micrography. The extruded samples would be subjected to mechanical testing like hardness, compressive and tensile to verify and evaluate their mechanical behaviour.

References:

[1] Bauser, M., and Klaus Siegert. *Extrusion*. ASM International, 2006.page 289.

[2] Hull, A. W. "The crystal structure of magnesium." *Proceedings of the National Academy of Sciences* 3.7 (1917): 470-473

[3] Sun, Dingyi et al. "Proliferation of twinning in hexagonal close-packed metals: Application to magnesium." *Journal of The Mechanics and Physics of Solids* 112 (2017): 368-384.

[4] Clyne, T. W., and P. J. Withers. *An introduction to metal matrix composites*. Cambridge university press, 1995.

[5] Ye, Hai Zhi, and Xing Yang Liu. "Review of recent studies in magnesium matrix composites." *Journal of materials science* 39.20 (2004): 6153-6171.

[6] Suryanarayana, C., and Nasser Al-Aqeeli. "Mechanically alloyed nanocomposites." *Progress in Materials Science* 58.4 (2013): 383-502.

[7] Zhang, Z., and D. L. Chen. "Consideration of Orowan strengthening effect in particulate-reinforced metal matrix nanocomposites: A model for predicting their yield strength." *Scripta Materialia* 54.7 (2006): 1321-1326.

[8] Lloyd, D. J. "Particle reinforced aluminium and magnesium matrix composites." *International materials reviews* 39.1 (1994): 1-23.

[9] Hazzledine, P. M. "Direct versus indirect dispersion hardening." *Scripta metallurgica et materialia* 26.1 (1992): 57-58.

[10] Zhang, Z., and D. L. Chen. "Consideration of Orowan strengthening effect in particulate-reinforced metal matrix nanocomposites: A model for predicting their yield strength." *Scripta Materialia* 54.7 (2006): 1321-1326.

[11] Vaidya, Rajendra U., and K. K. Chawla. "Thermal expansion of metal-matrix composites." *Composites Science and Technology* 50.1 (1994): 13-22.

[12] Sanaty-Zadeh, A. "Comparison between current models for the strength of particulate-reinforced metal matrix nanocomposites with emphasis on consideration of Hall–Petch effect." *Materials Science and Engineering: A* 531 (2012): 112-118.

[13] Kassner, M. E. "Taylor hardening in five-power-law creep of metals and Class M alloys." *Acta materialia* 52.1 (2004): 1-9.

[14] Habibnejad-Korayem, M., R. Mahmudi, and W. J. Poole. "Enhanced properties of Mg-based nano-composites reinforced with Al2O3 nano-particles." *Materials Science and Engineering: A* 519.1-2 (2009): 198-203

[15] Gupta, M., and N. M. L. Sharon. "Magnesium, magnesium alloys, and magnesium composites. 2011." *New York: Jonh Wiley & Sons*.

[16] Reed-Hill, R. E. "Role of deformation twinning in determining the mechanical properties of metals." *The Inhomogeneity of Plastic Deformation, ASM Seminar. 1973, 285-311*. 1973

[17] Wang, Y. N., and J. C. Huang. "Texture analysis in hexagonal materials." *Materials Chemistry and Physics* 81.1 (2003): 11-26.

[18] Kleiner, S., and Peter J. Uggowitzer. "Mechanical anisotropy of extruded Mg–6% Al–1% Zn alloy." *Materials Science and Engineering: A* 379.1-2 (2004): 258-263.

[19] Kawamura, Yoshihito, et al. "Rapidly solidified powder metallurgy $Mg_{97}Zn_1Y_2$ alloys with excellent tensile yield strength above 600 MPa." *Materials Transactions* 42.7 (2001): 1172-1176.

[20] Akiyama, H., and Yoshihito Kawamura. "The Effect of EMS on the Microstructure of LPSO Mg-Zn-Y Cast Alloy." *Materials Science Forum*. Vol. 706. Trans Tech Publications, 2012.

[21] Luo, Z, and S Q Zhang. "Y L Tang and D S Zhao." *J. Alloys Compounds* 209 (1994): 275.

[22] Luo, Z. P., and S. Q. Zhang. "High-resolution electron microscopy on the X-$Mg_{12}ZnY$ phase in a high strength Mg-Zn-Zr-Y magnesium alloy." *Journal of Materials Science Letters* 19.9 (2000): 813-815.

[23] Xu, Yongbo, et al. "Guinier-preston zone, quasicrystal and long-period stacking ordered structure in Mg-based alloys, a review." *Acta Metallurgica Sinica (English Letters)* 26.3 (2013): 217-231.

[24] Abe, E., et al. "Polytypes of long-period stacking structures synchronized with chemical order in a dilute Mg–Zn–Y alloy." *Philosophical Magazine Letters* 91.10 (2011): 690-696

[25] Xu, Daokui, En-hou Han, and Yongbo Xu. "Effect of long-period stacking ordered phase on microstructure, mechanical property and corrosion resistance of Mg alloys: A review." *Progress in Natural Science: Materials International* 26.2 (2016): 117-128.

[26] Nishida, Minoru, Yoshihito Kawamura, and Takateru Yamamuro. "Formation process of unique microstructure in rapidly solidified $Mg_{97}Zn_1Y_2$ alloy." *Materials Science and Engineering: A* 375 (2004): 1217-1223.

[27] Saal, James E., and C. Wolverton. "Thermodynamic stability of Mg-based ternary long-period stacking ordered structures." *Acta Materialia* 68 (2014): 325-338.

[28] Itoi, T., et al. "Long period stacking structures observed in $Mg_{97}Zn_1Y_2$ alloy." *Scripta Materialia* 51.2 (2004): 107-111.

[29] Egusa, D., and E. Abe. "The structure of long period stacking/order Mg–Zn–RE phases with extended non-stoichiometry ranges." *Acta Materialia* 60.1 (2012): 166-178.

[30] Luo, Z. P., D. Y. Song, and S. Q. Zhang. "Strengthening effects of rare earths on wrought Mg-Zn-Zr-RE alloys." *Journal of alloys and compounds* 230.2 (1995): 109-114.

[31] Luo, Z. P., and S. Q. Zhang. "High-resolution electron microscopy on the X-$Mg_{12}ZnY$ phase in a high strength Mg-Zn-Zr-Y magnesium alloy." *Journal of Materials Science Letters* 19.9 (2000): 813-815.

[32] Matsuda, M., et al. "Variation of long-period stacking order structures in rapidly solidified Mg97Zn1Y2 alloy." *Materials Science and Engineering: A* 393.1-2 (2005): 269-274.

[33] Inoue, Akihisa, et al. "Novel hexagonal structure of ultra-high strength magnesium-based alloys." *Materials Transactions*43.3 (2002): 580-584.

[34] Gao, Yan, et al. "Comparison of microstructure in Mg–10Y–5Gd–0.5 Zr and Mg–10Y–5Gd–2Zn–0.5 Zr alloys by conventional casting." *Journal of Alloys and Compounds*477.1-2 (2009): 374-378.

[35] Yamada, Kentaro, et al. "Alloy development of high toughness Mg-Gd-Y-Zn-Zr alloys." *Materials transactions* 47.4 (2006): 1066-1070.

[36] Apps, P. J., et al. "Precipitation reactions in magnesium-rare earth alloys containing yttrium, gadolinium or dysprosium." *Scripta Materialia* 48.8 (2003): 1023-1028.

[37] Nie, J. F., and B. C. Muddle. "Characterisation of strengthening precipitate phases in a Mg–Y–Nd alloy." *Acta Materialia* 48.8 (2000): 1691-1703.

[38] Chino, Yasumasa, et al. "Novel equilibrium two-phase Mg alloy with the long-period ordered structure." *Scripta materialia* 51.7 (2004): 711-714.

[39] Zhu, Y. M., A. J. Morton, and J. F. Nie. "The 18R and 14H long-period stacking ordered structures in Mg–Y–Zn alloys." *Acta Materialia* 58.8 (2010): 2936-2947.

[40] Itoi, T., et al. "A high-strength Mg–Ni–Y alloy sheet with a long-period ordered phase prepared by hot-rolling." *Scripta materialia* 59.10 (2008): 1155-1158.

[41] Hagihara, K., et al. "High-temperature compressive deformation behavior of Mg97Zn1Y2 extruded alloy containing a long-period stacking ordered (LPSO) phase." *Materials Science and Engineering: A* 560 (2013): 71-79.

[42] Hagihara, K., et al. "Plastic deformation behavior of Mg97Zn1Y2 extruded alloys." *Transactions of Nonferrous Metals Society of China* 20.7 (2010): 1259-1268.

[43] Chino, Yasumasa, et al. "Novel equilibrium two-phase Mg alloy with the long-period ordered structure." *Scripta materialia* 51.7 (2004): 711-714.

[44] Hagihara, K., N. Yokotani, and Y. Umakoshi. "Plastic deformation behavior of $Mg_{12}YZn$ with 18R long-period stacking ordered structure." *Intermetallics* 18.2 (2010): 267-276.

[45] Itoi, T., et al. "A high-strength Mg–Ni–Y alloy sheet with a long-period ordered phase prepared by hot-rolling." *Scripta materialia* 59.10 (2008): 1155-1158.

[46] Shao, X. H., et al. "Microstructure and microhardness evolution of a $Mg_{83}Ni_6Zn_5Y_6$ alloy upon annealing." *Journal of Alloys and Compounds* 509.26 (2011): 7221-7228.

[47] Kawamura, Yoshihito, et al. "Elevated temperature Mg97Y2Cu1 alloy with long period ordered structure." *Scripta Materialia* 55.5 (2006): 453-456.

[48] Wang, Dandan, et al. "Abundant long period stacking ordered structure induced by Ni addition into Mg–Gd–Zn alloy." *Materials Science and Engineering: A* 618 (2014): 355-358.

[49] Garcés, Gerardo, et al. "Influence of rare-earth addition on the long-period stacking ordered phase in cast Mg–Y–Zn alloys." *Journal of Materials Science* 49 (2014): 2714-2722.

[50] Okuda, Hiroshi, et al. "Evolution of long-period stacking ordered structures on annealing as-cast Mg85Y9Zn6 alloy ingot observed by synchrotron radiation small-angle scattering." *Scripta Materialia* 68.8 (2013): 575-578.

[51] Raynor, Geoffrey V. "The physical metallurgy of magnesium and its alloys." *Pergamon Press* (1959).

[52] Hauser, F. E., et al. "Deformation mechanisms in polycrystalline aggregates of magnesium." *Transactions of the ASM* 47 (1955): 102-134.

[53] Quimby, R. M., J. D. Mote, and J. E. Dorn. "Yield point phenomena in magnesium-lithium single crystals." *Am. Soc. Metals, Trans. Quart.* 55 (1962).

[54] Agnew, S. R., M. H. Yoo, and C. N. Tome. "Application of texture simulation to understanding mechanical behavior of Mg and solid solution alloys containing Li or Y." *Acta materialia* 49.20 (2001): 4277-4289.

[55] A. Nayeb Hashemi, J. B. Clark, A. D. Pelton, *Bulletin of Alloy Phase Diagrams*, 5 (1984) 365–374.

[56] Atkins, Garrett, et al. "Magnesium-lithium alloy weldability: A microstructural characterization." *JOM* 6 (2004).]

[57] Kim, Y. W., et al. "Widmanstätten type solidification in squeeze casting of Mg-Li-Al alloys." *Scripta materialia* 38.6 (1998): 923-929.

[58] Lee, R. E., and W. J. D. Jones. "Microplasticity and fatigue of some magnesium-lithium alloys: Part 1 Tensile microplasticity." *Journal of Materials Science* 9 (1974): 469-475.

[59] M. M. Avedesian and H. Baker (ed.) *ASM Specialty Handbook—Magnesium and Magnesium Alloys*. Materials Park, OH: ASM International (1999).

[60] N. Chawla and K. K. Chawla, *Metal Matrix Composites*. New York: Springer (2006).

[61] H. E. Friedrich and B. L. Mordike (ed.) *Magnesium Technology—Metallurgy, Design Data, Applications*. Berlin: Springer (2006).

[62] Ji, Hao, et al. "Influence of Er addition on microstructure and mechanical properties of as-cast Mg-10Li-5Zn alloy." *Materials Science and Engineering: A* 739 (2019): 395-403.

[63] Zhou, Yucheng, et al. "Dynamic nano precipitation behavior of as-cast Mg-4Li-4Zn-Y alloy during high-temperature deformation." *Materials Science and Engineering: A* 707 (2017): 110-117.

[64] Mine, Yoji, et al. "Microfracture behaviour of extruded Mg–Zn–Y alloys containing long-period stacking ordered structure at room and elevated temperatures." *Materials Science and Engineering: A* 570 (2013): 63-69.

[65] Ye, Hai Zhi, and Xing Yang Liu. "Review of recent studies in magnesium matrix composites." *Journal of materials science* 39.20 (2004): 6153-6171.

[66] Hashim, J., L. Looney, and M. S. J. Hashmi. "Metal matrix composites: production by the stir casting method." *Journal of materials processing technology* 92 (1999): 1-7.

[67] Cintas, J., et al. "High-strength PM aluminium by milling in ammonia gas and sintering." *Scripta Materialia* 53.10 (2005): 1165-1170.

[68] Liu, Y. B., et al. "Recent development in the fabrication of metal matrix-particulate composites using powder metallurgy techniques." *Journal of Materials Science* 29.8 (1994): 1999-2007.

[69] Bera, Supriya, et al. "Mechanical properties of Al7075 alloy with nano-ceramic oxide dispersion synthesized by mechanical milling and consolidated by equal channel angular pressing." *Journal of Alloys and Compounds* 548 (2013): 257-265.

[70] Witkin, D. B., and Enrique J. Lavernia. "Synthesis and mechanical behavior of nanostructured materials via cryomilling." *Progress in Materials Science* 51.1 (2006): 1-60.

[71] Zhou, F., et al. "High grain size stability of nanocrystalline Al prepared by mechanical attrition." *Journal of Materials Research* 16.12 (2001): 3451-3458.

[72] Tuschy, E. "Bibliography: Extruding--New Processes. Pt. 1." *Metall* 36.3 (1982): 269-279.

[73] Rollett, Anthony, Gregory S. Rohrer, and John Humphreys. *Recrystallization and related annealing phenomena*. Newnes, 2017.

[74] Baker, I. "Recovery, recrystallization and grain growth in ordered alloys." *Intermetallics* 8.9-11 (2000): 1183-1196.

[75] Doherty, R. D., et al. "Current issues in recrystallization: a review." *Materials Science and Engineering: A* 238.2 (1997): 219-274

[76] Atwell LD, Barnett RM. Extrusion limits of magnesium alloys. Metall Mater Trans A. 2007;38 (12):3032–3041.

[77] Sillekens, Wim, Marco van Hout, and Franka Pravdic. *Extrusion technology for magnesium: avenues for improving performance*. na, 2005.

[78] Luo AA, Zhang C, Sachdev AK. Effect of eutectic temperature on the extrudability of magnesium– aluminum alloys. Scr Mater. 2012;66(7):491–494.

[79] Galiyev A, Kaibyshev R, Gottstein G. Correlation of plastic deformation and dynamic recrystallization in magnesium alloy ZK60. Acta Mater. 2001;49 (7):1199–1207.

[80] Emley, Edward F. "Principles of magnesium technology." (1966)

[81] Ferguson, B. L., and P. R. Roberts. "Extrusion of metal powders." *ASM Handbook* 7 (1998): 621-631

[82] G. Scharf and I. Mathy, "Development of Aluminum Wrought Materials from Rapidly Solidified Alloy Powders", *Metall., Vol 41*, (1987), p 608–616

[83] Katrak, Firoze E., et al. "Alternative Ways to Fabricate Magnesium Products." Magnesium Technology 2000 (2000): 350-354

[84] Agnew, S. R., et al. "Texture evolution of five wrought magnesium alloys during route A equal channel angular extrusion: Experiments and simulations." Acta Materialia 53.11 (2005): 3135-3146.

[85] Hammond, Vincent H. *Magnesium Nanocomposites: Current Status and Prospects for Army Applications*. No. ARL-TR-5728. Army Research Lab Aberdeen Proving Ground MD, 2011.

[86] Hariprasad, S., S. M. L. Sastry, and K. L. Jerina. "Deformation behavior of a rapidly solidified fine grained Al-8.5% Fe-1.2% V-1.7% Si alloy." Acta materialia 44.1 (1996): 383-389.

[87] Mueller, S., et al. "Microstructure and mechanical properties of the extruded Mg-alloys AZ31, AZ61, AZ80." Zeitschrift für Metallkunde 97.10 (2006): 1384-1391.

[88] Březina, Matěj, et al. "Characterization of Powder Metallurgy Processed Pure Magnesium Materials for Biomedical Applications." Metals 7.11 (2017): 461.

[89] Duarte, H. P., et al. "Investigation of the Mechanical Properties of Magnesium Metal Matrix Composites with A Fine Dispersion of CeO2 Particles."

3

Experimental Details

This chapter consists of the preparation of the alloy systems and thorough characterization for evaluating the structure-property correlations and mechanisms involved in their behaviour. The material processing was carried out using both casting and powder metallurgy route. The common steps involved in these two different routes were, making initial intermetallic alloys using arc melting, and the final step of hot extrusion processes. **Figure 3.1** outlines the strategy implemented in carrying out this work.

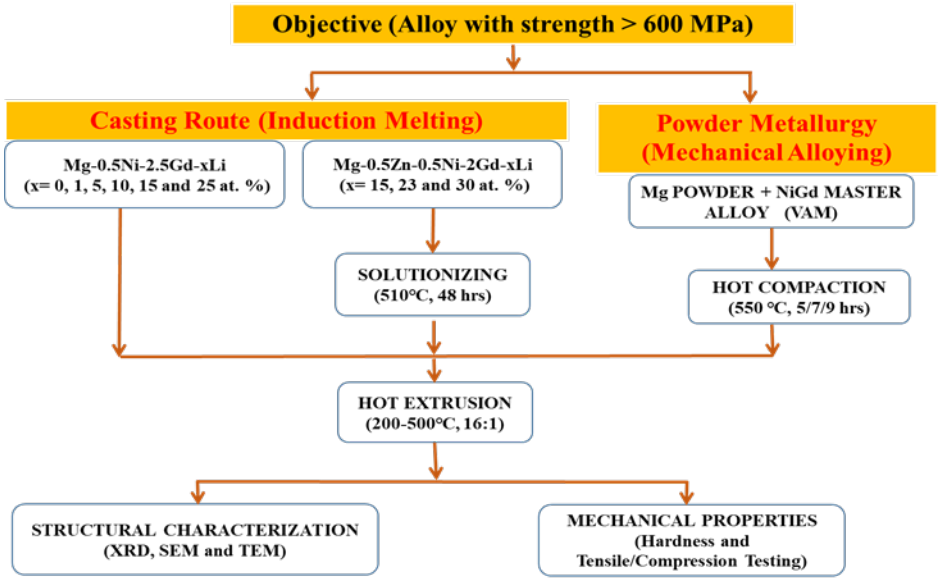

Figure 3.1 Flow chart representing the complete work of the thesis.

3.1 Preparation of Master Alloys through Vacuum Arc Re-melting:

The master alloys were produced prior to starting of the induction melting and ball milling processes for the casting and powder metallurgy routes, respectively. The decided systems require the pre-melted master alloys of NiGd for casting and powder metallurgy routes for better solubility of the individual elements. The other reason for this prerequisite was because of the greater possibility of LPSO phase formation. Ni and Gd were taken in equiatomic proportions and the master alloy was melted in a vacuum arc melting furnace (**Figure 3.2**).

The equipment used here was acquired from VAC solutions, Bengaluru. The melting chamber was cleaned thoroughly and applied a high vacuum of 10^{-4} bar to eliminate the formation of any foreign particles and impurities due to the reaction between air molecules and elements in the master alloys. Subsequently, argon gas was purged to maintain 1 atm pressure before carrying out melting. The equiatomic mixtures were subjected to four rounds of re-melting to attain homogeneity. The master alloys were found to be hard but brittle due to the formation of intermetallic phases.

Figure 3.2 Vacuum arc re-melting furnace.

3.2 Casting Route:

3.2.1 Preparation of Ingots using Vacuum Induction Melting Furnace:

The alloys with the nominal composition depending on the system were cast in a Vacuum Induction melting furnace (VIM, Vacuum techniques) (**Figure 3.3**) under an argon atmosphere. Pure Mg (99.9 %), pure Li (99 %) and an intermetallic master alloy of Ni & Gd were taken in a mild steel crucible. Due to the presence of highly reactive metals like Lithium and magnesium, their handling was done in a glove box and quick transfer into the furnace was carried out to avoid oxidation. A high vacuum of 10^{-5} bar was achieved in the furnace chamber using the roughing, rotary and diffusion pumps. The melting was carried out till the stirring by inductive forces was observed. The melt was held at the temperature around 800 ℃ for 20 minutes to ensure uniformity of the alloy mixture and then poured into a mild steel mold to obtain 20 mm diameter cylindrical rods.

Figure 3.3 Vacuum Induction Melting furnace.

3.2.2 Solutionisation of the as-Cast alloys:

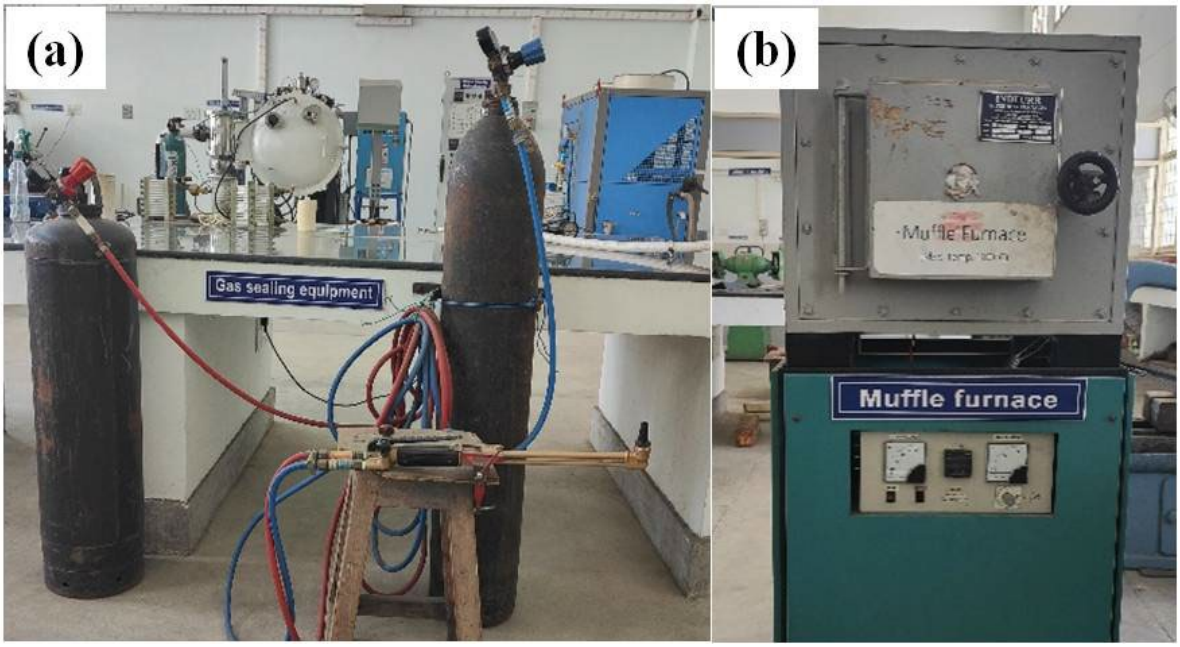

Figure 3.4 (a) Acetylene torch, (b) Muffle furnace.

In the casting route, the solutionisation was performed at 510 ℃ for the as-cast samples for a period of 48 hours. This process was carried out only in the system containing zinc as an alloying element, i.e., Mg-2Gd-0.5Ni-0.5Zn-xLi (x = 15, 25, 30) at. % but not on Mg-0.5Ni-2.5Gd-xLi (x = 0, 1, 5, 10, 15, 25) at. %. Since, Zn and Gd can be dissolved by the solutionising treatment and by intentional precipitation process or during the extrusion process at moderately high temperatures, uniform precipitation of the LPSO is expected in the matrix. The samples were sealed in a borosilicate glass tube under an argon atmosphere (using an oxy-acetylene torch (**Figure 3.3(a)**). The sealed glass tube with the sample was subsequently placed in the muffle furnace for solutionising at the aforementioned temperature and time period. Once the solutionising was done, the alloy was quenched in the water by breaking the glass tube.

3.2.3 Hot Extrusion:

Hot extrusion was performed on the as-cast samples of 20 mm diameter in the case of Mg-0.5Ni-2Gd-xLi (x = 0, 1, 5, 10, 15, 25) at. % system and on the as-solutionised samples of the same diameter for the Mg-2Gd-0.5Ni-0.5Zn-xLi (x = 15, 25, 30) at. % alloy system. The process was carried out at a temperature of 400 ℃ at a 16:1 ratio for the Zn-free system while the Zn-based system alloys were extruded at two different temperatures of 200 ℃ and 300 ℃. However, a holding time of 4 hours was the same and consistently maintained for all the alloys.

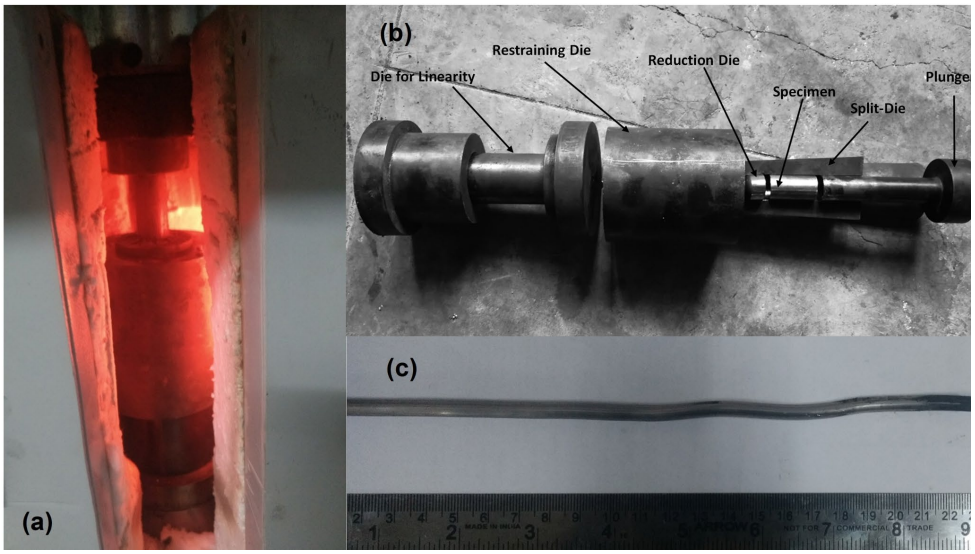

Figure 3.5 (a) Extrusion die inside the furnace, (b) Various parts of the Extrusion die set-up and (c) extruded bar.

Dies specifically for the hot extrusion requirement were designed and manufactured for extruding a billet of diameter 20 mm into a rod of 5 mm. As shown in **Figure 3.5**, two split dies enclose the specimen placed over the reduction die, which in turn goes inside the restraining die. The extrudate as shown in **Figure 3.6** which exits the die is made to pass through another die with a co-axial hole of 6 mm diameter to ensure the linearity of the sample. The whole die set-up was placed in the furnace attached to the 50-tonne capacity hydraulic press (**Figure 3.7**) and applied the required load for extrusion to take place.

Figure 3.6 Images of the sample before and after extrusion.

Figure 3.7 50-tonne Hydraulic press used for the hot extrusion of the alloys.

3.3 Powder Metallurgy Route:

3.3.1 Mechanical Alloying:

A planetary ball mill (Make: Retsch, Model: PM400) was used to mill the powders in order to achieve homogeneity in composition and a nano-grain size (**Figure 3.8**). The vials and balls are made of high-chromium stainless steel. The main concern while preparing magnesium alloys is the high affinity of magnesium for oxygen. Hence the entire process was carried out in a glove box as shown in **Figure 3.9** under an inert atmosphere to avoid the possibility of oxidation of Magnesium powder. The process was conducted in steps as enlisted below.

Figure 3.8 Planetary ball mill with 4 high chromium Vials (Retsch PM400).

1. The master alloy pellets and the ball milling vials were placed inside a glove box under an argon atmosphere. The master alloy was crushed with a mortar and pestle and was adequately weighed and placed in the vials.
2. The lids of the vials were then shut, taken out, and subjected to 2 minutes of milling at 300 rpm to pulverize the intermetallic to make a powder.
3. The vials were again opened inside the glove box and magnesium powder was added to the vials as per predetermined proportions.

4. 0.5 ml of ethanol was added to each vial as the process control agent to control the phenomenon of cold welding and to prevent formation of agglomerates and adherence of the milled powders to the walls of the vials.
5. The total weight of the powder was 10 grams so as to maintain a ball-to-powder ratio of 20:1. The lids were then shut and the vials were sealed.
6. The vials were then taken out and subjected to 150 hours of milling with intervals of 30 minutes of rest after every 30 minutes of milling operation. The milling was done at 300 rpm.
7. Small amounts of powder were removed and collected at definite intervals to understand the evolution of phases, crystallite size, and strain accumulated in the powder particles.
8. After milling, the powders were removed, transferred to plastic containers, and sealed under an argon atmosphere.

Figure 3.9 Portable Glove box used for handling highly reactive Lithium and Magnesium in a protective argon atmosphere.

After the removal of powders, the vials were filled with toluene up to half of their total capacity and are milled for 20 minutes at 10-minute intervals. The toluene washes off the powder adhered to the vials and cleanses it. The vials would be totally clean after 3 to 4 rounds of milling with toluene. Hard-to-remove layers of powder that cannot be removed by toluene will have to be ground using a Dremel rotary tool.

3.3.2 Hot Compaction:

The powder samples, if directly extruded might present the issues of porosity and absence of metallurgical bonding between the particles. Another concern with the direct extrusion of powders is that there is no window for degassing to happen. The gases trapped within the powders obstruct compaction and eventually bonding, thereby resulting in poor mechanical properties. The risk of oxidation also remains high. The powders were subjected to different cycles of heating and compaction in a hot press (**Figure 3.10**) to determine the optimal heat treatment route for obtaining a high degree of densification. Initially, the amount of powder required for a billet diameter of 20 mm and height of 25 mm was calculated. The inner walls of the die were lined with graphite sheets to prevent the bonding of the powder. The powders were transferred into the die and enclosed on both ends by floating billets in the glove box under an inert atmosphere. Around 12 grams of powder was filled so as to obtain a cold compacted specimen of 20 mm diameter and 25 mm height. Once the specimen is cold compacted, the danger of oxidation is partially minimized.

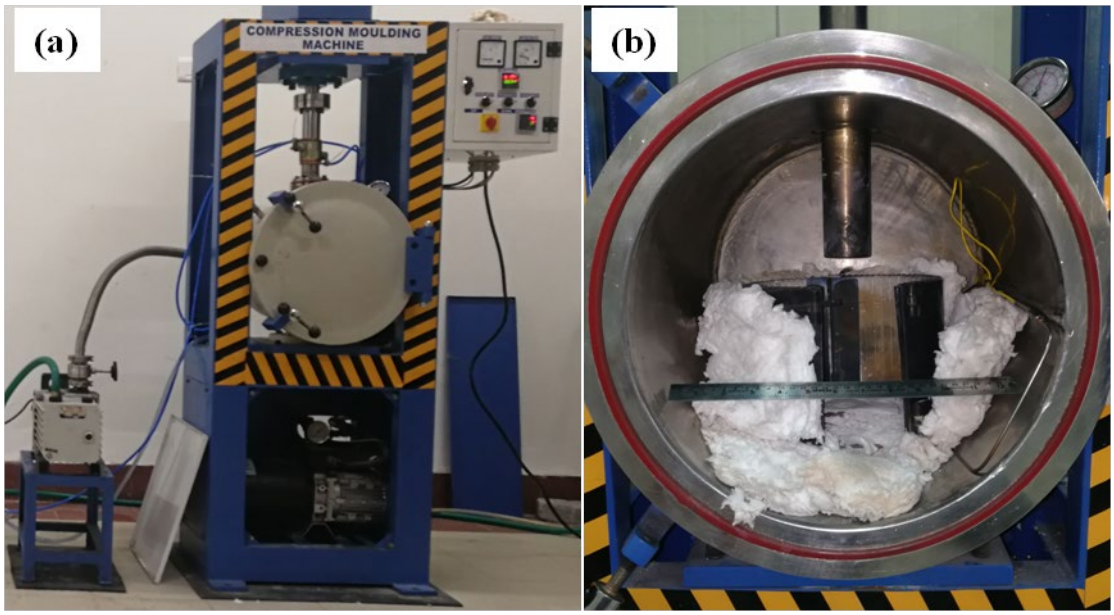

Figure 3.10 (a) Hot compaction machine and (b) Furnace chamber with the split furnace of the compaction machine.

Hot compaction temperature was common for all the samples, i.e., 550 ℃ but the compaction holding time was varied, i.e., 5 hrs, 7 hrs and 9 hrs. Finally, a load of 50 MPa was

applied at the end of the holding cycle on all the samples irrespective of the holding time. The whole hot compaction process was conducted in a continuous vacuum for an extended duration of respective time periods so as to expel all the gases entrapped within and apply a minor load at the end of the heating cycle for a short duration to initiate densification. After the removal of the load, the sample was allowed to cool down in the furnace itself under a vacuum. Once cooling is done, the chamber was purged with argon gas before removing the sample, which fills up any open pores on the surface of the billet and thus prevents oxidation.

3.3.3 Hot Extrusion for hot compacted samples:

Hot extrusion was carried out to reduce the remaining porosity in the hot compacted samples. Hot extrusion for powder route samples was performed at 500 ℃, after a holding time of 4 hours at a 16:1 ratio. The hot compacted sample of 20 mm diameter was the precursor; the extruded product would be a 5 mm diameter cylindrical rod. A reduction die having a relief angle of 45º was used for extrusion. Graphite powder mixed with oil was used as a lubricant and applied to the die before loading the sample into it. It is imperative to ensure that the temperature at the centre of the compacted sample reaches 500 ℃; hence the temperature profile was monitored using a K-type thermocouple.

Once the sample reaches 500 ℃, it was soaked for a specific duration of 4 hrs, to ensure the homogenization of temperature throughout the sample and then extruded by means of a servo-hydraulic press as depicted in **Figure 3.7**. Once the ram presses the specimen out of the reduction die, the main die is swiftly but steadily raised with a pair of tongs so as not to give any jerks to the extruded sample and the extruded specimen was cut off at the mouth of the die with a bolt cutter. The extruded portion then falls down maintaining the straightness. After every extrusion, the reduction die was checked and corrected for eccentricity, and care was taken that the plunger was not bent. It was also mandatory that the specimen possesses parallel faces so as to ensure consistent extrusion.

3.4 Characterization methods used:

The samples were subjected to physical, phase analysis, microstructural, and mechanical characterization at different stages of processing depending on the processing route. The details of the characterization techniques and equipment used are discussed below.

3.4.1 Physical characterization:

3.4.1.1 Density measurement:

As shown in **Figure 3.10**, the density measurement setup was used to measure the density of as-extruded samples. The density of the as-extruded samples was measured on Sartorius Secura YDK03, using the Archimedes principle following ASTM B 962-15 standard (ASTM International, 2017a). The sample density (ρ_s) is given as:

$$\rho_s = \frac{m_s \rho_f}{m_s - m_f} \qquad \text{(Eq. 3.1)}$$

Where, m_s – sample weight in air

m_f – sample with in fluid

ρ_f – density of the fluid

Figure 3.11. high sensitivity weighing balance with density measurement apparatus.

3.4.2 Phase analysis:

The phases present in the powders and sintered samples were analyzed using X-Ray Diffractometer, whereas the microstructure analysis was done by using Scanning Electron Microscope as discussed in the following sections.

3.4.2.1 X-ray diffraction analysis:

Phase and crystallite sizes of specimens were characterized using X-Ray Diffractometer (XRD: X'Pert PRO, PANalytical, Netherlands) shown in **Figure 3.11**. Diffraction peaks were obtained using CuK_α radiation (wavelength λ = 0.15406 nm) operated at 45 kV, 30 mA. The patterns were then analyzed using X'Pert Highscore Plus (PANalytical, Netherlands) software for phase identification and quantification which was equipped with ICDD (International Center for Diffraction Data) and ICSD (Inorganic Crystal Structure Database). The XRD measurements were conducted from 20º to 100º with a step size of 0.0167 and a time of 24.765s per step at a speed of 0.085699 per second. The analysis of as-cast samples, milled powders, and extruded samples was conducted to understand and evaluate the evolution of phases during milling and during various stages of hot working operations.

3.4.2.2 Measurement of crystallite size from XRD:

Crystallite sizes were calculated from XRD patterns using Debye Scherrer's formula. In order to eliminate the effect of instrument broadening, standard coarse-grained samples were prepared using similar composition, and XRD patterns were obtained.

Crystallite size according to Debye Scherrer's formula:

$$t = \frac{0.94.\lambda}{B_c.COS\theta} \qquad \text{(Eq. 3.2)}$$

where, t is crystallite size, λ is X-ray wavelength Cu Kα - radiation, θ is the diffraction angle and B_c is the peak broadening due to crystallite size.

Figure 3.12. PANalytical X-ray Diffraction equipment used for phase analysis.

In general broadening (Full-Width Half Maxima) is a combined effect of crystallite size, lattice strain and instrument broadening. Broadening due to instrument B_i can be calculated from the standard sample. Now by subtracting B_i from observed broadening B_o, one can obtain broadening due to crystallite size and lattice strain B_r ($B_r = B_c + B_s$),

$$B_r = \sqrt{(B_o^2 - B_i^2)} \qquad \text{(Eq. 3.3)}$$

where, B_o is the broadening of the actual sample, B_i is the broadening of the standard sample.

Broadening due to only crystallite size can be obtained from equation 3.4,

$$B_c = \frac{k\lambda}{t\,cos\theta} \qquad \text{(Eq. 3.4)}$$

Broadening due to only lattice strain can be calculated from the below formula:

$$B_s = \eta\, tan\theta \qquad \text{(Eq. 3.5)}$$

As B_r is the combined effect of crystallite size and lattice strain it can be written as follows:

$$B_r = B_c + B_s \quad \text{(Eq. 3.6)}$$

$$B_r = \frac{k\lambda}{t\,cos\theta} + \eta\, tan\theta \quad \text{(Eq. 3.7)}$$

$$B_r cos\theta = \frac{k\lambda}{t} + \eta\, sin\theta \quad \text{(Eq. 3.8)}$$

Now if a graph is plotted by considering sinθ as X-axis and B_r cosθ as Y-axis as shown in the **Figure. 3.12**, the slope of the graph will give us the lattice strain (η) value. The crystallite size can be calculated from the intercept.

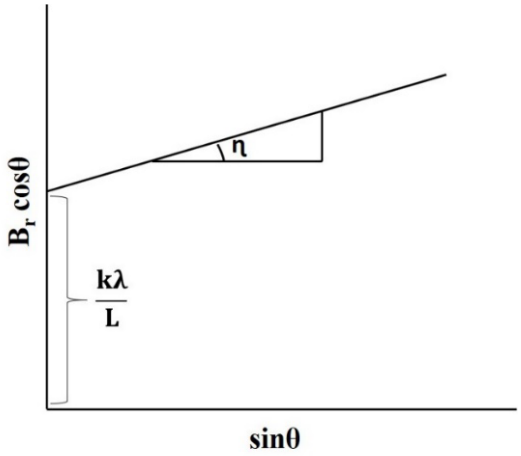

Figure 3.13. Plot of B_r cos θ against sin θ, indicating that the intercept (kλ/L) and slope (η) can be used to calculate the crystallite size (L) and lattice strain (η), respectively.

3.4.3 Microstructural analysis:

3.4.3.1 Scanning Electron Microscope (SEM):

The microstructure of the samples was examined with a Scanning Electron Microscope (**Figure 3.13**) having tungsten filament electron source (SEM: VEGA 3LMV, TESCAN, Czech Republic) using Secondary Electron (SE) and Back Scattered Electron (BSE) imaging modes. Chemical composition of the samples was qualitatively measured using Energy Dispersive X-ray Spectroscopy (EDS: Oxford Technologies, UK) attached to the SEM. The SEM was operated at an accelerated voltage of 15 kV for imaging and 20 kV for EDS analysis. The samples were metallographically polished over a series of emery papers of grades 600, 800, 1200 and 2000 in

that order, followed by disc polishing with diamond paste of grade 6 microns, 3 microns and 1 micron. Extreme care was taken to avoid every possibility of oxidation of the surface of samples. The diamond paste was dissolved in distilled alcohol, instead of water, which is normally used; alcohol was used to induce lubrication during polishing also avoids the oxidation of the surface. The etchant used to reveal the microstructure is 2% nital. The samples were vacuum sealed or put under vacuum as soon as the polishing process was complete until the SEM observation.

Figure 3.14. Scanning Electron Microscope (SEM) fitted with EDX for microstructure observation.

3.4.3.2 Transmission Electron Microscope (TEM):

The TEM instrument (TechnaiG2, FEI) equipped with a LaB_6 filament was used for studying samples at very high magnifications (**Figure 3.14**). The transmitted beam is used for imaging and also electron diffraction studies. The sample for the TEM observation was prepared first cutting thin sample slices of ~300 microns using slow speed cutting machine (Isomet, Buehler) from the as-extruded specimens and metallographically polished to a thickness of less than 100 microns. These samples were subsequently ion milled to attain a thickness of 100 nm or less at the centre, so that electron transparency can be achieved. An incident electron beam

accelerated at 200 kV was used. Bright field (BF), dark field imaging and Selected Area Electron Diffraction was used to analyze the microstructural features present in the samples.

Figure 3.15. Transmission Electron Microscope (TEM) for the microstructure analysis at the sub-micron and nano-scales.

3.4.4 Mechanical property evaluation:

Mechanical properties of processed samples were studied by using equipment such as Micro Vickers Hardness tester, uniaxial compression and uniaxial tensile tests at room temperatures were analysed by the Universal Testing Machine and the details are described in the following sections.

3.4.4.1 Hardness:

The Vickers micro-hardness of the alloys extruded after processing, in both casting and powder metallurgy route was tested on a micro Vickers hardness testing machine (Shimadzu HMT-G20ST, Japan) following ASTM C 1327-15 (ASTM International, 2019). The samples were ensured to be perfectly flat on both sides and polished, before testing. A load of 1 kg over a dwelling time of 30 seconds was laid on the samples through a diamond indenter. The indentation was observed with an attached optical microscope, and diagonal lengths were measured. An average of 5-10 readings was taken at random positions on the samples. Vickers hardness(HV) was calculated using the following formula.

$$HV=1.854\,\frac{F}{d^2} \qquad \text{(Eq. 3.9)}$$

where, F= applied a load (Kgf), d=average length of the diagonals (mm).

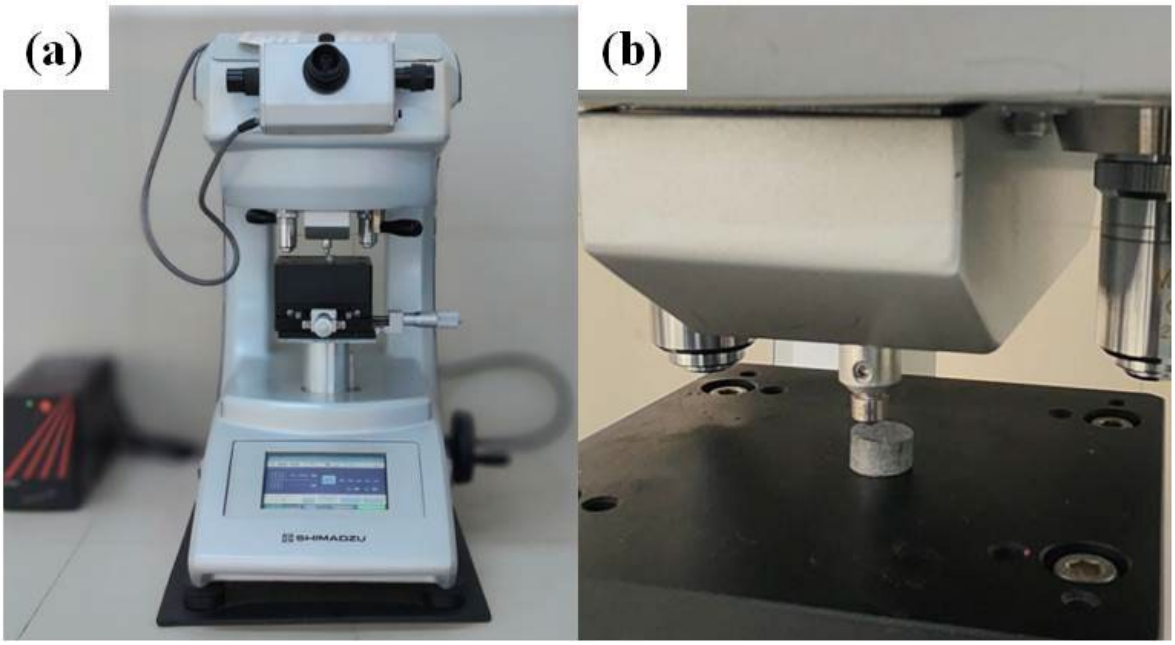

Figure 3.16. (a) Vickers Hardness testing machine and (b) Close up view of the sample with diamond pyramid indenter.

3.4.4.2 Compression and tensile testing:

The uniaxial tensile and compressive tests were carried out on a JINAN WDW-100S machine equipped with computer control (**Figure 3.16**). The tests were carried out on all the as-extruded samples of different alloy systems at room temperature with an initial strain rate of 1×10^{-3} s^{-1} with loading along the extrusion direction. The compression samples were cylindrical in shape with a 5 mm diameter and 7.5 mm height. The samples were ensured to be flat on both sides and slightly polished with fine 2000 grit emery paper to clear any oxide layers present on the surface. Tensile test samples were dog bone shaped cylindrical bars with a gauge length of 10 mm and diameter of 3 mm. Three tests were conducted for each condition and the average value was reported. The 0.2 % proof stress, ultimate strength and % elongation were evaluated from the obtained test data.

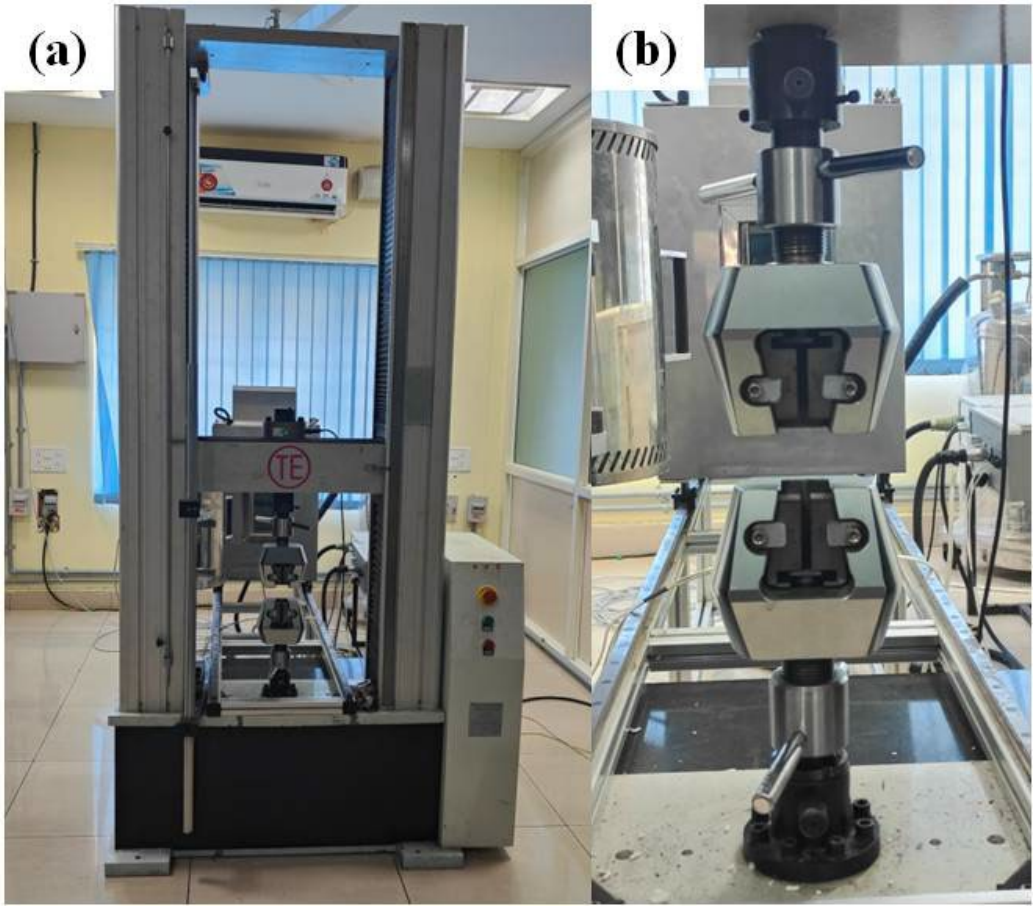

Figure 3.17 (a) Universal Testing Machine for performing tensile and compressive tests (b) tensile grips.

4

Effect Of Li On The Formation Of LPSO Phases in Mg-0.5Ni-2.5Gd-xLi (0, 1, 5, 10, 15, And 25 at. %) Alloy System

As mentioned in Chapter 2, several systematic studies have been conducted in the Mg-Zn-RE (RE – rare earth) system to comprehend the formation of LPSO phases and changes in their volume fraction and the variation in mechanical properties at room and elevated temperatures [1,2]. The important processing steps involved in the cast Mg-Zn-RE system are the solutionisation treatment and subsequent aging process where the LPSO phase is being precipitated. Since Zn has a high solubility in Mg, the LPSO phase stability at high temperatures is low. To increase the stability of LPSO phases Mg-Ni-Gd system has been investigated by several authors and found that the LPSO has high stability due to sluggish diffusion of Ni in the Mg-matrix [3,4]. Due to the high densities of Zn, Ni & Gd the overall alloy density is also found to be increasing with increasing their amounts in the alloy. Reduction of the alloy density can be achieved by adding another element with a much lower density even compared to Mg. Even though there are several elements, Li is conventionally used to lower the density, e.g., Mg-Li alloys [5].

Hence, this Chapter majorly deals with the effect of Li addition on the microstructural features (e.g., LPSO formation, grain size, Mg_3Gd, Mg_5Gd & Mg_2Ni intermetallics) and mechanical properties of Mg-0.5Ni-2.5Gd (at. %) alloy. The alloys were cast using a Vacuum Induction Melting furnace and extruded to refine the grain size as well as to reduce the casting defects. Subsequently, the influence of these parameters on the microstructural features and mechanical properties has been studied.

4.0 Preparation of cast alloys:

The compositions, i.e., Mg-0.5Ni-2.5Gd-xLi (0, 1, 5, 10, 15, and 25 at. %) or Mg-1.1Ni-14.6Gd-xLi (0, 0.25, 1.29, 2.66, 4.13 and 7.4 wt. %) were prepared in the current study and have been given in Table 1. Accordingly, the desired amounts of Mg, Li, a master alloy of NiGd and Gd was taken in a mild steel crucible. Melting was performed under a high argon pressure in a Vacuum Induction Melting Furnace and cast in a mild steel mold, a detailed procedure has been given in Chapter 3.

4.1 Elemental Analysis using ICP-OES:

The chemical constitution of the casted alloys was evaluated using Inductively Coupled Plasma – Optical Emission Spectrometry (ICP-OES) technique. It was found to statistically agree with the nominal composition according to which the alloys were designed. Due to the limitation of the detector used in the SEM–EDX, the presence of Li in the current alloys cannot be done, hence ICP-OES was performed on the alloys.

Table 4.1. Alloy designation, nominal and actual compositions of investigated Mg-0.5Ni-2Gd-xLi alloys having different amounts of Li.

Alloy Designation	Nominal composition	Actual Composition
0Li	Mg-2.5Gd-0.5Ni	Mg-2.48Gd-0.26Ni
1Li	Mg-2.5Gd-0.5Ni-1Li	Mg-2.37Gd-0.22Ni-1.04Li
5Li	Mg-2.5Gd-0.5Ni-5Li	Mg-2.56Gd-0.22Ni-5.23Li
10Li	Mg-2.5Gd-0.5Ni-10Li	Mg-2.47Gd-0.21Ni-10.09Li
15Li	Mg-2.5Gd-0.5Ni-15Li	Mg-2.39Gd-0.22Ni-15.45Li
25Li	Mg-2.5Gd-0.5Ni-25Li	Mg-2.45Gd-0.22Ni-26.39Li

4.2 Analysis of Phases:

The XRD patterns in Figure 4.1 show the evolution of phases of the Mg-0.5Ni-2.5Gd-xLi alloys in as-cast and as-extruded states. All the alloys comprise of α-Mg and Mg_3Gd phases in both as-cast as well as in as-extruded conditions. In the case of 15Li and 25Li, extra peaks corresponding to the β-Li were observed. The intensity of β-Li peaks was increasing with an increase in the lithium content, indicating a raise in the volume fraction of this phase. After extrusion, the peak intensities of Mg_3Gd were found to be smaller than the as-cast condition, indicating that there is dissolution in to the matrix and/or transformation to the LPSO phase, thereby changing its volume fraction. LPSO phase was found to be present in all the alloys, i.e., in as-cast and as-extruded conditions and its volume fraction was found to be declining with the increase in the Li content. A slight change in the intensities of α-Mg and β-Li peaks after extrusion implies that the thermo-mechanical process affects the alloy's texture.

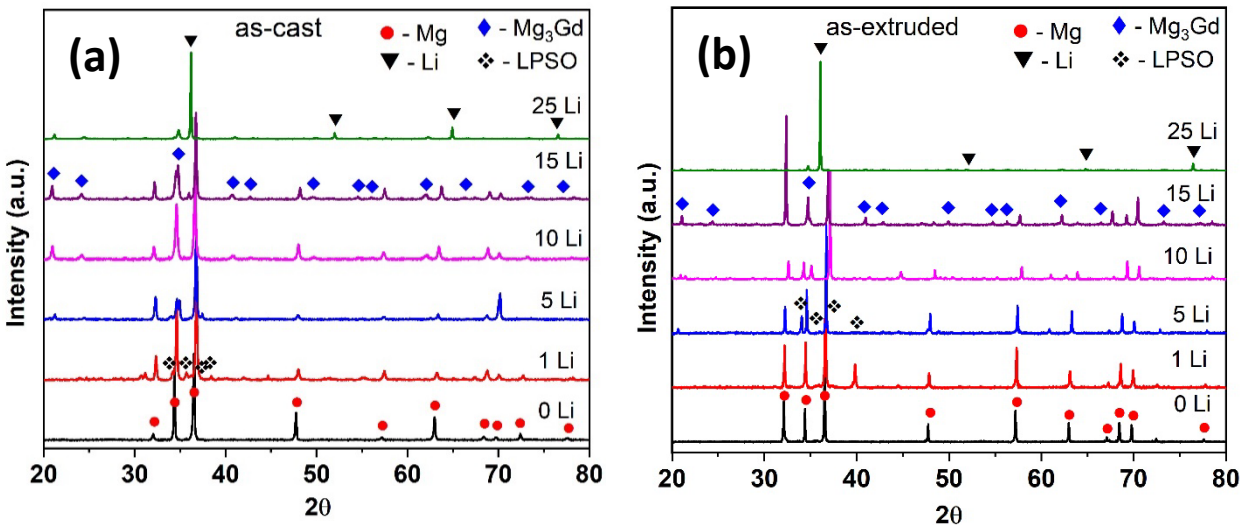

Figure 4.1. XRD patterns show the evolution of phases in as-cast and as-extruded conditions in Mg-0.5Ni-2.5Gd-xLi (0, 1, 5, 10, 15 and 25 at. %) alloys.

4.3 Microstructural Analysis:

4.3.1 As-cast Mg-0.5Ni-2.5Gd-xLi alloys:

Figure 4.2 shows the micrograph of 0Li alloy in the as-cast condition. The micrograph consists of dendrites, a quasi-continuous eutectic lamellar structure, and a light grey phase at the inter-dendritic regions. The phase with bright contrast (shown with a green arrow) in the eutectic

lamellar structure contains large amounts of Gd and the EDS analysis (**Figure 4.2b**) shows it has a composition near to Mg_3Gd. Whereas the light grey phase (shown with a red arrow) contains both Ni and Gd (**Figure 4.2c**) in it and a close inspection shows a lamellar structure indicating that this is an LPSO phase. It was evident from the micrograph that the LPSO phase formation was initiated at the interface and extended into the interior of the dendrite.

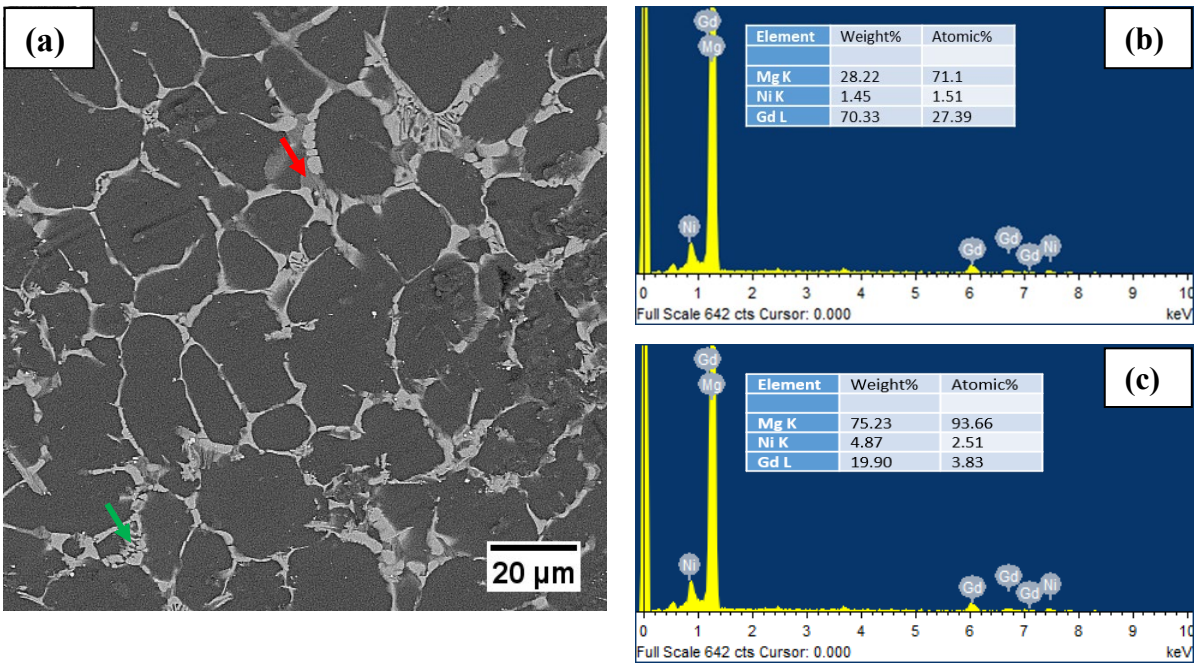

Figure 4.2. (a) SEM-BSE micrograph of 0Li as-cast material and (b) and (c) show the EDS patterns taken at the locations shown by green and red arrows

Similar features, albeit with different volume fractions, were observed in all the alloys (**Figure 4.3**), where eutectic lamellar structure consisting of Mg, Mg_3Gd phases and separate LPSO phase particles. Initially, as the lithium content increases, quantity of the LPSO phase increases, and its size decreases until 5Li (**Figures 4.3a** to **4.3c**). Later, the amount decreases continuously with increasing lithium content. Simultaneously, the volume fraction of the eutectic lamellar phase had a trend opposite to that of the LPSO phase, which initially decreased up to 5Li and then increased with increasing the Li content. In 15Li and 25Li alloys, a typical duplex structure comprising of α-Mg and β-Li was evident. The β-Li was distinguishable with lighter contrast in the matrix, and this confirms the same assertion made using the XRD patterns (**Figure 4.1**). The mean dendritic size in the as-cast alloys was around 20 microns.

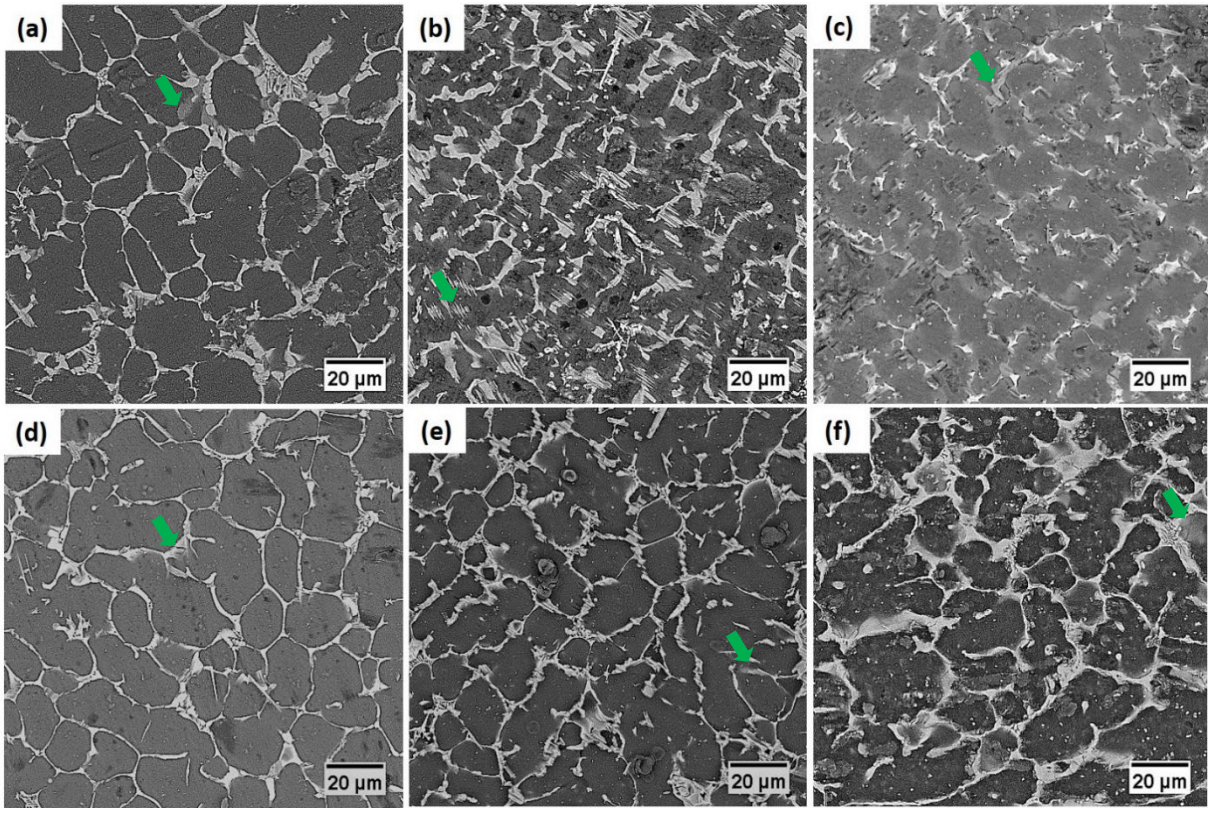

Figure 4.3. Microstructures of as-cast Mg-0.5Ni-2.5Gd-xLi alloys with varied Li content observed by SEM (BSE mode) at 1000X magnification (a) 0Li (b) 1Li (c) 5Li (d) 10Li (e) 15Li and (f) 25Li.

The microstructure of the alloys in the as-cast state shows the α-Mg dendrites, eutectic structure, β-Li and LPSO phases; this is due to the equilibrium partition coefficient, which is less than 1 as observed in the equilibrium binary phase diagrams of Mg-Li, Mg-Ni, Mg-Gd, and ternary phase diagram of Mg-Ni-Gd [3,6-9]. This means that the α-Mg phase forms first, and with a further drop in temperature and increase in Li concentration, the constitutional supercooling occurs and accumulation of solute, i.e., Ni and Gd, in front of the solid/liquid interface will increase. With a further drop in the melt temperature, the eutectic reaction takes place in the residual melts, giving rise to different volume fractions of α-Mg, β-Li, Mg_2Ni, Mg_3Gd/Mg_5Gd and LPSO phases depending on the composition [3,6-9].

The current alloys do not show the Mg_2Ni phase in either the as-cast or extruded conditions. Identical observations were put forward by Yin et al., in the Mg-Gd-Ni and Wu et al.,

in the Mg-Y-Ni systems [3,4]. Yin et al., [4] inferred that in the case of Mg-2Gd-xNi alloys, the amount of the LPSO phase increased with an increment in the Ni content up to 1 at. % and no Mg_2Ni phase was formed either after the solidification or after heat treatment at 500 ℃ for 100h. Similarly, Wu et al., [3] found that the LPSO phase forms when the Y/Ni atomic ratio is greater than one and identified the absence of the Mg_2Ni phase. Hence, the possible reason for the absence of the Mg_2Ni phase in the current alloys is due to the lower content of Ni (0.5 at. %) and higher affinity to form the LPSO phase with Gd. The excess/remaining Gd formed as the Mg_3Gd phase in the as-cast condition (**Figures 4.1 - 4.3**). In 15Li and 25Li alloys, the β-Li phase was observed next to the eutectic regions as an individual phase; some are distributed in the dendrites (**Figure 4.3f**). Nayeb-Hashemi et al., [10] comprehensively studied the Mg-Li binary system and compared the modeled and assessed phase diagram. According to this study, the alloy comprises of α-Mg only if the Li content is below 14 at. %. With further increase in Li content, both α-Mg & β-Li co-exist in different volume fractions and after 30 at. % Li, the β-Li phase is stable. On the basis of the type and amount of other element additions to the Mg-Li alloys, the eutectic reaction gives rise to a microstructure consisting of either a eutectic mixture of α-Mg and β-Li or continuous/discontinuous β-Li phase at the boundaries of the α-Mg dendrites or a mixture of both [11,12]. A minute decrease in average grain size was evident in the as-cast alloys with increased Li addition (**Figure 4.3**). Liu et al., [13] proposed that the addition of Li subdued the grain growth of α-Mg dendrites by means of solute segregation, thereby acting as a substantial grain refiner leading to finer dendrites. Jiang et al., [14] noted that modest amounts of Li addition could lead to significant grain refinement and favor the formation of secondary phases.

As per **Figure 4.3**, it was clear that Li addition after a critical amount (>5 at. %) lowered the formation of lamellar LPSO phases and favored secondary phase (Mg_3Gd) formation. It is due to the increased stacking fault energy by the addition of Li to Mg, which is crucial in generating LPSO phases. Han et al., [15] observed that the stacking fault energy of Mg-Li (46 MJ/m^2) was higher than that of Mg (33 MJ/m^2). Consequently, Gd and Ni tend to participate in the second phase development rather than forming lamellar LPSO phases with a rise in the Li content. The solubility of alloying elements also affects this phenomenon, as Mg can dissolve more Li (17 at.% @ 588 ℃) compared to Ni and Gd. Hence, a minor addition of Li to the alloy could effectively encourage the Ni and Gd precipitation in the α-Mg matrix or at the interdendritic boundaries.

4.3.2 As-extruded Mg-0.5Ni-2.5Gd-xLi alloys:

The SEM-BSE micrographs of the extruded alloys taken perpendicular to the extrusion direction are represented in **Figure 4.4** and **Figure 4.5** at the magnifications of 1000X and 5000X, respectively. The grains became finer after extrusion with respect to the as-cast alloys and are evident from the comparison with **Figure 4.3** and **Figure 4.4**, which are at a similar magnification of 1000X. The secondary phase structure was also broken and distributed uniformly throughout.

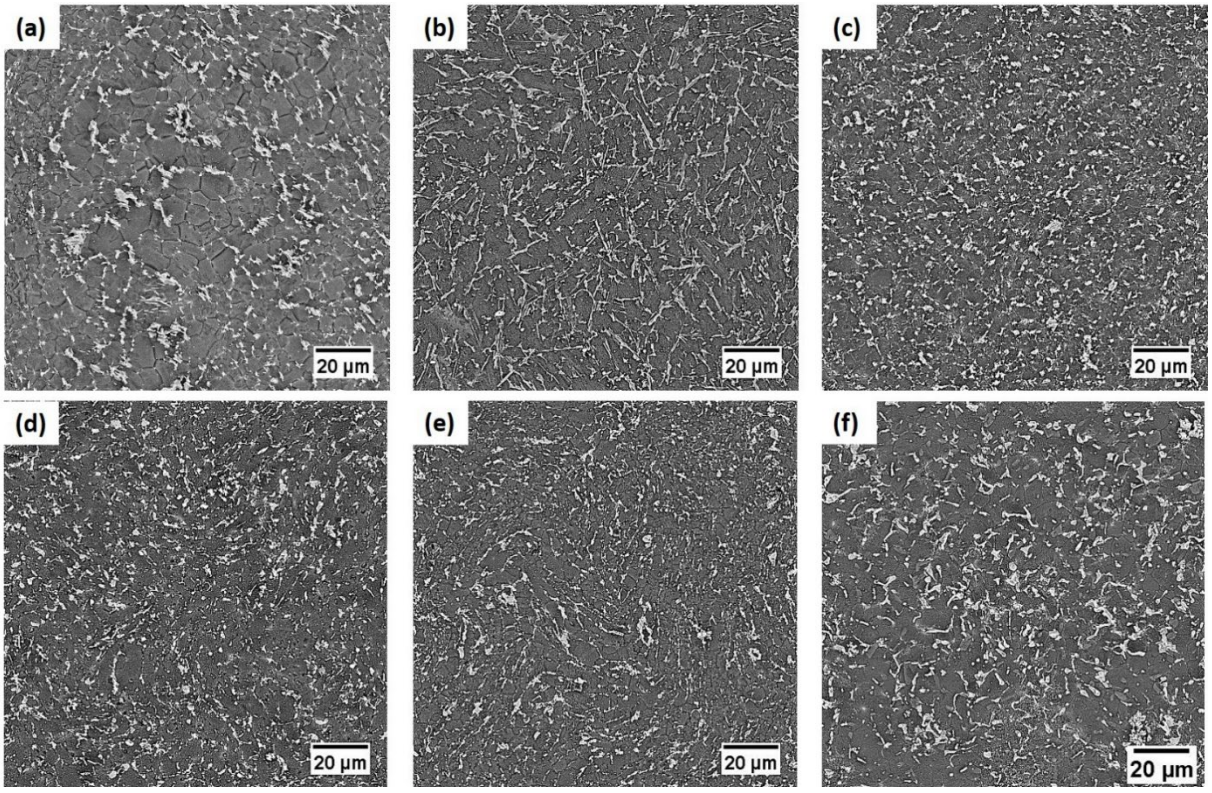

Figure 4.4. Microstructures of as-extruded Mg-0.5Ni-2.5Gd-xLi alloys with varied Li content observed by SEM (BSE mode) at 1000X magnification (a) 0Li (b) 1Li (c) 5Li (d) 10Li (e) 15Li and (f) 25Li.

Figure 4.4 and **Figure 4.5** show that the microstructure refined greatly after the hot extrusion process. Where the dendritic α-Mg transformed to fine grain size (2 to 8.4 µm), the eutectic phase in the cast condition was disintegrated to small particles and the LPSO phases were deformed and oriented along the extrusion direction. It has been reported elsewhere that hot extrusion process is beneficial in modifying microstructure [16-23]. The DRX process results in

refinement of the cast dendritic microstructure [16-20]. Second-phase particles such as LPSO phases enhance the DRX process at their grain boundaries due to the accumulation of strain because of the partitioning of the stress and the elastic modulus mismatch [21]. Rare-earth elements in the matrix enhances the dislocation density, thereby increasing the internal energy and accelerating the DRX process. Grain boundary pinning by the secondary particles such as Mg_5RE, Mg_3Gd (dynamically precipitated at the DRX grain boundaries and present in the as-cast phase), and LPSO phases reduces the grain growth resulting in the refined grain size [21,22].

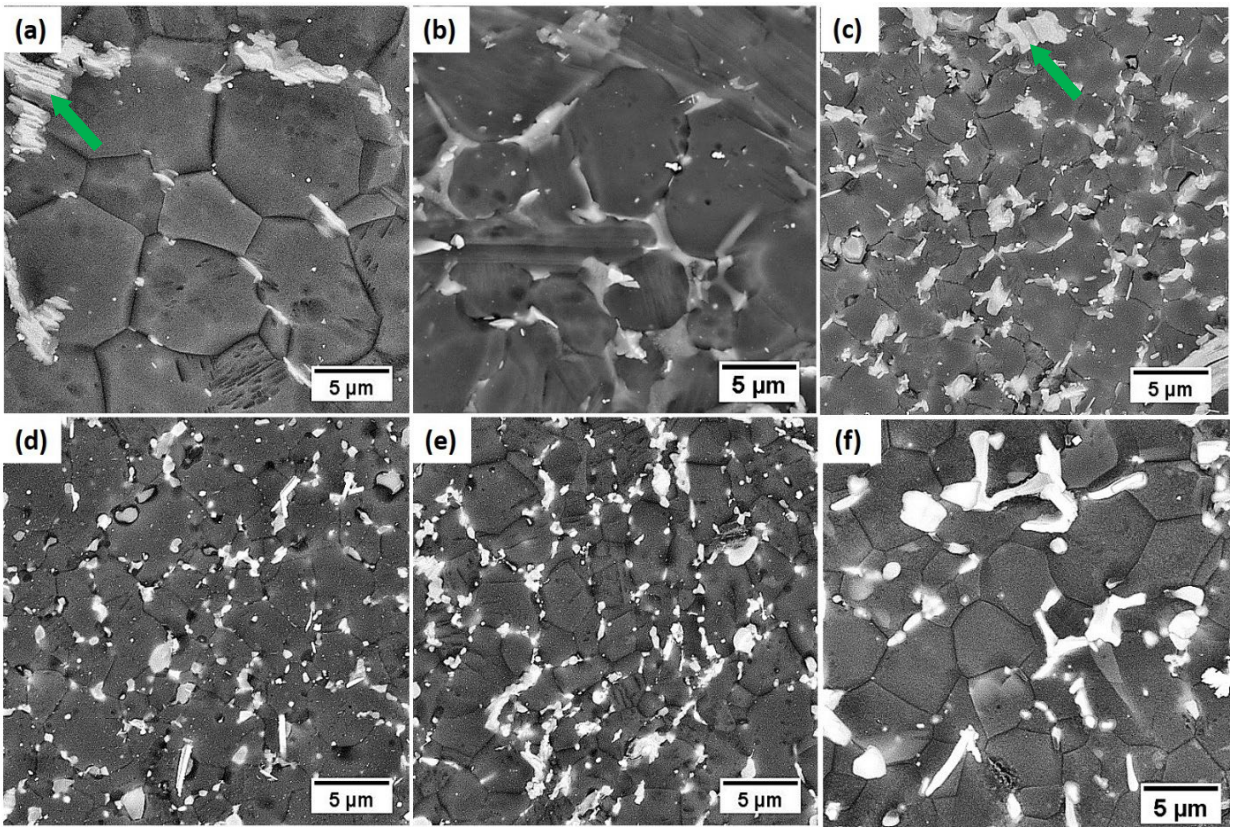

Figure 4.5. Microstructures of as-extruded Mg-0.5Ni-2.5Gd-xLi alloys with varied Li content observed by SEM (BSE mode) at 5000X magnification (a) 0Li (b) 1Li (c) 5Li (d) 10Li (e) 15Li and (f) 25Li.

Figure 4.6 shows the SEM-BSE micrographs of the extruded alloys taken parallel to the extrusion direction (indicated by a red arrow). The grain size and particle size refinement were observed in all the alloys after extrusion at 400 °C. The network of secondary phases in the as-cast alloys was broken down and dispersed along the extrusion direction in the matrix. The

micrographs show an equiaxed α-Mg matrix up to 15Li alloys and a fine grain structure of inter-dispersed α-Mg and β-Li in 25Li alloy. The grain refinement is more pronounced near the second-phase particles than in other regions. Most of the second-phase particles are elongated along the extrusion direction and distributed at the grain boundaries, whereas others are dispersed inside the grains. When the alloy content increases to 25Li, the particles consist primarily of a block-like shape.

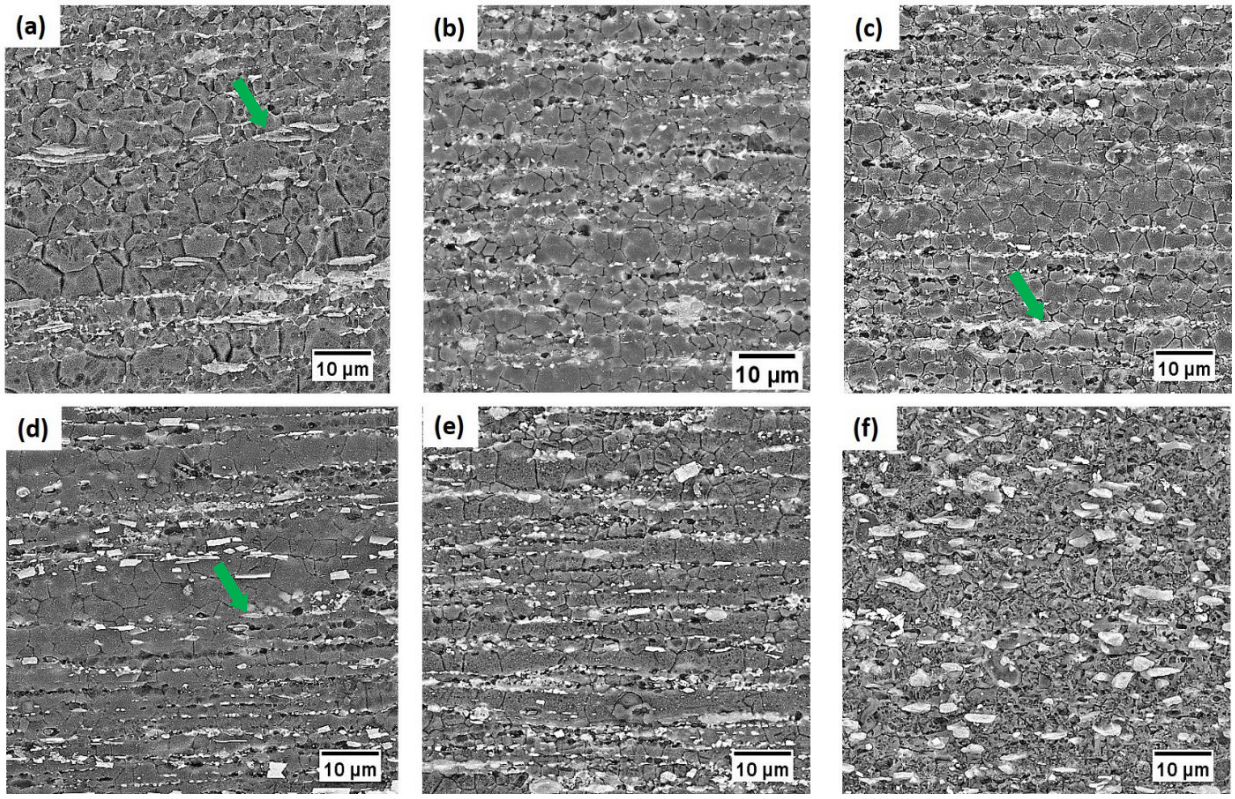

Figure 4.6. Microstructures of as-extruded Mg-0.5Ni-2.5Gd-xLi alloys with varied Li content observed by SEM (BSE mode) at 2000X magnification (a) 0Li (b) 1Li (c) 5Li (d) 10Li (e) 15Li and (f) 25Li.

During the extrusion process, dynamic recrystallization (DRX) takes place, which converts the dendritic structure to grains and imparts a significant refinement in the grain size. The volume fraction of the LPSO phases (light grey or lamellar structure) increases and decreases in size until 5Li. With a further increase in lithium content, the LPSO volume fraction decreased gradually, and the lamellar structure changed to a block-like structure. The bright particles were found to be made of Mg_3Gd, and their sizes, as well as volume fraction, were

decreased considerably when compared with the as-cast structure. Another distinct feature was that the Mg_3Gd phase was present either in the middle of the LPSO phase or at the edges of the LPSO phase, suggesting that the LPSO phase has grown by consuming the Mg_3Gd phase (shown with green arrows in **Figure 4.5**). The same is in line with the XRD plots (**Figure 4.1**), where, after the extrusion, the peak intensities of the Mg_3Gd phase were found to decrease.

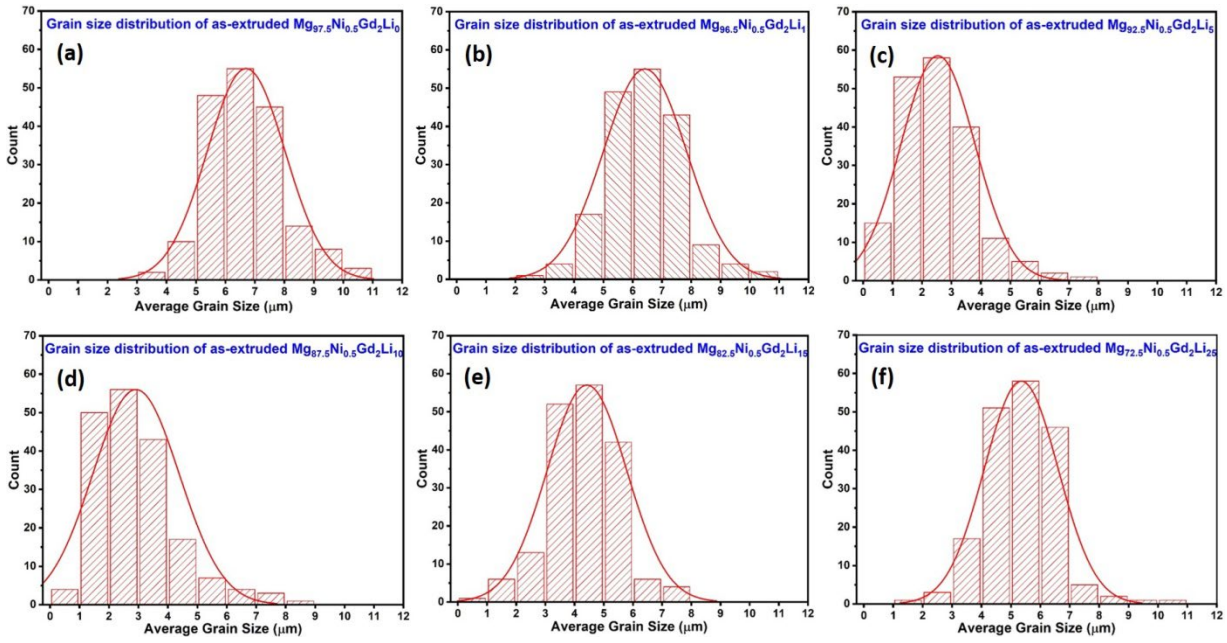

Figure 4.7. Grain size distributions of as-extruded Mg-0.5Ni-2.5Gd-xLi alloys with varied Li content (a) 0Li (b) 1Li (c) 5Li (d) 10Li (e) 15Li and (f) 25Li.

The line intercept method was employed to quantify the grain size in the microstructures taken perpendicular to the extrusion axis of the alloys. The as-extruded alloys had a mean grain size of 7.8, 6.1, 2.1, 4.5, 5.3, and 8.4 μm for 0Li, 1Li, 5Li, 10Li, 15Li, and 25Li, respectively (**Figure 4.7**). The average grain size initially decreased to as low as 2.1 μm for 5Li and gradually increased with higher Li content, up to 25% (25Li). This change might be due to the greater pinning forces acting on the grain boundaries by the Mg_3Gd and high-volume fraction of LPSO particles. When the second phase volume fraction decreases, the grains grow slightly higher. Also, in the 25Li extruded alloy (**Figure 4.6f**), it was observed that the particles inside the grains

had different contrast, and these were formed by the precipitation of either hcp-Mg in bcc-Li (slightly bright contrast) or bcc-Li in hcp-Mg (darker contrast) as per the phase diagram.

4.3.3. Evaluation of Microstructural Phases through TEM:

Figure 4.8 shows the TEM bright field image of the 5Li alloy. The micrographs show the existence of numerous stacking faults (**Figure 4.8a**) and an LPSO phase (**Figure 4.8b**) at the grain boundaries. The SAED patterns reveal the LPSO phase's existence, i.e., extra spots between the major reflections (**Figure 4.8b**). The TEM microstructures of the extruded alloys (0Li, 5Li, 10Li and 25Li) are shown in **Figure 4.9**. **Figures 4.9a** to **4.9c** show the LPSO lamella (green arrows) originating either from the grain boundaries or at the Mg_3Gd particles present at the grain boundaries and growing into the matrix. Block-like particles at the grain boundaries and sub-micron particles in the matrix were observed (blue arrow) in the case of 25Li alloy (**Figure 4.9d**). Along with the particles, the strain contrast due to dislocation is also visible near the particles in all the images.

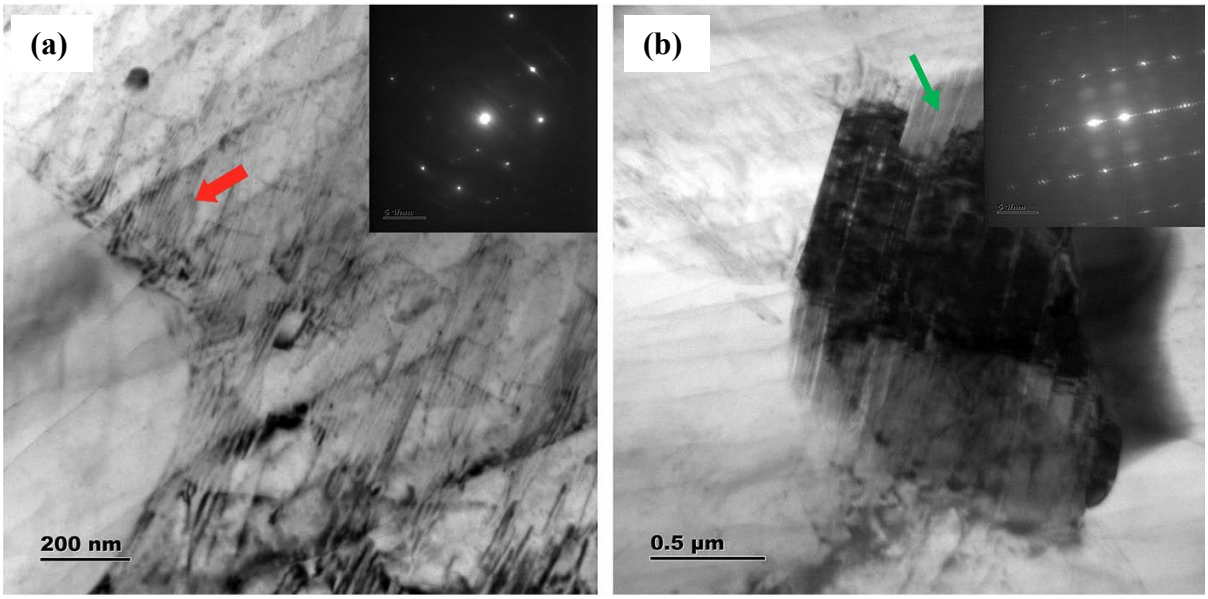

Figure 4.8. Transmission electron micrograph images of as-extruded Mg-0.5Ni-2.5Gd-5Li alloy showing the (a) stacking faults and (b) LPSO phase at the grain boundary.

The LPSO volume fraction varied with the addition of Li content of the hot extruded alloys, where the volume fraction was increased up to 5Li and then decreased. The formation of an additional LPSO phase during the hot extrusion is either due to the dissolution or transformation of the eutectic phase. The mechanism for the nucleation and growth of LPSO consists of initially forming the dislocations and stacking faults at the grain boundaries (**Figure 4.8a**). The generated dislocations and stacking faults are good pathways for diffusing TM and RE elements from the grain boundaries or the eutectic phases and act as nucleation sites for the LPSO phase. Hence, LPSO forms on the grain boundary and enlarges into the grain [22, 24-27].

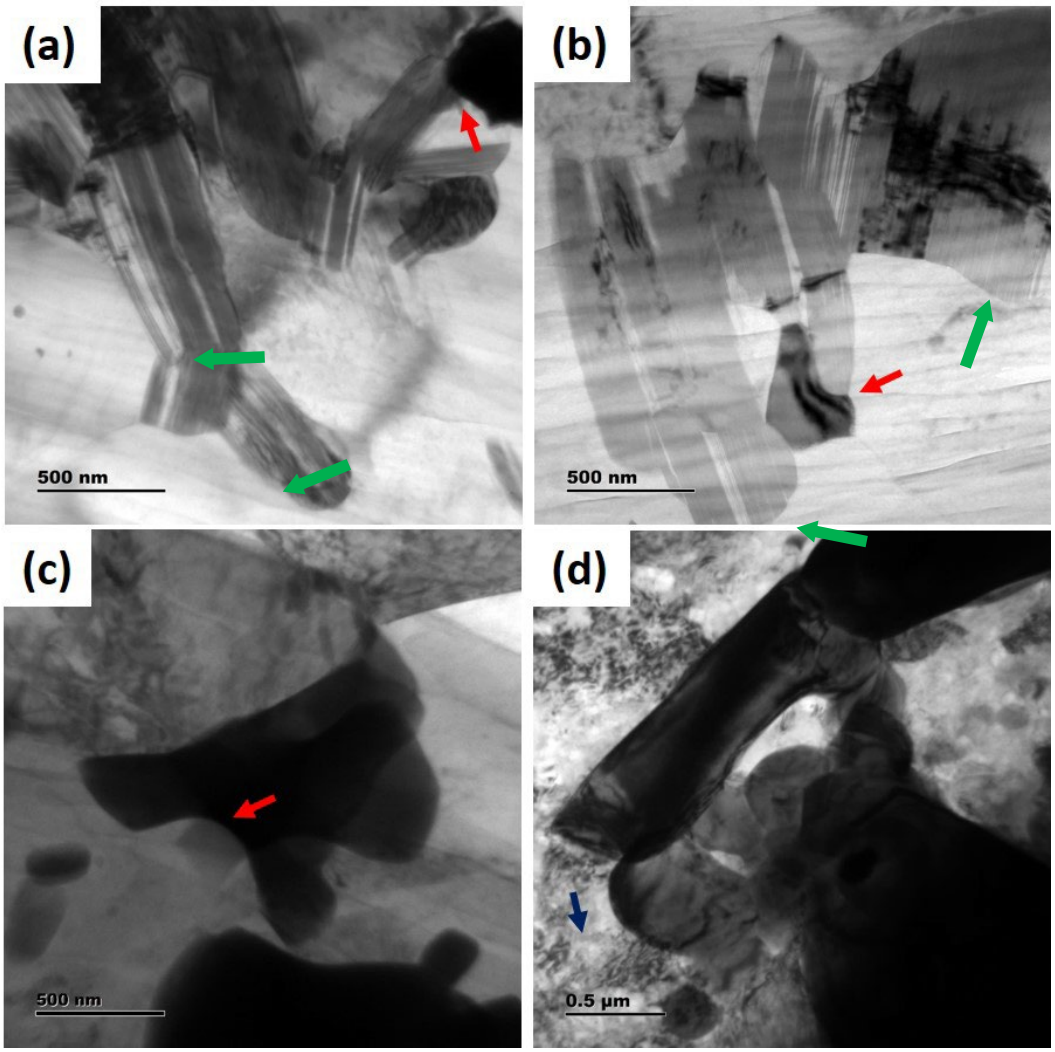

Figure 4.9. Transmission Electron Micrograph images of as-extruded Mg-0.5Ni-2.5Gd-xLi alloys with varied Li content, (a) 0Li (b) 5Li (c) 10Li and (d) 25Li. respectively.

Lu et al., [24] suggest that the dissolved RE elements (e.g., Y) and TM element (e.g., Zn) supersaturate in the Mg matrix and create a stress field around them and during the extrusion process; they interact with the dislocations and increase the number density. Liu et al., [26] suggest that due to the difference in Young's modulus of LPSO and α-Mg matrix, i.e., 67 GPa and 40 GPa, respectively, a large amount of elastic modulus mismatch will be generated during the extrusion process, this, in turn, gives rise to dislocation generation and also stacking faults. The presence of Zn, Y and Gd atoms lowers the stacking fault energy of the dislocations on (0001) α-Mg habit place, thereby generating more stacking faults and hence more LPSO phase formation. It was observed that in Mg-Zn-Y and Mg-Zn-Gd alloys, Li addition initially increases the amount of the lamellar LPSO phase, but after a critical amount, the lamellar LPSO formation was suppressed [27,28]. Since adding Li enhances the stacking fault energy, the formation of stacking faults becomes more difficult, which is an essential criterion for the formation of the lamellae LPSO phase. Indeed, it was observed in the current study that up to 5Li, numerous stacking faults were observed in the matrix; upon a further increase in the Li content, the density of stacking faults decreased enormously. Hence only the block-like LPSO phases were observed at the grain boundaries at high Li alloys (**Figures 4.5** and **4.6**) [15].

4.4 Physical and Mechanical Properties

4.4.1 Density:

Changes in the density of the as-extruded alloys were measured and are shown in **Figure 4.10a**. Ni and Gd being heavier than the parent element Mg (1.738 g/cc), raised the density as high as 1.94 gm/cc in 0Li and 1Li alloys compared to standard AZ31. The increased percentage of Li significantly reduced the alloy's density compared to pure magnesium, which is ascribed due to lithium's low density (0.534 g/cc). In alloys 15Li and 25Li, the alloy density was as low as 1.76 gm/cc and 1.61 gm/cc, respectively.

4.4.2 Hardness:

Initially, hardness decreased slightly and increased with increased lithium content up to 5 at. % and reduced afterward as shown in **Figure 4.10b**. When the Li content was 5%, the

hardness reached its maximum value, i.e., a 17% increase compared with an alloy having 0% Li. With further increase in the Li content, the hardness decreased drastically to a value as low as 54 HV, due to the increase in the soft β-Li phase in the alloy and reduction in the amount of lamellar LPSO phases, confirmed by XRD as well as microstructural studies.

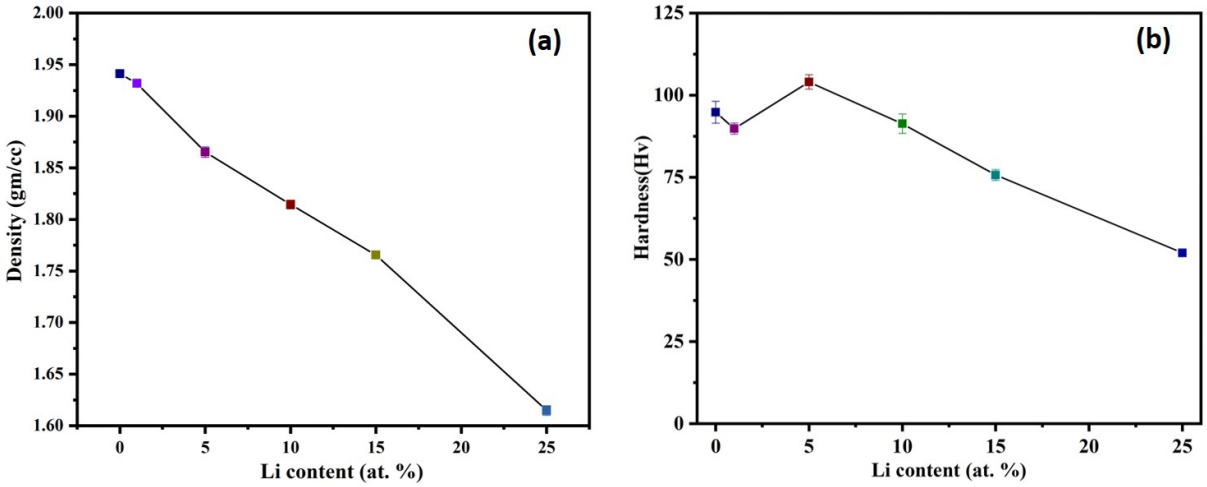

Figure 4.10. Variation of (a) density and (b) hardness with increasing Li content in the as-extruded Mg-0.5Ni-2.5Gd-xLi alloys.

4.4.3 Tensile Testing at room temperature:

Typical tensile and compressive stress-strain plots of extruded Mg-0.5Ni-2.5Gd-xLi alloys tested at ambient temperature are depicted in **Figure 4.11**, and the corresponding calculated mechanical properties are shown in Table 4.2. The tensile yield strength i.e., 0.2% yield stress, decreased slightly after adding 1 at. % Li and then increased to 5 at. % Li. Further addition of Li content reduced the tensile YS, which aligns with the observed trend in the hardness values (**Figure 4.10b**). Maximum YS and UTS of 302 MPa and 347 MPa were obtained for 5Li alloy, which is a 12% increase in tensile yield strength compared to the base alloy, i.e., 0Li alloy. The mechanical property enhancements can be accredited to the synergy of secondary phases like LPSO and Mg_3Gd along with the fine dynamically recrystallized grains. A significant increase in the total elongation and strain softening behaviour in the 25Li alloy was mainly due to the β-Li phase.

Mechanical properties of Mg-TM-RE alloys can be enhanced either by an individual or a synergy of solid solution strengthening, nano-spaced stacking faults, grain size refinement,

precipitation and dispersion hardening mechanisms [29-33]. Han et al., [34] explored the mechanical properties of cast $Mg_{96.0}Gd_{3.0}Ni_{1.0}$ (at. %) alloy and found that the alloy shows tensile yield stress, UTS and elongation values of 175 MPa, 266 MPa and 10% respectively in as-cast condition. In contrast, the current extruded alloy $Mg_{97.5}Gd_{2.0}Ni_{0.5}$ shows increased yield strength, UTS and elongation values (Table 4.2). The increase in strength values might be ascribed to grain refinement of the matrix phase from 20 µm to 6.5 µm, refinement and increased volume fraction of LPSO phases both at grain boundaries and in the matrix. An increase in the yield strength due to the reduction of grain size, i.e., the Hall-Petch relationship, was well studied elsewhere and observed that the final grain size, either close to 1 µm or lower, gives rise to the enhanced strength values [35].

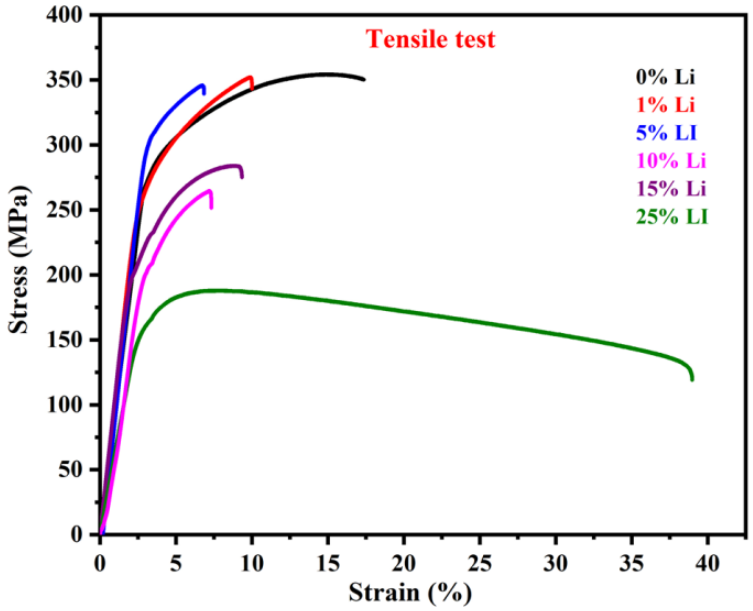

Figure 4.11. Typical tensile stress-strain curves of as-extruded Mg-0.5Ni-2.5Gd-xLi alloys with varied Li content.

The LPSO phase is harder than the Mg matrix, and acts as a strengthening phase for the Mg matrix [36].The decrease in size and increase in volume fraction of the LPSO phase and their dispersion in the matrix (**Figure 4.4**) actively hinder the motion of dislocations, thereby improving the strength of Mg alloys. Unlike other intermetallic phases, the LPSO phase could deform by forming deformation kinks, thereby contributing to elongation and reducing the propensity to form cracks due to its fracture. The alignment of the long LPSO phase (**Figure 4.6**)

and its inherent deformation capability, in turn, increase the effectiveness of pinning the dislocations during the plastic deformation, which was the main reason for the observed ductility [13,24,36]. The occurrence of substantial high volume fraction of the LPSO phase at the grain boundaries, especially the blocky particles would also not be recommended as they can act as a preferred site for the generation of cracks during tensile tests due to the development of stress concentration [34,24].

Table 4.2. Tensile properties of the as-extruded Mg-0.5Ni-2.5Gd-xLi alloys with variation in Li content.

Li content in the alloys (at. %)	0.2% Yield Strength (MPa)	Ultimate Strength (MPa)	Total Elongation (%)
0Li	269±1	359±2	14.4±1.6
1Li	242±2	352±1	9.9±0.2
5Li	302±1	347±1	5.2±0.6
10Li	201±1	265±2	7.3±0.5
15Li	200±0	285±2	8.5±0.7
25Li	167±1	188±1	37.5±1.0

Addition of Li up to 5 at. % shows a decrease in the size and increase in the volume fraction of the LPSO phase in the matrix. Due to grain size refinement (~2μm), precipitation, and dispersion of the LPSO and Mg_3Gd phases, enhanced YS and UTS values were 302 MPa and 347 MPa, respectively. Similar results were observed in other works, albeit the critical amount of Li varies depending on the alloy system [13,28,37]. It has been proposed that the solubility of Li in the matrix has a greater influence on the formation of the amount of stacking faults and at lower Li content, the effect is small on the decrease in the number density of stacking faults [28]. Since the lamellar LPSO phase formation depends on the lower stacking fault energy and the formation of a high number density of stacking faults, the presence of higher amount of Li retards the LPSO phase formation (**Figure 7**). However, for the block-shaped LPSO phase at the grain boundaries, the addition of Li has a negligible effect. Henceforth, higher Li-content alloys show an increasing density of block-shaped LPSO particles at the grain boundaries. Therefore, the contribution of highly effective precipitation strengthening by the lamellar LPSO phase was

decreased and only the dispersion strengthening of the block-like LPSO phase is active in the higher Li content alloys. This was the main reason for the decrease in the yield strength of the higher Li-containing alloys.

4.5 Summary:

The microstructure evolution and mechanical properties of cast and extruded Mg-0.5Ni-2.5Gd-xLi (x = 0, 1, 5, 10, 15, and 25 at. %) alloy systems were studied using different techniques to evaluate the effect of Lithium on the formation of LPSO and other secondary phases like Mg_3Gd. In the as-cast state, the eutectic phase existed as a quasi-continuous network along the dendritic boundaries of α-Mg and LPSO phases. Initially, with an increase in Li content, the lamellar LPSO phase was dominant compared to the eutectic phase up to 5 at.%, further increase in Li content leads to Mg_3Gd and eutectic phases when compared to the LPSO particles in the as-cast condition. The hot extrusion process leads to grain size refinement due to dynamic recrystallization and the crushing, breaking and uniform dispersion of second-phase particles (Mg_3Gd and LPSO phases). A high yield strength of 302 MPa was achieved in 5Li alloy, which can be ascribed to the fine grain size (around 2 microns), and uniform distribution of the Mg_3Gd phase and LPSO phases. A tensile ductility of 37.5% was attained in 25Li alloy due to the presence of β-Li, a soft bcc phase.

References:

[1] Lu, Fumin, et al. "Review on long-period stacking-ordered structures in Mg-Zn-RE alloys." *Rare Metals* 31 (2012): 303-310.

[2] Ross, N. G., M. R. Barnett, and A. G. Beer, "Effect of alloying and extrusion temperature on the microstructure and mechanical properties of Mg–Zn and Mg–Zn–RE alloys." *Materials Science and Engineering: A* 619 (2014): 238-246.

[3] Wu, S. Z., X. G. Qiao, and M. Y. Zheng. "Ultrahigh strength Mg-Y-Ni alloys obtained by regulating second phases." *Journal of Materials Science & Technology* 45 (2020): 117-124.

[4] Yin, Jian, et al. "Investigation of two-phase Mg-Gd-Ni alloys with highly stable long period stacking ordered phases." *Intermetallics* 68 (2016): 63-70.

[5] Sun, Yue-hua, et al. "Recent progress in Mg-Li matrix composites." *Transactions of*

Nonferrous Metals Society of China 29.1 (2019): 1-14.

[6] Chakravorty, C. R. "Development of ultra light magnesium-lithium alloys." *Bulletin of Materials Science* 17 (1994): 733-745.

[7] Si, Huaijia, et al. "Stable and metastable phase equilibria in binary Mg-Gd system: A comprehensive understanding aided by CALPHAD modeling." *Journal of Magnesium and Alloys* 7.3 (2019): 501-513.

[8] Jacobs, M. H. G., and P. J. Spencer. "A critical thermodynamic evaluation of the system MG-NI." *Calphad* 22.4 (1998): 513-525.

[9] Xu, Guanglong, et al. "Phase equilibria in the Gd–Ni binary and Mg–Ni–Gd ternary systems." *International journal of materials research* 103.10 (2012): 1179-1187.

[10] Nayeb-Hashemi, A. A., J. B. Clark, and A. D. Pelton. "The Li-Mg (lithium-magnesium) system." *Bulletin of Alloy Phase Diagrams* 5.4 (1984): 365-374.

[11] Feng, Shi, et al. "Effect of extrusion ratio on microstructure and mechanical properties of Mg–8Li–3Al–2Zn–0.5 Y alloy with duplex structure." *Materials Science and Engineering: A* 692 (2017): 9-16.

[12] Yang, Yan, et al. "Influence of Extrusion on the Microstructure and Mechanical Behavior of Mg-9Li-3Al-x Sr Alloys." *Metallurgical and Materials Transactions A* 44 (2013): 1101-1113.

[13] Liu, Wei, et al. "High-performance extruded Mg89Y4Zn2Li5 alloy with deformed LPSO structures plus fine dynamical recrystallized grains." *Materials & Design* 110 (2016): 1-9.

[14] Jiang, Yan, et al. "Effect of Li on microstructure, mechanical properties and fracture mechanism of as-cast Mg–5Sn alloy." *Materials Science and Engineering: A* 641 (2015): 256-262.

[15] Han, J., et al. "Basal-plane stacking-fault energies of Mg: A first-principles study of Li- and Al-alloying effects." *Scripta Materialia* 64.8 (2011): 693-696.

[16] Chang, L. L., et al. "Microstructure and mechanical properties in an AZ31 magnesium alloy sheet fabricated by asymmetric hot extrusion." *Materials Science and Engineering: A* 496.1-2 (2008): 512-516.

[17] Hsiang, S. H., and Y. W. Lin. "Investigation of the influence of process parameters on hot extrusion of magnesium alloy tubes." *Journal of Materials Processing Technology* 192 (2007): 292-299.

[18] Wu, R. Z., Y. S. Deng, and M. L. Zhang. "Microstructure and mechanical properties of Mg–5Li–3Al–2Zn–x RE alloys." *Journal of materials science* 44 (2009): 4132-4139.

[19] Liu, X. B., R. S. Chen, and E. H. Han. "Effects of ageing treatment on microstructures and properties of Mg–Gd–Y–Zr alloys with and without Zn additions." *Journal of Alloys and Compounds* 465.1-2 (2008): 232-238.

[20] Yu, Zijian, et al. "Effects of extrusion ratio and annealing treatment on the mechanical properties and microstructure of a Mg–11Gd–4.5 Y–1Nd–1.5 Zn–0.5 Zr (wt%) alloy." *Journal of materials science* 52 (2017): 6670-6686.

[21] Xu, Chao, et al. "Effect of LPSO and SFs on microstructure evolution and mechanical properties of Mg-Gd-Y-Zn-Zr alloy." *Scientific reports* 7.1 (2017): 40846.

[22] Wang, Jingfeng, et al. "Effects of heat treatment on the morphology of long-period stacking ordered phase and the corresponding mechanical properties of Mg–9Gd–xEr–1.6 Zn–0.6 Zr magnesium alloys." *Materials Science and Engineering: A* 563 (2013): 36-45.

[23] Yu, Zijian, et al. "Microstructure evolution and mechanical properties of as-extruded Mg-Gd-Y-Zr alloy with Zn and Nd additions." *Materials Science and Engineering: A* 713 (2018): 234-243.

[24] Lu, Ruopeng, et al. "Effect of extrusion on damping and mechanical properties of Mg-Zn-Y alloy." *Materials Research Express* 7.7 (2020): 076520.

[25] Huang, Song, et al. "Effect of Gd and Y contents on the microstructural evolution of long period stacking ordered phase and the corresponding mechanical properties in Mg–Gd–Y–Zn–Mn alloys." *Materials Science and Engineering: A* 612 (2014): 363-370.

[26] Liu, Wei, et al. "Precipitation behaviors of 14H LPSO lamellae in Mg 96 Gd 3 Zn 0.5 Ni 0.5 alloys during severe plastic deformation." *Journal of Materials Science* 52 (2017): 13271-13283.

[27] Zong, Ximei, et al. "Effects of Li on Microstructures, Mechanical, and Biocorrosion Properties of Biodegradable Mg94-xZn2Y4Lix Alloys with Long Period Stacking Ordered Phase." *Advanced Engineering Materials* 19.3 (2017): 1600606.

[28] Wei, Li-yun, et al. "Effect of Li on formation of long period stacking ordered phases and mechanical properties of Mg-Gd-Zn alloy." *China Foundry* 13.4 (2016): 256-261.

[29] Homma, T., N. Kunito, and Scr Kamado. "Fabrication of extraordinary high-strength magnesium alloy by hot extrusion." *Scripta Materialia* 61.6 (2009): 644-647.

[30] Jian, W. W., et al. "Ultrastrong Mg alloy via nano-spaced stacking faults." *Materials Research Letters* 1.2 (2013): 61-66.

[31] Xu, Chao, et al. "Improving strength and ductility of Mg–Gd–Y–Zn–Zr alloy simultaneously via extrusion, hot rolling and ageing." *Materials Science and Engineering: A* 643 (2015): 137-141.

[32] Honma, T., et al. "Effect of Zn additions on the age-hardening of Mg–2.0 Gd–1.2 Y–0.2 Zr alloys." *Acta Materialia* 55.12 (2007): 4137-4150.

[33] González, Sergio, et al. "Influence of processing route on microstructure and mechanical properties of two Mg–Ni–Y–RE alloys." *Materials characterization* 64 (2012): 53-61.

[34] Han, Zhenhua, et al. "Effects of volume fraction of Ni-containing LPSO phase on mechanical and corrosion properties of Mg-Gd-Ni alloys." *Materials and Corrosion* 70.3 (2019): 537-548.

[35] Yu, Huihui, et al. "Hall-Petch relationship in Mg alloys: A review." *Journal of Materials Science & Technology* 34.2 (2018): 248-256.

[36] Xu, Daokui, En-hou Han, and Yongbo Xu. "Effect of long-period stacking ordered phase on microstructure, mechanical property and corrosion resistance of Mg alloys: A review." *Progress in Natural Science: Materials International* 26.2 (2016): 117-128.

[37] Becerra, A., and M. Pekguleryuz. "Effects of lithium, indium, and zinc on the lattice parameters of magnesium." *Journal of Materials Research* 23.12 (2008): 3379-3386.

5

Microstructure and mechanical properties of Mg-0.5Ni-0.5Zn-2Gd-xLi (x = 15, 23 and 30 at. %) alloys prepared by casting and extrusion processes

Mg-0.5Ni-2.5Gd-xLi alloys (Chapter 4) show that with the addition of Li content, the LPSO phase formation happens, but their morphology has been changed from lamellar to the block type of structure with higher Li contents. The block-type particles and Mg_3Gd are mostly situated at the grain boundaries, reducing the number density of particles inside the matrix and reducing precipitation strengthening. Also, the big Mg_3Gd particles are found to be brittle and lead to reduced elongation even in the high Li-containing alloys except for 25 at. % Li alloy where the elongation is due to the higher volume fraction of soft β – Li phase. Adding Zn as an alloying element to the Mg-Gd alloys encouraged the formation of LPSO particles profoundly [1]. By using suitable solutionizing and aging heat treatment, the LPSO phases can be refined.

Further addition of 0.5 at. % Ni to the Mg-0.5Zn-3Gd alloy show pronounced increase in the LPSO volume fraction and showed increased mechanical properties [2]. Adding Zn to Mg-Li alloys also results in the formation of MgLiZn and MgLi2Zn particles as precipitates which will enhance the material's overall strength by precipitation strengthening mechanism [3]. Hence, the study is undertaken to increase the precipitation of LPSO and secondary phases inside the matrix by replacing the partial amount of Gd with Zn in the Mg-Ni-Gd-Li system.

This chapter majorly deals with the effect of Zn and extrusion temperature on the microstructural evolution and mechanical properties of the Mg-0.5Ni-0.5Zn-2Gd-xLi system with high amounts of Li. The alloys were cast, solutionized, and extruded to the required size suitable for evaluating the microstructural and mechanical features.

The alloys having the nominal composition of Mg-0.5Ni-0.5Zn-2Gd-xLi (x = 15, 23 and 30 at. %) or Mg-1.26Ni-1.4Zn-13.47Gd-xLi (x = 4.21, 6.84 and 9.41 wt. %) were cast in a Vacuum Induction melting furnace (VIM, Vacuum technologies) under argon. The melt was allowed to stay at the temperature around 800 ℃ for 20 minutes to ensure uniformity of the alloy mixture and subsequently poured into a mild steel mold to obtain 20 mm diameter cylindrical rods. The ingot's homogeneity was ensured through stirring and confirmed by X-ray diffraction on both ends of the cast ingot and by chemical analysis with ICP-OES technique. As-cast ingots were solutionised at 510 ℃ for 48 hrs, and water quenched. Following which, the as-solutionised samples were extruded at two temperatures, i.e., 200 ℃ and 300 ℃, having a reduction ratio of 16:1. The phase, microstructural and mechanical analyses were performed to evaluate the alloys with the help of the equipment mentioned in the chapter 3 (section 3.4).

5.1 Elemental analysis using ICP-OES:

Due to the limitation of the detector available in the SEM-EDX, it was not possible to determine the amount of Li present in the current alloys. Hence, the actual composition of the alloys was determined using the inductively coupled plasma–optical emission spectrometry (ICP-OES) technique, Table 5.1 shows the nomenclature and the details of the experimentally quantified compositions of the as-cast alloys. The measured composition was found to be close to the nominal composition to which the alloys were designed.

Table 5.1. Alloy designation, nominal and actual compositions of investigated Mg-0.5Ni-0.5Zn-2Gd-xLi alloys having different amounts of Li.

Alloy Designation	Nominal composition (at. %)	Actual Composition (at. %)
15Li	Mg-2Gd-0.5Ni-0.5Zn-15Li	Mg-1.93Gd-0.5Ni-0.5Zn-14.91Li
23Li	Mg-2Gd-0.5Ni-0.5Zn-23Li	Mg-1.94Gd-0.51Ni-0.51Zn-23.19Li
30Li	Mg-2Gd-0.5Ni-0.5Zn-30Li	Mg-1.94Gd-0.48Ni-0.49Zn-30.81Li

5.2 Analysis of Phases:

The evolution of phases of the alloys in the as-cast, as-solutionised and as-extruded conditions was studied using the XRD and is shown in **Figure 5.1**. All the alloys under this study comprise of α-Mg, β-Li, LPSO and Mg_3Gd phases in all the three processing stages. The intensity of β-Li peaks was increasing with respect to lithium content, indicating a rise in the volume fraction of this phase. Peaks corresponding to the LPSO phase were observed even at higher Li contents like at 30 at. %, which was not seen in the alloy system discussed in the Mg-0.5Ni-2.5Gd-15 & 25Li (at. %) alloys (chapter 4). This phenomenon can be attributed to the presence of Zn, which justified its addition in enhancing the possibility of LPSO phase formation. Solutionization treatment gave mixed results, i.e., in the case of 15Li alloy, the Mg_3Gd phase intensity decreased (21º in **Figure 5.1**), whereas, in 23Li it has slightly increased and 30Li has no change in its peak intensity.

After extrusion, the peak intensities of Mg_3Gd were found to be smaller than the as-cast condition, indicating a dissolution and conversion to the LPSO phase, thereby changing its volume fraction. A slight change in the intensities of α-Mg and β-Li peaks post extrusion implies that the thermo-mechanical process affects the alloy's texture. Alloys extruded at 300 ℃ always show higher intensities of major phases compared to 200 ℃ extruded conditions, indicating a definitive increase in the grain size in the former condition. In the extruded condition, there is a slight change in the intensities of the LPSO phase (e.g., peak at an angle of 34º). In the case of 15Li, higher volume fractions were observed compared to as-cast and solutionized conditions. Whereas 23Li show very little change in the LPSO phase peak intensities and 30Li alloy do not show any LPSO peak intensities, this could be due to the higher peak intensity of β – Li because

of texture and masked the other peaks close to the background. Hence, the LPSO phase formation after extrusion is profoundly dependent on the alloy composition and temperature.

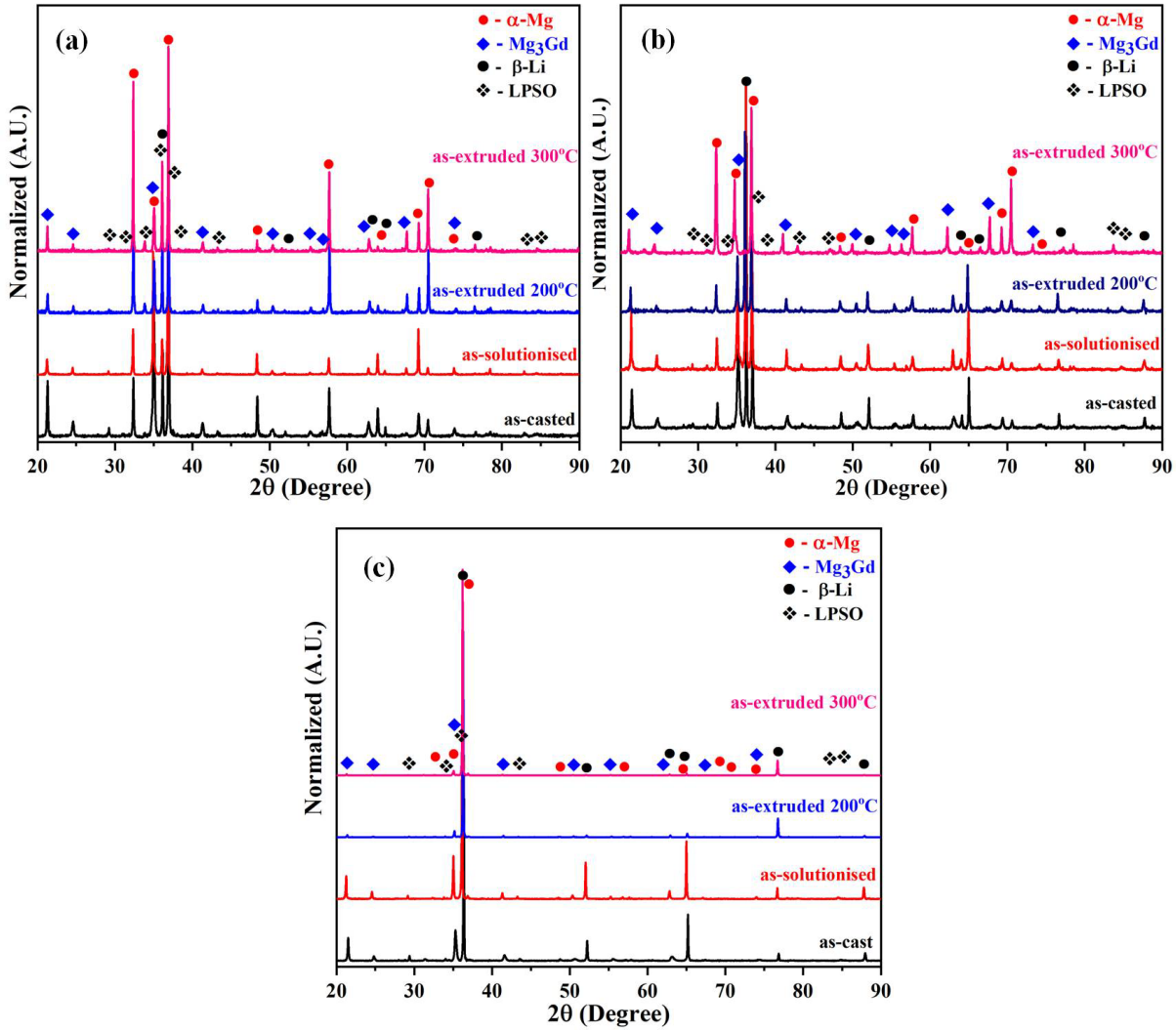

Figure 5.1. XRD patterns showing the phases at different stages of processing Mg-0.5Ni-0.5Zn -2Gd-xLi (at. %) alloys (a) 15Li (b) 23Li (c) 30Li.

5.3 Microstructural Analysis:

5.3.1 As-cast Mg-0.5Ni-0.5Zn-2Gd-xLi alloys:

Figures 5.2(a), (c), and (e) depict the SEM-BSE micrographs of 15Li, 23Li, and 30Li alloys, respectively, in as-cast state. The micrograph comprises of dendrites, a quasi-continuous eutectic lamellar structure (red arrow), and a light grey phase (green arrow) at the inter-dendritic regions. The images got less bright with the increase in Li addition as a result of

the gradual replacement of the α-Mg phase by the β-Li phase, which became predominant at higher Li alloys. The phase with bright contrast in the eutectic lamellar structure contains large amounts of Gd, whereas the light grey phase contains both Ni and Gd **(Figure 5.2(a), (c) & (e))**. The microstructure appeared to be very similar to the Mg-0.5Ni-2.5Gd-xLi alloys discussed in the previous chapter (**Chapter 4**), except for the evident existence of LPSO phases in all the current compositions. This was not the case for the higher Li alloys (15 & 25 at. %) in the previous chapter. A close inspection shows a lamellar structure indicating that this is an LPSO phase (green arrow). The addition of Zinc to the system made the formation of LPSO phases possible even at the higher Li content. It was obvious from the as-cast microstructure that the LPSO formation was observed at the interface which continued into the interior of the dendrite (**Figure 5.2b & Figure 5.2d**). The formation of LPSO phase is suppressed with increase in Li addition, yet it can be found in all the alloys. The mean dendritic size in as-cast alloys were around 14 μm, 12 μm, and 21 μm for 15Li, 23Li, and 30Li, respectively. As the lithium content increases, the volume fraction of the eutectic phase goes up, and the LPSO phase decreases. It is proven that Zn and Gd provided a better possibility of LPSO formation [4-6]. But, higher Li additions lead to reduction in the solid solutibilities of Zn & Gd, an increase in the stacking fault energy and thereby decrease the volume fraction of LPSO phase.

The as-cast microstructure shows the α-Mg dendrites, eutectic structure, β-Li, and LPSO phases; the solidification phenomenon is similar to the alloy system discussed in Chapter 4 and observed in the equilibrium binary phase diagrams of Mg-Li, Mg-Ni, Mg-Gd, and ternary phase diagram of Mg-Ni-Gd [7-11]; This means the α-Mg phase forms first, and with a further drop in temperature and increment in Li concentration, the constitutional supercooling due to the aggregation of solute, i.e., Ni and Gd, beside the solid/liquid interface will increase. With a further spike in melt temperature, eutectic reaction is initiated in residual melt, giving rise to different volume fractions of α-Mg, β-Li, Mg_2Ni, Mg_3Gd/Mg_5Gd and LPSO phases depending on the composition [7-11]. The current alloys also don't possess the Mg_2Ni phase in either the as-cast or extruded conditions similar to the Mg-0.5Ni-2.5Gd-xLi alloys. Identical inferences were put forward by Yin et al., in the Mg-Gd-Ni and Wu et al., in the Mg-Y-Ni systems [7,12]. Yin et al., [7] surmised that in the case of Mg-2Gd-xNi alloys, the volumetric fraction of the LPSO increased with an increment in the Ni content up to 1 at. % and no Mg_2Ni phase was formed either after the solidification or post heat treatment at 500 ℃ for 100h. Hence, the Mg_2Ni

phase was not observed due to the lower content of Ni (0.5 at. %) and higher affinity to form the LPSO phase with Gd. The remaining Gd formed as the Mg_3Gd in as-cast state (**Figure 5.2(a), (c) & (e)**).

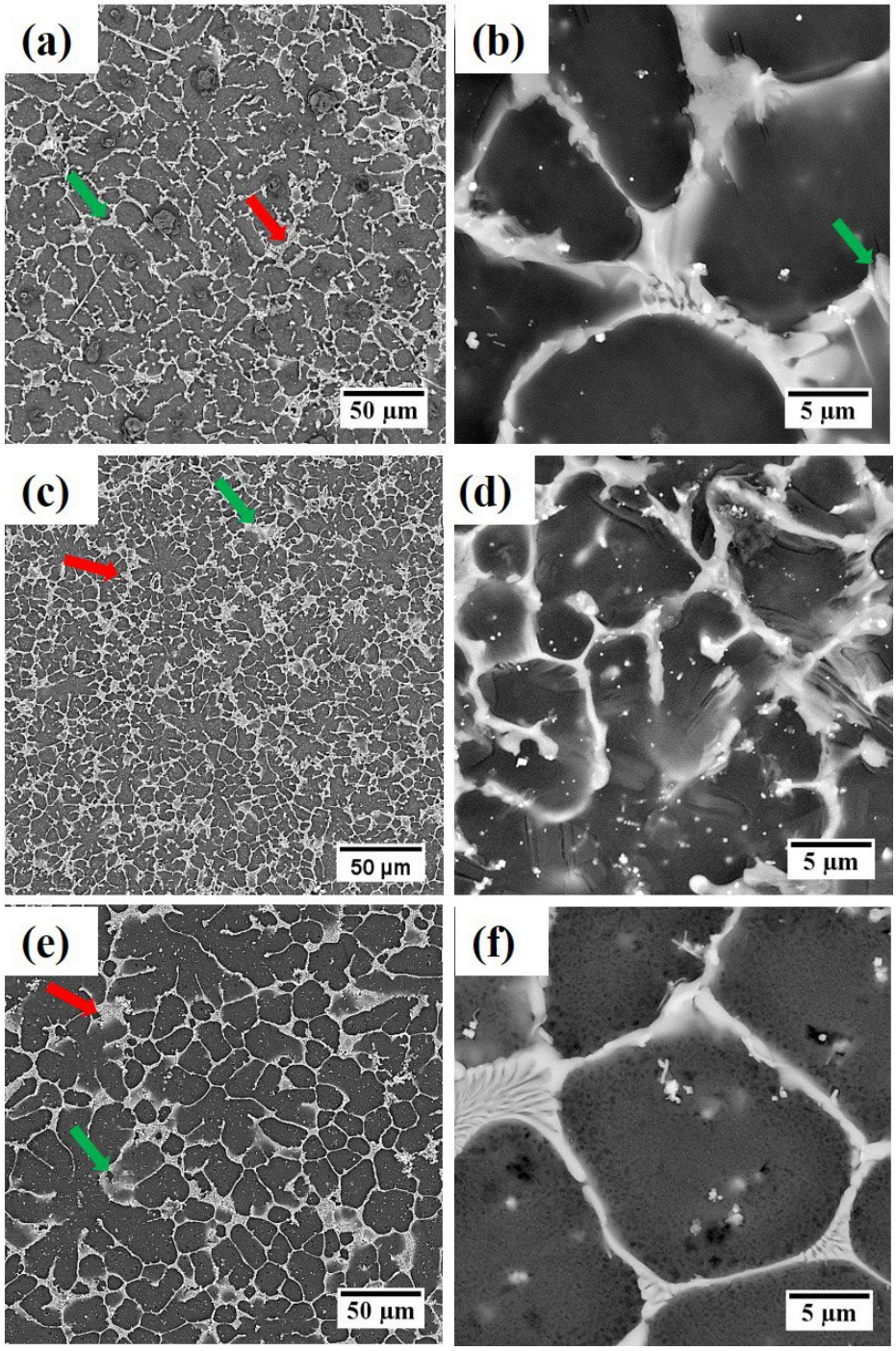

Figure 5.2. SEM-BSE Microstructures of Mg-0.5Ni-0.5Zn -2Gd-xLi as-cast alloys. (a) & (b) 15Li, (c) & (d) 23Li and (e) & (f) 30Li.

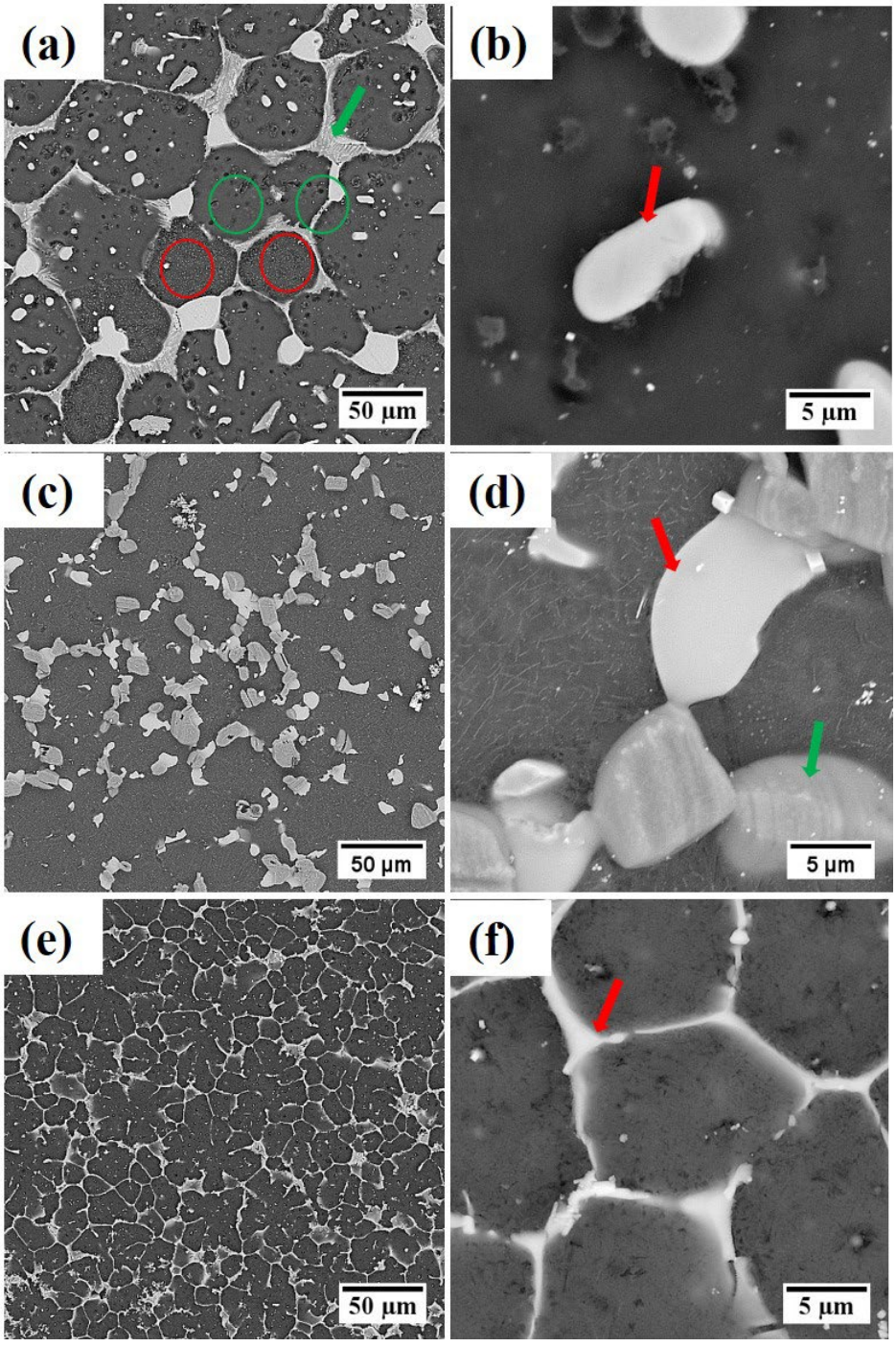

Figure 5.3. SEM-BSE Microstructures of Mg-0.5Ni-0.5Zn -2Gd-xLi as-solutionized alloys. (a) & (b) 15Li, (c) & (d) 23Li and (e) & (f) 30Li.

Figure 5.3 shows the SEM-BSE micrographs of the 15Li, 23Li, and 30Li compositions in as-solutionised state. The grain size increased dramatically due to the high-temperature exposure and dissolution of the eutectic structure in the 15Li and 23Li alloys. In the case of 15Li alloy, the eutectic network reacted with the Mg-matrix and was replaced by light grey phase (LPSO), which is complemented by the XRD data (**Figure 5.1a**). Also, two regions can be observed marked with the red circle and green circle, where the red circle shows the dark region (β-Li matrix phase) with white precipitates (α-Mg precipitates) and the green circle shows a white region (α-Mg matrix phase) with sparsely dispersed dark phase (β-Li particles). 23Li alloys (**Figure 5.3c & 5.3d**) show a single-phase matrix with dispersed particles (Mg-rich particles) and blocky (red arrow) and lamellar LPSO (green arrow) phases at the boundaries of the grains. Some amount of bright white particles still can be found around grain boundaries and it is found to be Mg_3Gd phase. Whereas 30Li alloys do not show a significant change in the microstructure after the solutionizing heat treatment. Still there is some reaction between the eutectic network and the formation of blocky LPSO phase (red arrow in **Figure 5.3f**). Hence, it can be concluded that adding Zn enhanced the formation of LPSO phases in both 15Li, 23Li and slightly in 30Li alloys.

5.3.2 As-extruded Mg-0.5Ni-0.5Zn-2Gd-xLi alloys:

The SEM-BSE micrographs of the magnesium based alloys extruded at multiple temperatures of 200 ℃ and 300 ℃ are shown in **Figures 5.4 and 5.5**, respectively. The images were taken perpendicular to the extrusion direction. The grains, which became coarser after solutionizing treatment, were refined during the hot extrusion process; this can be observed by comparing microstructures at a similar magnification. The secondary phase structure was also broken and distributed uniformly; the higher magnification microstructures provide a better view of the microstructural features in great detail. The refinement is much greater when the extrusion temperature is lower, i.e., at 200 ℃ (**Figure 5.4**). According to **Figure 5.4**, the α-Mg & β - Li (**Figure 5.4b**) transformed to fine grain size, i.e., 2.56, 4.98 and 7.45 μm for 15Li, 23Li and 30Li, respectively (**Figure 5.6**), the eutectic phase in as-cast and as-solutionized conditions were broken down to small particles, and LPSO phases were deformed and oriented parallel to the extrusion direction. In case of 30Li alloys, the solutionized condition did not show much lamellar LPSO phase, but after the extrusion process, a good volume fraction of miniscule particles of

lamellar LPSO stacks were visible at the grain boundaries (**Figure 5.4e**). Several secondary particles were present in the matrix grains and the volume fraction was found to decrease with increased Li content in alloys (**Figures 5.4b, 5.4d & 5.4f**).

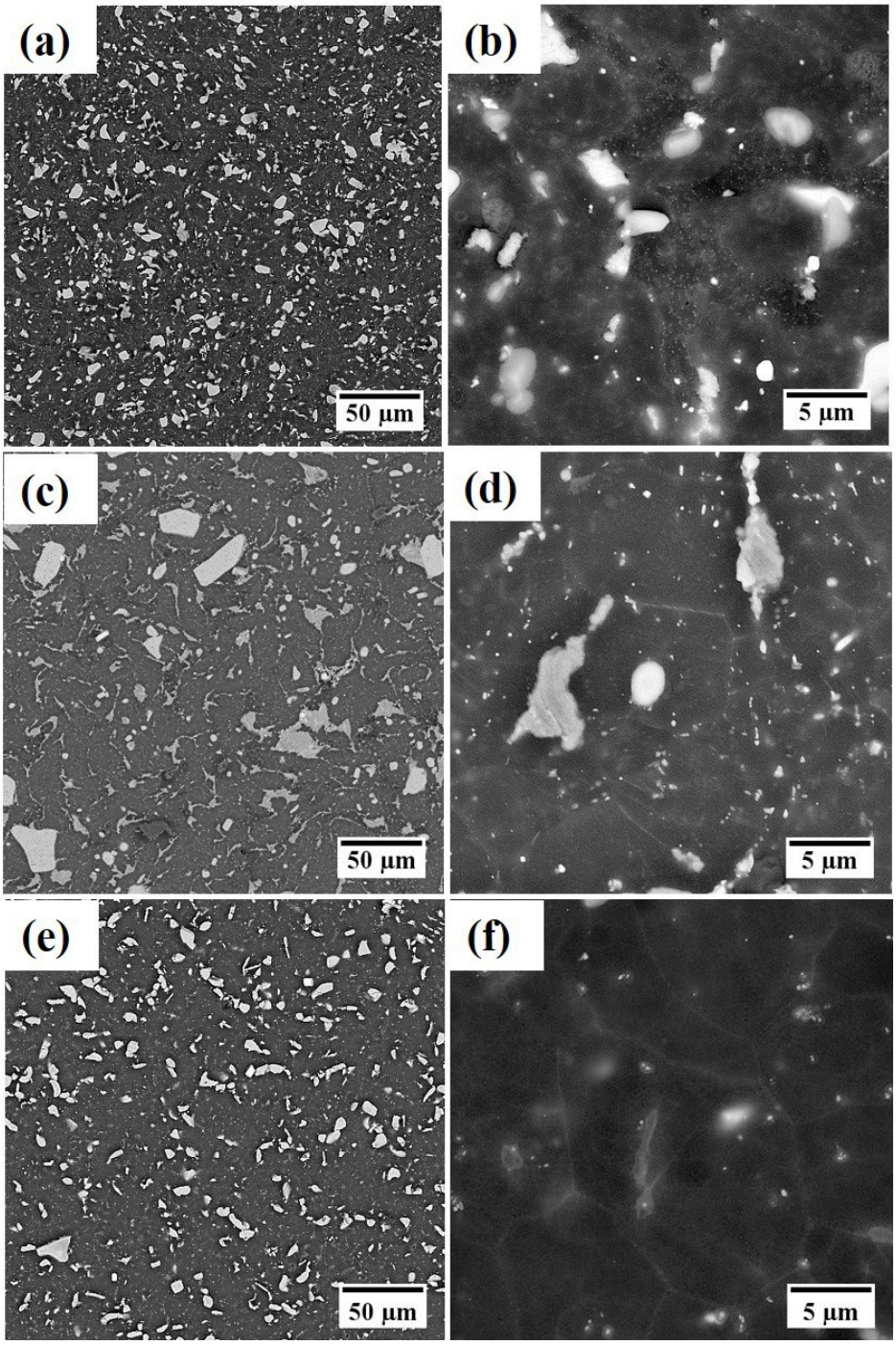

Figure 5.4. SEM-BSE Micrographs of as-extruded Mg-0.5Ni-0.5Zn -2Gd-xLi alloys at temperature 200 ℃. (a) & (b) 15Li, (c) & (d) 23Li and (e) & (f) 30Li.

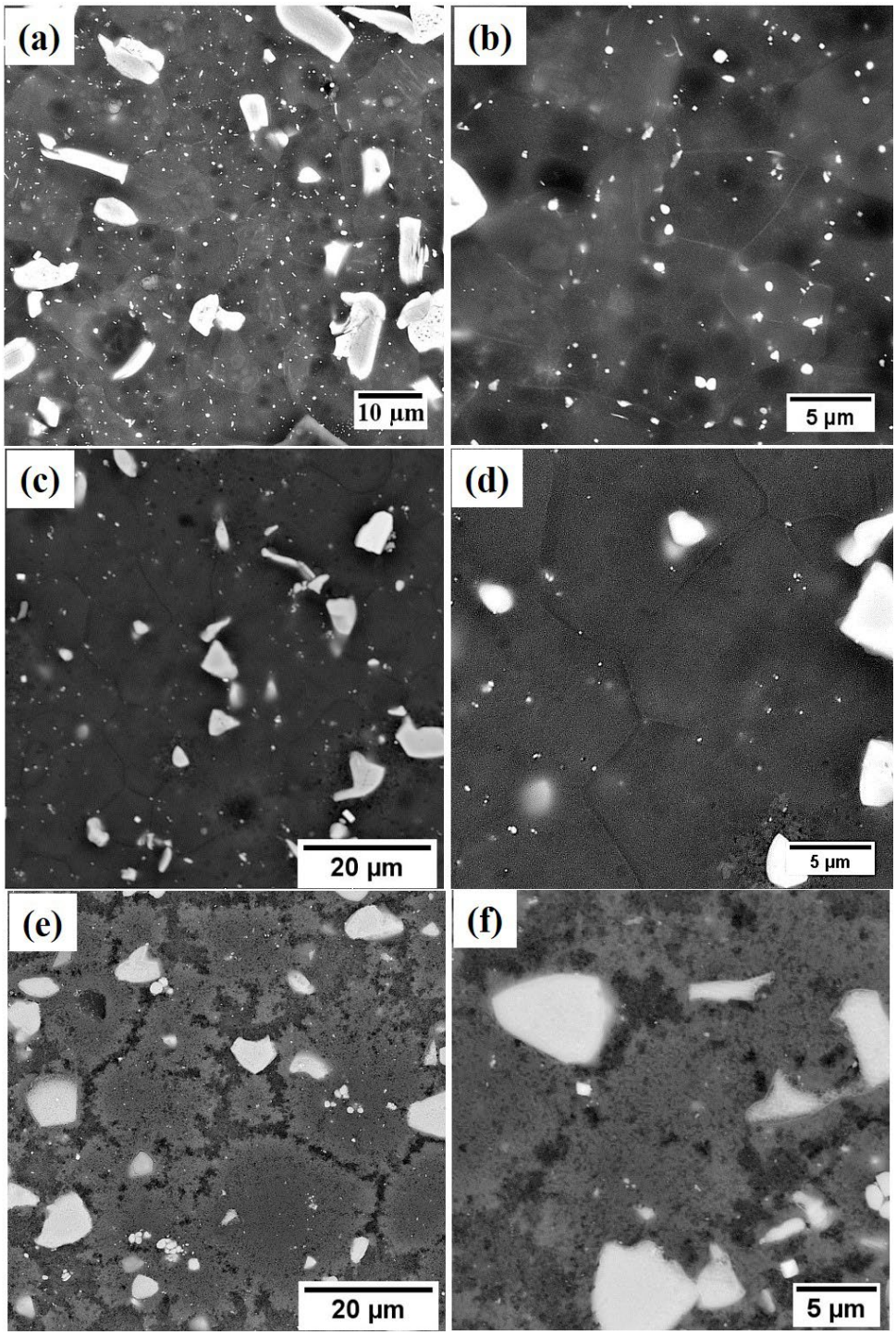

Figure 5.5. SEM-BSE Microstructures of as-extruded Mg-0.5Ni-0.5Zn -2Gd-xLi alloys at a temperature of 300 ℃. (a) & (b) 15Li, (c) & (d) 23Li and (e) & (f) 30Li.

Figure 5.5 shows the microstructural details of the alloys extruded at 300 ℃. The matrix grain size was found to be 4.74, 11.32, and 17.67 µm for 15Li, 23Li, and 30Li, respectively (**Figure 5.6**), which is a slight increase compared to the 200 ℃ extruded condition. This is due to the

higher extrusion temperature, where diffusion is higher. Similarly, the particle size of the LPSO phase and secondary phase particles dispersed in the matrix were also higher in all three alloys. The eutectic network present in the as-cast alloys was completely removed, even in the 30Li alloy. 30Li alloys occasionally show clusters of white particles (**Figure 5.5e**), which are undissolved Mg_3Gd particles and dual-phase microstructure. The decrement in the matrix grain size in all the alloys under study is due to the dynamic recrystallization (DRX) during the extrusion process [16–20]. Higher volume fractions of the second-phase particles, such as LPSO phases, enhance the DRX process at their grain boundaries due to the strain accumulation because of the stress partitioning and the elastic modulus mismatch [13]. Grain boundary pinning by the secondary particles such as Mg_5RE, Mg_3Gd (dynamically precipitated at the DRX grain boundaries and present in the as-cast phase), and LPSO phases reduces the grain growth leading to the refined grain size [13, 14]. Hence, the 15Li alloys showed greater refinement in the microstructure when compared to other alloys. The particles consist primarily of a block-like shape for the 23Li and 30Li alloys.

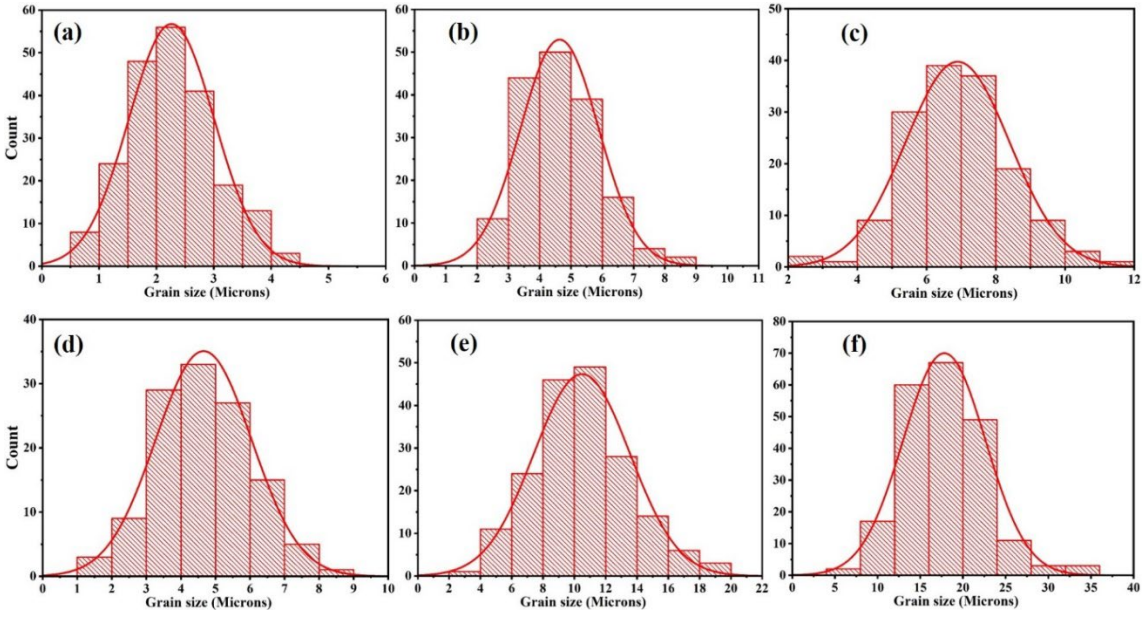

Figure 5.6. Grain size distributions of as-extruded Mg-0.5Ni-0.5Zn -2Gd-xLi alloys. (a) & (d) 15Li, (b) & (e) 23Li and (c) & (f) 30Li. Plots (a), (b), & (c) represent for the samples extruded at 200 ℃ and (d), (e), & (f) at 300 ℃.

5.3.3. Evaluation of Microstructural Phases through TEM:

To understand the microstructure in more detail, the 200 ℃ extruded samples were analyzed using Transmission Electron Microscopy, and they are shown in **Figures 5.7, 5.8,** and **5.9** for the 15Li, 23Li and 30Li alloys, respectively.

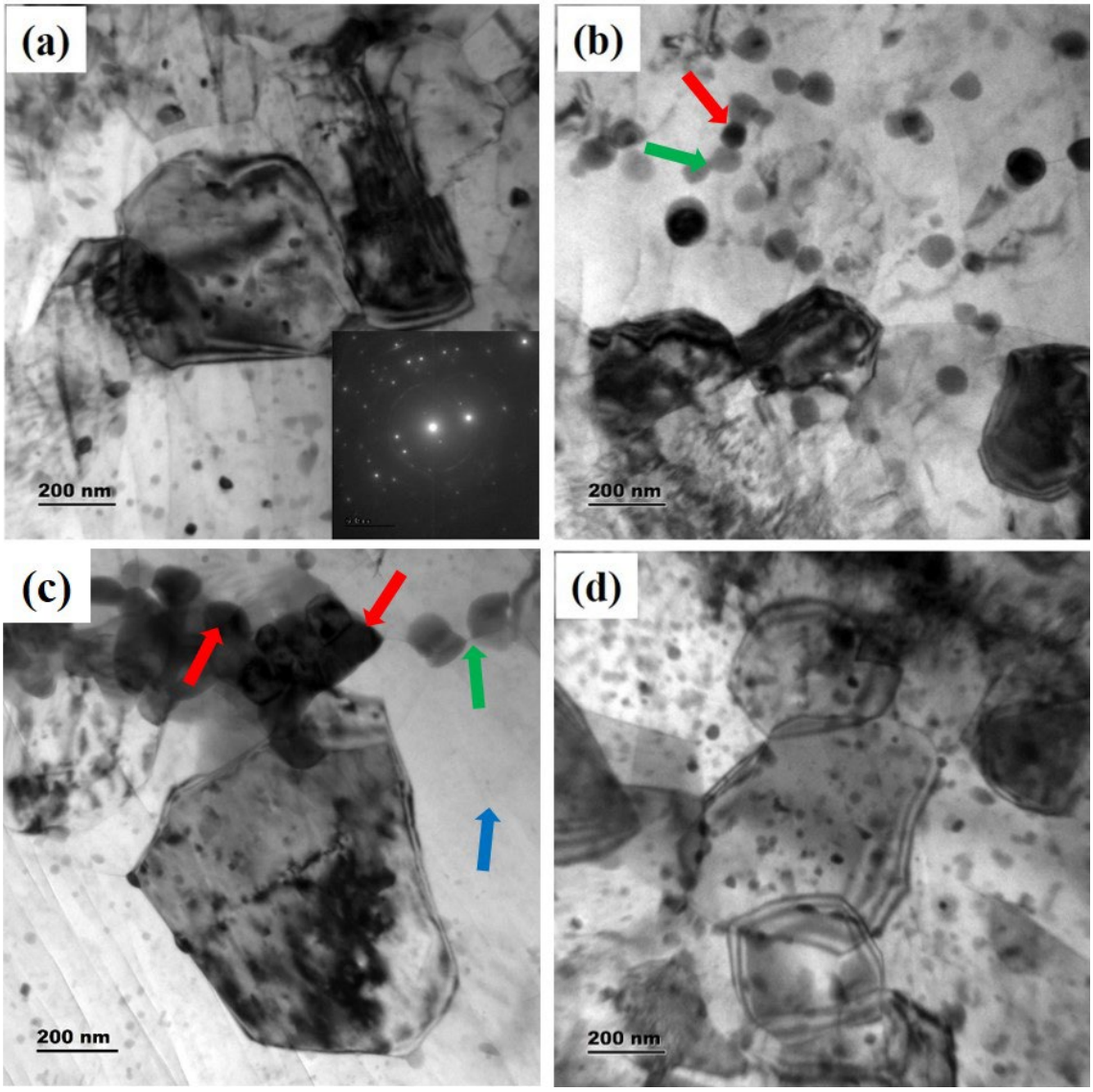

Figure 5.7. (a) to (d) Bright field images of Mg-0.5Ni-0.5Zn-2Gd-15Li alloy extruded at 200 ℃ at various locations showing the grain size, size; shape, and distribution of second phase particles.

15Li alloy micrographs (**Figure 5.7**) show that the matrix grain size was reduced to a sub-micron region at various locations at the extrusion at 200 ℃. Several small and big secondary phases were found in the matrix, whereas their type, size, shape, and distribution differed as a function of the location. The size of second phase particles varies from 10 nm to 200 nm depending on the location in the micrographs. Finer particles were mostly distributed inside the grains, whereas coarsest particles were located at the grain boundaries. Grain boundaries contain the greater free volume, and the diffusion of solute atoms takes place much faster; hence, the precipitates were larger than the matrix. The matrix grains having a finer distribution of secondary phases were found to be smaller in size, which might be due to the grain growth resistance offered by the particles due to the Zener pinning effect (**Figures 5.7a & 5.7b**). The grains are much coarser in some regions where these particles were absent (Blue arrow in **Figure 5.7c**). Two different contrasts can be observed in most precipitates, i.e., dark particles and light grey particles. The light grey particles (green arrows in **Figure 5.7b**) are usually found to be in contact with the darker particles (red arrows in **Figure 5.7b**). These darker particles were found to have high Gd content (**Figure 5.8**) and are mostly Mg_3Gd particles, whereas lighter particles could be the LPSO particles. The same phenomenon can also be observed for the particles present along grain boundaries as well (Red arrows in **Figure 5.7c**). Also, at some locations, the light grey particles grew from the grain boundaries and into the matrix grains (green arrow in **Figure 5.7c**). An identical phenomenon was noticed in the case of Mg-0.5Ni-2.5Gd-xLi alloys (section 4.3.3), where LPSO nucleation occurs either at the matrix grain boundaries or at the Mg_3Gd particles. Jiahao et al., also observed the generation of globular LPSO particles in the matrix in case of Mg-8Li-6Y-2Zn (wt.%) alloy by means of heat treatment and hot rolling processes [15]. Zn has good solid solubility in the Mg-matrix (6.2 wt.% or 2.4 at.% @ 340 ℃) [16]. The current alloys consist of 0.5 at. % Zn; hence almost all the Zn is expected to be soluble in the matrix, which is the reason for the nucleation of LPSO particles both within the matrix and along grain boundaries. Formation of the LPSO phase during the aging heat treatments at temperatures of 300 ℃ was observed in $Mg_{96.5}Zn_1Gd_{2.5}$ (at. %) alloy [17, 18]. Michiaki et al., [18] observed that after solution treatment (500 ℃ for 5 hrs) and subsequent aging at 300 ℃ of $Mg_{96.5}Zn_1Gd_{2.5}$ (at. %) alloy, the microstructure consists of the 14H - LPSO phase formed from supersaturated solid solution and Mg_3Gd particles at the grain boundaries. Especially the grain boundaries act as nucleating sites due to the initial enrichment

of Gd and Zn solutes due to their higher free volume. Hence, adding Zn in the current alloys benefitted the nucleation and uniform dispersion of LPSO phases within the matrix grains.

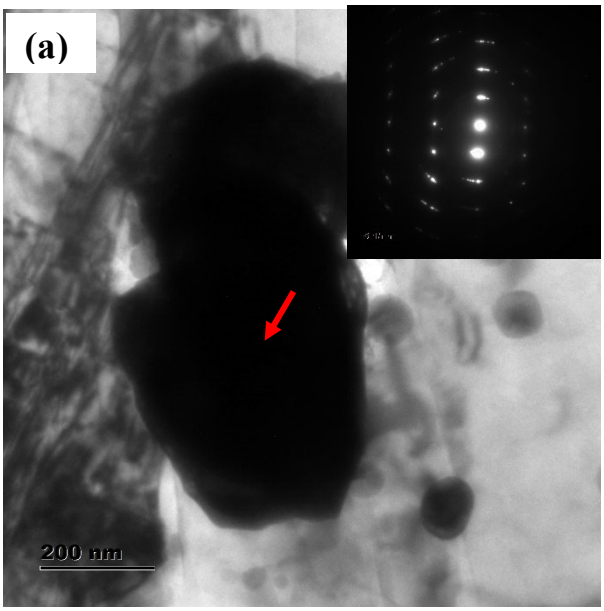

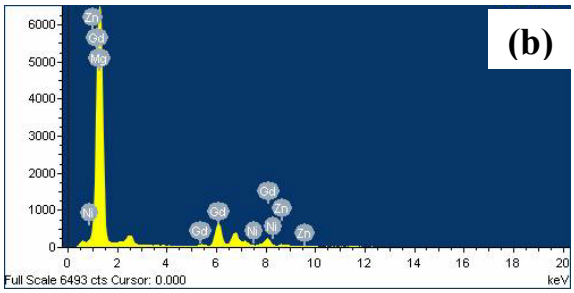

(c)

Element	Weight %	Atomic %
Mg K	52.21	86.84
Ni K	0.38	0.26
Zn K	1.94	1.2
Gd L	45.46	11.69

Figure 5.8. The presence of Mg_3Gd particles in the matrix and at the grain boundaries in the Mg-0.5Ni-0.5Zn-2Gd-15Li alloy extruded at 200 ℃. (a) Bright field image, (b) EDS analysis of the particle, and (c) corresponding chemical composition.

Figures 5.9 and **5.10** shows the TEM-BF micrographs of 23Li and 30Li samples extruded at 200 ℃. Similar features as observed in the 15Li alloy were observed. Fine grains (**Figures 5.9a & 5.10a**) and coarse grains greater than 1 µm (**Figure 5.9b**) were observed in the alloy. Larger grains were found to contain a minimum number of LPSO particles. Some of the LPSO particles started from the dark Mg_3Gd particles (red arrow in **Figure 5.9a**), from the grain boundaries (red arrow in **Figure 5.9c**) and Mg_3Gd particles present along grain boundaries (**Figure 5.10c**). The volume fraction of LPSO phase particles decreased greatly compared to 15Li alloy. Also, bigger Mg_3Gd particles were observed, and the dislocation structure was found to be greater surrounding these particles and show a sub-grain structure. The lesser quantity of LPSO particles can be attributed to the high content of Li in the matrix, which suppresses the formation of LPSO by decreasing the solid solubility of alloying elements like Zinc & Gd and increasing the stacking fault energy [19]. Yang et al., [20] and Si-jie et al., [21] observed that in the Mg-xLi-2Zn-2Gd (x= 8 and 9 wt.%) alloys, the as-cast microstructure consists of I-phase

(Mg_3Zn_6Gd) and W-phase ($Mg_3Zn_3Gd_2$). Initially, W-phase and $(Mg, Zn)_3Gd$ phases were found to be present for low Zn and Gd contents, and their volume fraction increases with an increase in the alloying elements. After a critical amount, Icosahedral I-phase was observed. Since the amount of Zn in the current alloys is low, these phases were not observed, but an increased amount of $(Mg, Zn)_3Gd$ and some amount of LPSO phases were found to be present.

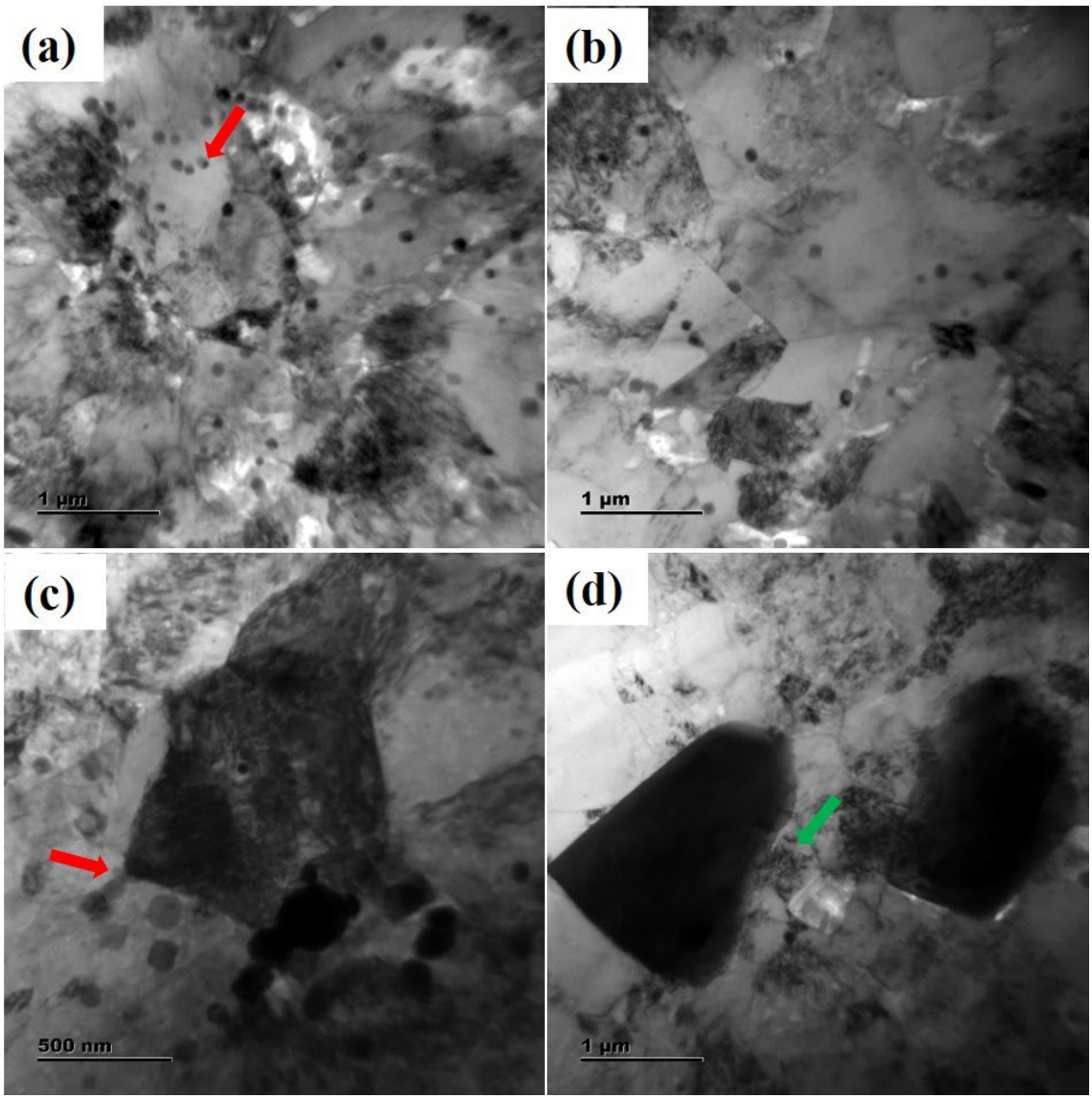

Figure 5.9. TEM - BF images of Mg-0.5Ni-0.5Zn-2Gd-23Li alloy extruded at 200 °C. (a) Fine grain structure having a good number of LPSO particles, (b) Coarse grains with fewer LPSO particles, (c) presence of LPSO particles at the grain boundaries, and (d) Dislocation accumulation at the Mg_3Gd particle boundaries.

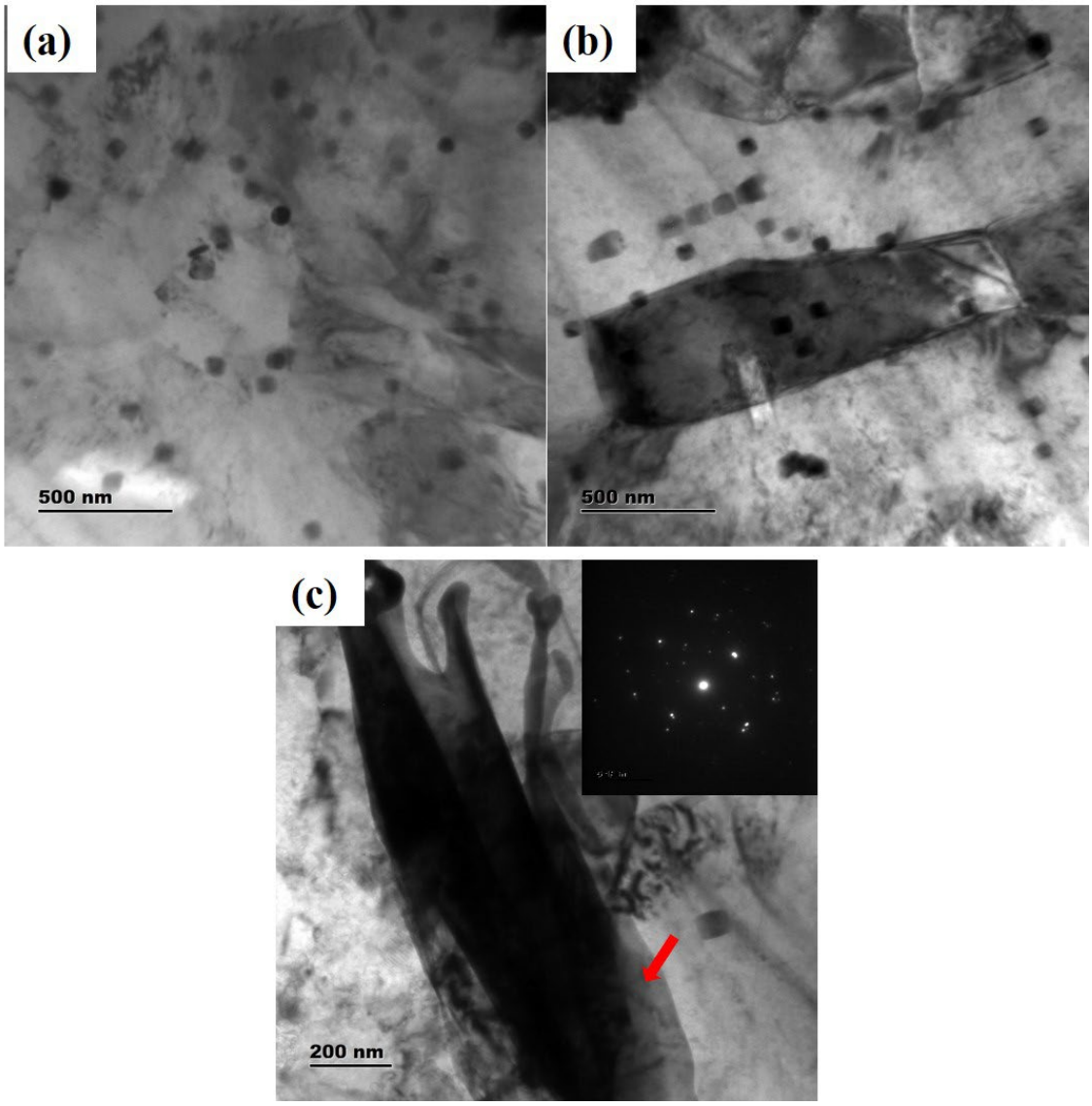

Figure 5.10. TEM - BF images of Mg-0.5Ni-0.5Zn -2Gd-30Li alloy extruded at 200 °C. (a) and (b) Presence of fine LPSO particles at different locations, and (c) Growth of LPSO particles at the Mg_3Gd particle boundaries.

5.4 Physical and Mechanical Properties:

5.4.1 Density:

Changes in the density of extruded alloys were measured and are depicted in **Figure 5.11b**. Even with the presence of relatively heavier elements like Zn, Ni and Gd, the density of the three alloys was calculated to be 1.78 g/cc, 1.69 g/cc and 1.59 g/cc for 15Li, 23Li and 30Li

alloys, respectively. The increased percentage of Li significantly reduced the alloy's density, which is ascribed due to lithium's low density (0.534 g/cc). In alloys 23Li and 30Li, the alloy density was lower than that of the pure magnesium (1.738 g/cc).

5.4.2 Hardness:

Figure 5.11a depicts the hardness of all the three alloys after extrusion at 200 ℃ and 300 ℃. The alloys extruded at 200 ℃ exhibited moderately better hardness than those extruded at 300 ℃. The hardness of the alloys gradually decreased with a boost in Li content. With further increment in the Li content, the hardness decreased drastically to a value as low as 51 HV, which can be ascribed to the high volume fraction of the soft β-Li phase in the alloy and reduction in the volume fraction of lamellar LPSO, confirmed by XRD as well as microstructural studies. The 15Li alloy extruded at 200 ℃ showed the highest hardness value of 95 HV.

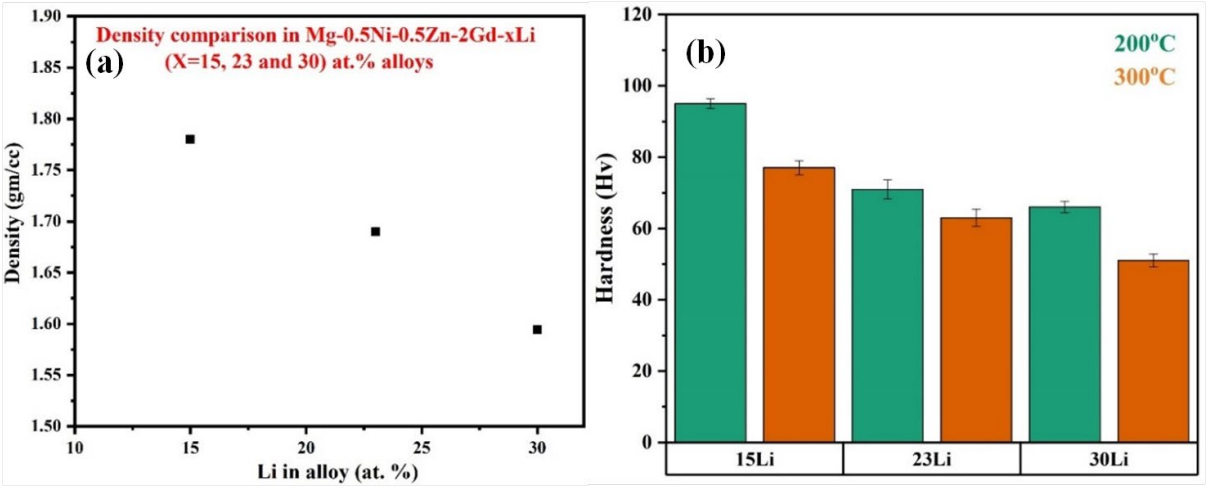

Figure 5.11. Variation of (a) density and (b) hardness with increasing Li content in the as-extruded Mg-0.5Ni-0.5Zn-2Gd-xLi alloys.

5.4.3 Tensile Testing at room temperature:

The tensile stress-strain curves of the alloys extruded at 200 ℃ and 300 ℃ tested at ambient temperature are presented in **Figure 5.12**, and the corresponding calculated mechanical properties are shown in Table 5.2. In both the extrusion temperature conditions, the tensile yield strength i.e., 0.2% yield stress, dropped and total elongation increased with increase in Li content in the alloys. The alloys extruded at 200 ℃ portrayed better strength than their counterparts extruded at 300 ℃. There is a significant improvement in elongation for the alloys extruded at

higher temperatures i.e., 300 ℃. 15Li alloy extruded at 200 ℃ possessed the highest tensile yield strength and UTS of 270 MPa and 320 MPa, respectively, with a good total elongation of 18%.

Compared to the similar alloy (i.e., Mg-0.5Ni-2.5Gd-15Li (at. %)) in the Chapter 4, there is a 35% improvement in the tensile yield stress i.e., i.e., 0.2% yield stress and 125% increase in the total elongation. Likewise, even 23Li alloy displayed better mechanical properties than the Mg-0.5Ni-2.5Gd-25Li alloy (Chapter 4), with a 23% and 46% rise in tensile yield strength and UTS values, respectively. Even though a decrease in elongation was observed for 23Li when compared to Mg-0.5Ni-2.5Gd-25Li alloy (Chapter 4), strain softening was completely eliminated. 30Li alloy also displayed a good strength of 201 MPa and 145 MPa at 200 ℃ and 300 ℃ respectively, however, after a critical amount of elongation (~10%), it also exhibited strain softening at both the extrusion temperatures. The extrusion temperature affected the alloys' mechanical properties significantly, as seen from the notable drop in strength. The secondary phases played a pivotal role in upholding the good mechanical properties and the fine grains were achieved through hot extrusion. Zn addition achieved the objective of imparting LPSO phases even in higher Li content alloys and successfully assisted in accomplishing better mechanical properties.

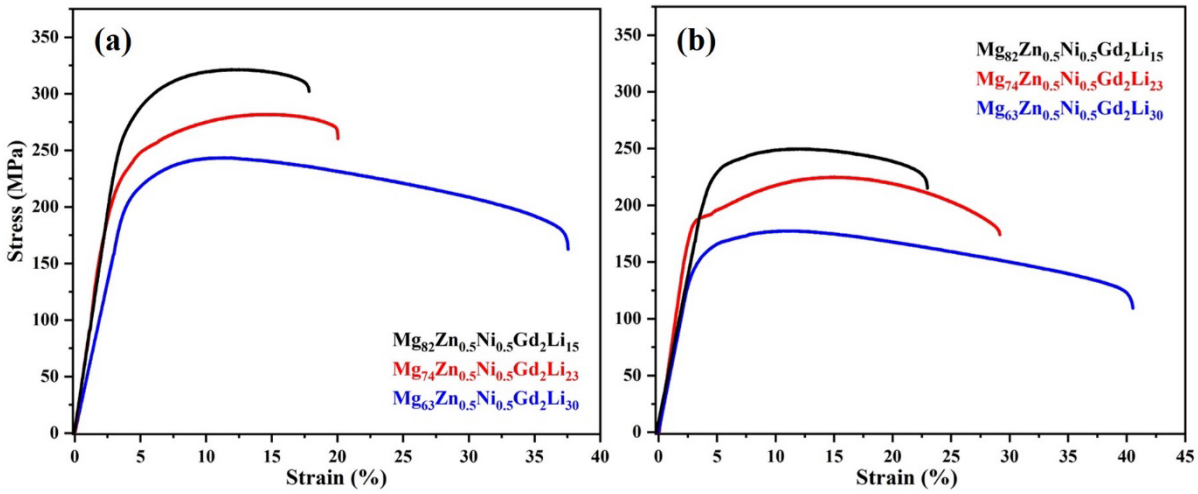

Figure 5.12. Typical room temperature tensile stress-strain curves of Mg-0.5Ni-0.5Zn-2Gd-xLi alloys extruded at (a) 200 ℃, and (b) 300 ℃ temperatures.

The mechanical property enhancements can be accredited to the synergy of secondary phases like LPSO and Mg_3Gd (precipitation and dispersion strengthening) and the fine dynamically recrystallized grains (Hall-Petch relationship). A significant increase in the total elongation and strain softening behavior in the 30Li alloy was mainly due to the increased presence of the β-Li phase. The work hardening phenomenon is strong in 15Li and 23Li compositions owing to the presence of a high-volume fraction of nano LPSO particles in the matrix but reduces in 30Li alloys irrespective of the extrusion temperature. The 15Li-200 ℃ alloy exhibits the highest yield strength, which proves that the fine precipitates in the grains impart a substantially higher strengthening effect. The strength of the 23Li-200 ℃ alloy is comparatively lesser than that of the 15Li-200 ℃ alloy. Despite the 23Li-200 ℃ alloy having relatively coarse grains, an adequate density of secondary phase precipitates can contribute to the precipitate strengthening.

The conventionally observed phenomenon is that, the accumulation of dislocations around obstacles accounts for the hardening behavior, whereas softening occurs when dislocations climb or slip over hinderances. 48 slip planes present the possibility to be activated in the case of the soft BCC β-Li matrix phase, thereby increasing the probability for undergoing deformation. Softening can also occur as a result of dynamic recovery post yield during tensile deformation. Dynamic recovery has been reported for the Mg-9Li-6Al and Mg-15Li-6Al alloys undergoing tensile tests at room temperature [22]. The excess Li addition accelerates the cross-slip and dislocation climb, resulting in annihilation of dislocations, thereby resulting in a softening phenomenon. In other wrought single phase β-Li or near β-Li Mg-Li alloys with greater than 9 wt. % Li [23-26], the softening behavior is evident even during room temperature tensile test. Hence, it is paramount that the annihilation of dislocations should be controlled by restricting their movement by the uniform dispersion of second-phase particles.

Table 5.2. Tensile properties of the as-extruded Mg-0.5Ni-0.5Zn-2Gd-xLi alloys having different amounts of Li content.

Temp. of Extrusion	Li content in the alloys (at. %)	Tensile Test		
		0.2% Yield (MPa)	Ultimate strength (MPa)	Total Elongation (%)
200°C	15Li	270±1	320±2	18.0±1.6
	23Li	205±1	275±1	20.3±0.2
	30Li	201±1	230±1	38.2±0.6
300°C	15Li	225±1	248±2	24.4±0.5
	23Li	180±1	220±2	30.5±0.7
	30Li	145±1	170±1	41.2±1

During the tensile tests, the substantial ductility of over 30% signifies that, the phenomenon of necking during these tests is extremely gradual and prolonged. This is possible when the grains undergo slip thereby decreasing the probability for stress concentration and increasing the ability to undergo more deformation. The stress concentration would most likely be centered around Gd-rich phases which have the capability to hinder mobility of dislocations, which can then accumulate and boost the material's strength. However, they might cause stress concentration at the matrix and Mg_3Gd interface. With an increase in the temperature of extrusion, the surface area covered by grain boundary decreases thereby facilitating nucleation of micro-cracks along the grain boundary as compared to the LPSO phases or at Mg_3Gd phases.

5.5 Summary:

The microstructure evolution and mechanical properties of cast and extruded Mg-0.5Ni-0.5Zn-2Gd-xLi (x = 15, 23, and 30 at. %) alloy system was studied using different techniques to evaluate the effect of Zn and Lithium on the formation of LPSO and other secondary phases like Mg_3Gd. In the as-cast state, the eutectic phase was a quasi-continuous network along the dendritic boundaries of α-Mg, Mg_3Gd, and LPSO phases. Initially, with an increase in Li content, the lamellar LPSO phase decreased continuously with an increase in the Li content leading to Mg_3Gd and eutectic phases in the as-cast condition. Solutionizing treatment

transformed the quasi-continuous network of 15Li and 23Li alloys into discontinuous structures having LPSO and Mg3Gd particles along with solid solutions of α-Mg and β-Li alloys. Whereas 30Li shows the quasi-continuous network even after the solutionisation treatment with reduced eutectic volume fraction and increased blocky LPSO phases. The hot extrusion process leads to grain size refinement due to dynamic recrystallization and the crushing, breaking, and uniform dispersion of second-phase particles (Mg_3Gd and LPSO phases). A high yield strength of 270 MPa with a tensile elongation of 18% and good strain hardening behavior was achieved in 15Li alloy extruded at a temperature of 200 ℃, which can be ascribed to the fine grain size (sub-micron grains), and uniform distribution of the Mg_3Gd phase and LPSO phases. 30Li alloy showed a good tensile ductility of 41%, albeit with low yield strength values due to the presence of β-Li, a soft bcc phase.

References:

[1] W.J. Ding, et al. “Formation of 14H-type long period stacking ordered structure in the as-cast and solid solution treated Mg-Gd-Zn-Zr alloys”, J. Mater. Res., Vol. 24, No. 5, 2009, pp. 1842 – 1854.

[2] Liu, Wei, et al. "Precipitation behaviors of 14H LPSO lamellae in Mg 96 Gd 3 Zn 0.5 Ni 0.5 alloys during severe plastic deformation." *Journal of Materials Science* 52 (2017): 13271-13283.

[3] Atsushi Yamamoto, et al. “Precipitation in Mg-(4-13)%Li-(4-5)%Zn ternary alloys”, Materials Transactions, Vol. 44, No. 4, 2003, pp. 619 – 624.

[4] Zhang, Jinshan, et al. "Study of Mg–Gd–Zn–Zr alloys with long period stacking ordered structures." *Materials Science and Engineering: A* 585 (2013): 268-276.

[5] Wu, Y. J., et al. "Formation of a lamellar 14H-type long period stacking ordered structure in an as-cast Mg–Gd–Zn–Zr alloy." *Journal of materials science* 44 (2009): 1607-1612.

[6] Du, Yaxian, et al. "Formation of lamellar phase with 18R-type LPSO structure in an as-cast Mg96Gd3Zn1 (at. %) alloy." *Materials Letters* 169 (2016): 168-171.

[7] J. Yin et al. “Investigation of Two-Phase Mg-Gd-Ni Alloys with Highly Stable Long Period Stacking Ordered Phases.” *Intermetallics*, 68(2016): 63–70.

[8] A.A. Nayeb-Hashemi et al. “The Li-Mg (Lithium-Magnesium) System”, *Bull. Alloy Phase Diagrams* 5(1984): 365–374.

[9] S. Feng, et al. “Effect of Extrusion Ratio on Microstructure and Mechanical Properties of Mg–8Li–3Al–2Zn–0.5Y Alloy with Duplex Structure.” *Materials Science and Engineering: A* 692 (2017): 9-16.

[10] Y. Yang et al. “Influence of Extrusion on the Microstructure and Mechanical Behavior of Mg-9Li-3Al-XSr Alloys.”, *Metall. Mater. Trans. A*, 44(2013): 1101–1113.

[11] W. Liu et al. “High-Performance Extruded Mg89Y4Zn2Li5 Alloy with Deformed LPSO Structures plus Fine Dynamical Recrystallized Grains.” *Materials and Design*, 110(2016): 1–9.

[12] Wu, S. Z. et al. "Ultrahigh strength Mg-Y-Ni alloys obtained by regulating second phases." *Journal of Materials Science & Technology* 45 (2020): 117-124.

[13] Xu, Chao, et al. "Effect of LPSO and SFs on microstructure evolution and mechanical properties of Mg-Gd-Y-Zn-Zr alloy." *Scientific reports* 7.1 (2017): 40846.

[14] Yu, Zijian, et al. "Microstructure evolution and mechanical properties of as-extruded Mg-Gd-Y-Zr alloy with Zn and Nd additions." *Materials Science and Engineering: A* 713 (2018): 234-243.

[15] Wang, Jiahao, et al. "Improvement of electromagnetic shielding properties for Mg-8Li-6Y-2Zn alloy by heat treatment and hot rolling." *Journal of Materials Science: Materials in Electronics* 31 (2020): 17249-17257.

[16] Binjiang, Lu, et al. "Effects of Extruding Temperature on Microstructure and Mechanical Properties of Mg-2.0 Zn-0.3 Zr-0.9 Y Alloy." *Rare Metal Materials and Engineering* 42.4 (2013): 841-844.

[17] Ding, W. J., et al. "Formation of 14H-type long period stacking ordered structure in the as-cast and solid solution treated Mg-Gd-Zn-Zr alloys." *Journal of Materials Research* 24 (2009): 1842-1854.

[18] Yamasaki, Michiaki, et al. "Mechanical properties of warm-extruded Mg–Zn–Gd alloy with coherent 14H long periodic stacking ordered structure precipitate." *Scripta Materialia* 53.7 (2005): 799-803.

[19] Han, J., et al. "Basal-plane stacking-fault energies of Mg: A first-principles study of Li- and Al-alloying effects." *Scripta Materialia* 64.8 (2011): 693-696.

[20] Zhang, Yang, et al. "Microstructure and tensile properties of as-extruded Mg–Li–Zn–Gd alloys reinforced with icosahedral quasicrystal phase." *Materials & Design (1980-2015)* 66 (2015): 162-168.

[21] Ouyang, Si-jie, et al. "Microstructure and mechanical properties of as-cast Mg− 8Li− xZn− yGd (x= 1, 2, 3, 4; y= 1, 2) alloys." *Transactions of Nonferrous Metals Society of China* 29.6 (2019): 1211-1222.

[22] Zou, Yun, et al. "Improvement of mechanical behaviors of a superlight Mg-Li base alloy by duplex phases and fine precipitates." *Journal of Alloys and Compounds* 735 (2018): 2625-2633.

[23] Lei, Xue, et al. "Effect of Hot Extrusion on the Microstructure, Mechanical Properties, and Corrosion Behavior of Mg–11Li–3Al–2Zn–1.5 Nd–0.2 Zr Alloy." *Transactions of the Indian Institute of Metals* 72 (2019): 2893-2899.

[24] Tang, Yan, et al. "Microstructure evolution and strengthening mechanism study of Mg-Li alloys during deformation and heat treatment." *Materials Science and Engineering: A* 704 (2017): 344-359.

[25] Li, Chuanqiang, et al. "Effects of icosahedral phase on mechanical anisotropy of as-extruded Mg-14Li (in wt%) based alloys." *Journal of Materials Science & Technology* 35.11 (2019): 2477-2484.

[26] Dutkiewicz, Jan, et al. "Development of new age hardenable Mg-Li-Sc alloys." *Journal of Alloys and Compounds* 784 (2019): 686-696.

6

Development of high-strength $Mg_{98.82}Ni_{0.59}Gd_{0.59}$ and $Mg_{97.56}Ni_{1.22}Gd_{1.22}$ (at. %) alloys through Powder Metallurgy

As-cast and extruded Mg-0.5Ni-2.5Gd-xLi and Mg-0.5Ni-0.5Zn-2Gd-xLi alloys show a significant increase in strength and ductility compared to pure magnesium (Chapters 4 and 5). The strength can be further improved by refining the microstructure, e.g., decreasing the grain size to the nanoscale. The dynamic recrystallization, which is the primary driving factor for grain refinement for these alloys, happens due to the high-temperature processing; making it difficult for the further refinement of the microstructure. The powder metallurgy route has been considered one of the best processing routes to decrease the grain size of magnesium alloys to the nanoscale; thereby, a significant gain in the strength levels has been reported [1-4]. The additional advantage of the powder metallurgy route is that the amount of alloying addition needed is far less to achieve high strength as compared to the other processing routes [1,5].

In the present investigation, the alloys $Mg_{94.96}Ni_{1.37}Gd_{3.67}$ and $Mg_{90}Ni_{2.72}Gd_{7.28}$ (wt.%) ($Mg_{98.82}Ni_{0.59}Gd_{0.59}$ and $Mg_{97.56}Ni_{1.22}Gd_{1.22}$ (at. %)) were processed by mechanical alloying, hot compaction and subsequent hot extrusion. The main objective was to understand the

microstructure evolution and its relationship with the mechanical properties of the P/M Mg–Ni–Gd alloys by compressive tests at room temperature.

The alloys with the pre-determined composition were prepared through the powder metallurgy route of mechanical alloying using a planetary ball mill (RETSCH PM 400). High-purity magnesium powder (-325 mesh, Alfa Aesar) and equiatomic NiGd master alloy pieces (prepared using a Vacuum Arc Re-melting process) were used. The powder mixture was loaded into a high chrome steel vial. High chrome steel balls were used with a ball-to-powder weight ratio of 20:1 at a speed of 300 rpm, while 0.5 ml ethanol was used as a process control agent (PCA). The milling process was carried out for 150 hrs in an argon atmosphere. Small quantities of the milled powders were collected at regular intervals and characterized with X-Ray Diffraction (XRD, Panalytical, Xpert Powder) to study the crystallite size, lattice strain, solubility of alloying elements, and evolution of phases with milling time. The complete handling of the powders was conducted in a glove box under an argon (99.999%) atmosphere to eliminate contamination with atmospheric air. After 150 hrs of mechanical alloying, the precise quantity of powder was subjected to hot compaction in a vacuum, followed by hot extrusion to reduce porosity. The hot compaction was done at 550 °C at three different holding durations of 5 hrs, 7 hrs, and 9 hrs, and a load of 50 MPa was applied at the final 2 minutes of the process. The compact obtained was further subjected to hot extrusion at 500 °C with a reduction ratio of 16:1.

6.1 Density:

The density of the as-extruded samples was measured using the Archimedes principle (ASTM B 962-15) by taking the weight of the samples in air and ethanol. The densities of both alloys at three different compaction holding times were calculated and presented in Table 6.1. The measured densities of the alloys were close to the density of pure Mg. Only a slight increase was observed with alloying as the quantity of alloying elements was minimal. The theoretical density was calculated using the rule of mixtures. There is an evident improvement in relative density with the increase in the compaction holding time.

Table. 6.1. Densities of the alloys measured through Archimedes principle.

Alloy (at. %)	Compaction (hrs)	Density (gm/cc)	Relative density (%)	Theoretical (gm/cc)
$Mg_{98.82}Ni_{0.59}Gd_{0.59}$	5	1.6917	93.5	1.809
	7	1.7421	96.3	
	9	1.7743	98.1	
$Mg_{97.56}Ni_{1.22}Gd_{1.22}$	5	1.7504	92.8	1.8864
	7	1.8032	95.6	
	9	1.8511	98.5	

6.2 Phase analysis using XRD:

6.2.1 Analysis of Powders:

Figure 6.1 shows the evolution of phases during mechanical alloying at various time intervals (0.5, 1.5, 3, 6, 10, 30, 50, 75, 100 and 150 hours) in both the alloys. Two significant changes can be observed as the milling time increases: firstly, the magnesium peaks' width is increased, height is decreased and had a little peak shift. Secondly, the NiGd phase peaks get broadened and only one peak is visible at an angle of 42°, whereas the other peaks disappear in the background noise. These changes were consistent in both alloys. These two observations indicate that the crystallite size of both phases keeps decreasing, and the slight peak shift in magnesium might be due to the solid solution formation and strain-induced due to the mechanical milling process.

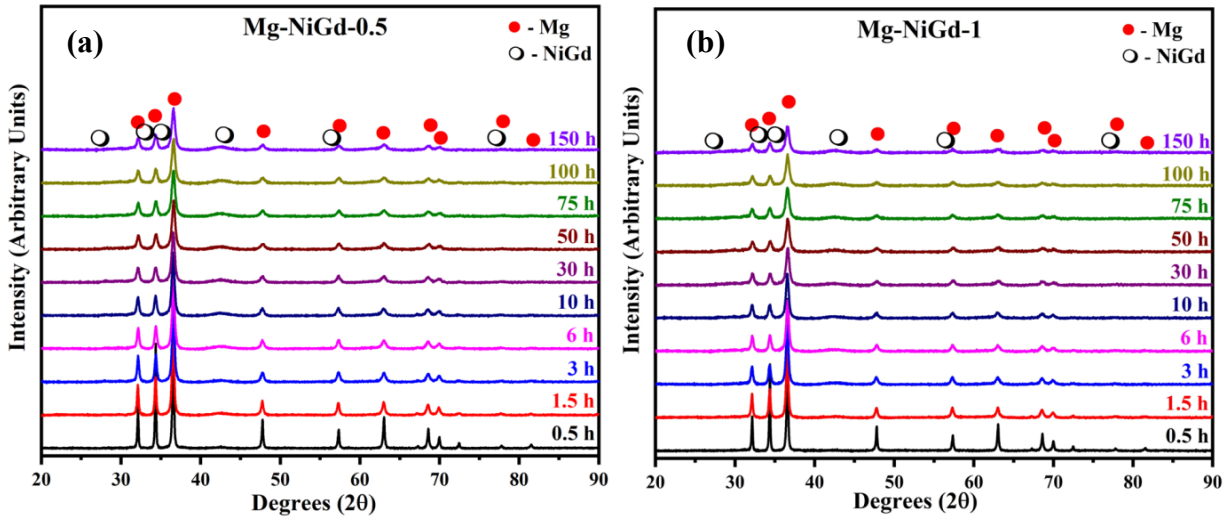

Figure 6.1. The study of phases in the milling powder at different intervals of milling time. (a) $Mg_{98.82}Ni_{0.59}Gd_{0.59}$ (at. %) and (b) $Mg_{97.56}Ni_{1.22}Gd_{1.22}$ (at. %).

Figure 6.2 shows the variation in lattice strain and crystallite size with respect to the milling time obtained using the Williamson-Hall method [6]. In both alloys, the crystallite size decreased rapidly during the initial milling period and later achieved a gradual reduction till the end of 150 hours of milling. Similarly, the lattice strain initially increased, and the increase in the later stages of milling is smaller. The crystallite sizes of the $Mg_{98.82}Ni_{0.59}Gd_{0.59}$, $Mg_{97.56}Ni_{1.22}Gd_{1.22}$ (at. %) alloys are 91 nm and 47 nm, respectively. The alloy with higher content of Ni and Gd exhibited finer crystallite size which could be due to the incorporation of brittle intermetallic particles (NiGd) embedded in the magnesium matrix, inducing strain in the surrounding matrix and further crack and decrease overall crystallite size. Lattice parameters a and c were calculated and they are 0.322 & 0.521 nm before milling and 0.318 & 0.530 nm after 150 hrs milling, indicating that some amount of solid solution has taken place. Nickel being a smaller atomic radius and Gd having a bigger atomic radius when compared to Mg results in changes in the lattice parameter as they dissolve into the matrix, which is similar to the trends observed in the Mg-Zn-Y system [7].

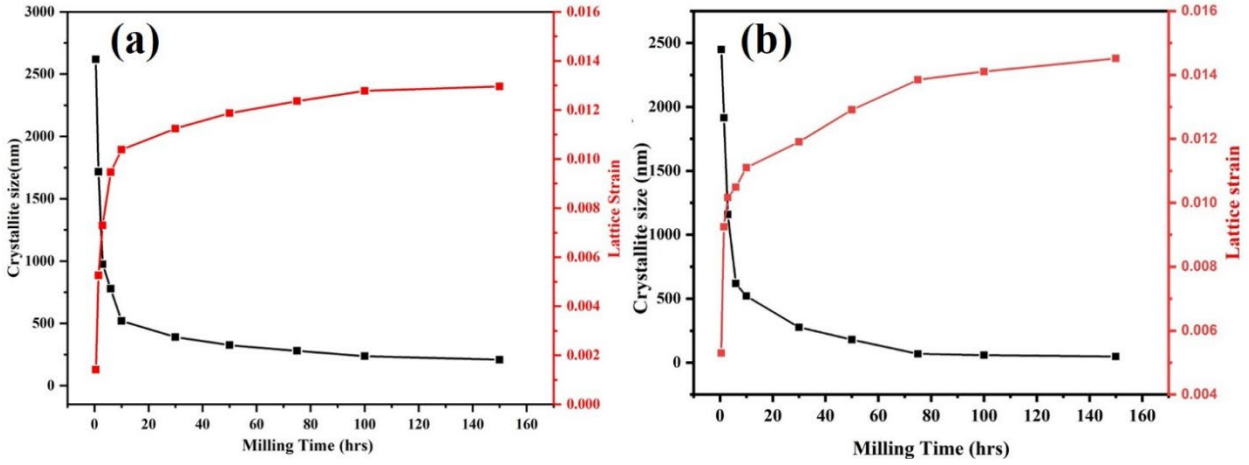

Figure 6.2. Variation of Crystallite size and lattice strain during milling.
(a) $Mg_{98.82}Ni_{0.59}Gd_{0.59}$ (at. %) and (b) $Mg_{97.56}Ni_{1.22}Gd_{1.22}$ (at. %).

The observed reduction in crystallite size or mechanisms of grain refinement during mechanical alloying has been evaluated in detail by Fecht et al. [8]. It begins with localized deformation by creating shear bands with high dislocation density, followed by annihilation and subsequent dislocation recombination, thereby forming nanometre-sized grains during the process. The subgrain boundary is transformed into high-angle grain boundaries with random orientations.

6.2.2 Phase analysis of the samples after extrusion:

Numerous phases, i.e., Mg_5Gd, Mg_2Ni, Gd_2O_3 and MgO, were observed after the extrusion process and are shown in **Figure 6.3**. The formation of Mg_5Gd and Mg_2Ni is due to the reaction between the Mg-matrix and NiGd. Interestingly, no LPSO phase peaks were observed, which are very prominent in the cast alloys, as observed in Chapter 3 in the base alloy and also similar observation was found by Liu et al. [9]. The formation of a stable equilibrium intermetallic phase, when compared to the metastable LPSO, was also reported in the Mg-Zn-Y alloys by mechanical milling/alloying and subsequent consolidation by equal channel angular pressing [8,10,11]. In the case of Y-containing alloys, $Mg_{24}Y_5$ [8,10,11], whereas Gd-containing alloys Mg_3Gd or Mg_5Gd were observed after the consolidation process either by extrusion or ECAP processes [5]. An increase in the holding time during the hot compaction decreased the NiGd phase and increased the volume fractions of the intermetallic phases. The

presence/formation of oxide phases was also observed after the sintering of mechanically milled or alloyed Mg-powders [2,12]. Several factors influence oxygen contamination, i.e., the condition of initial raw materials, milling media, process control agent, milling atmosphere, and consolidation parameters [8]. The presence of Gd_2O_3 and MgO might be due to the oxygen picked up either from the reaction between the Mg and ethanol or due to the very thin oxide layer on the master alloy or oxygen pickup during the transfer of the powder from the glove box to the sintering furnace.

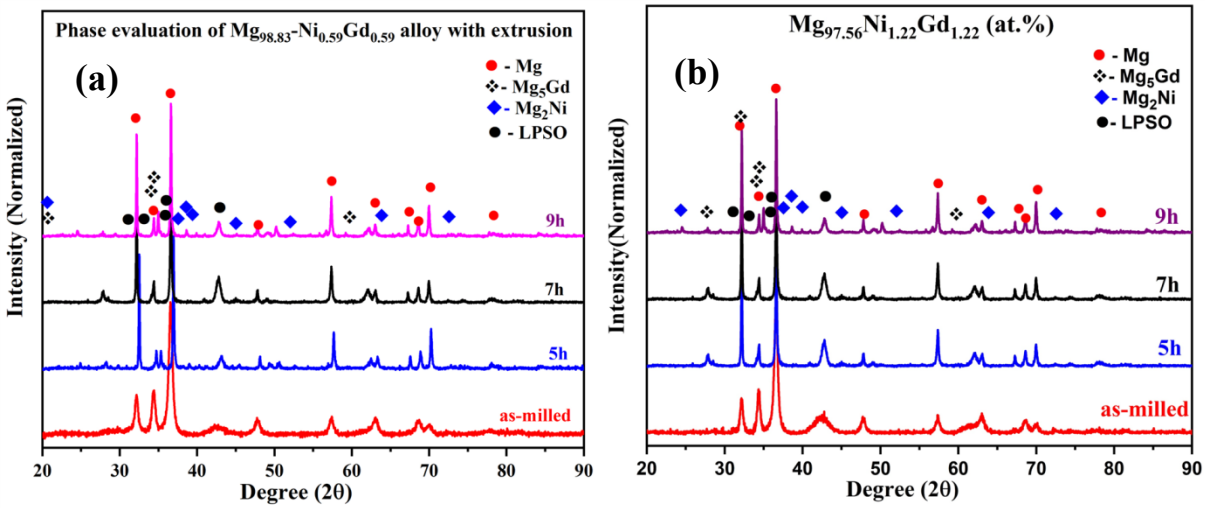

Figure 6.3. X-ray diffraction patterns of mechanically alloyed powders and extruded specimens after different processing conditions (a) $Mg_{98.82}Ni_{0.59}Gd_{0.59}$ (at. %) and (b) $Mg_{97.56}Ni_{1.22}Gd_{1.22}$ (at. %) .

6.3 Microstructural Characterization:

6.3.1 Scanning Electron Microscopy:

The powder particle morphology after 150hrs of milling is shown in **Figures 6.4a** and **6.4b**. The fracturing and welding of powder particles can be seen, and the average size of the particles is around 10 µm and 7.5 µm for alloys $Mg_{98.82}Ni_{0.59}Gd_{0.59}$ (at. %) and (b) $Mg_{97.56}Ni_{1.22}Gd_{1.22}$ (at. %), respectively (**Figures 6.4c** and **6.4d**). The white particles, as shown by red arrows in Figures 6.4a and 6.4b, show the undissolved agglomerated sub-micron size NiGd particles which are uniformly dispersed in the powder particles, supporting the XRD observations (**Figure 6.1**). A notable decrease in particle size was observed with an increase in alloying addition. This refinement can be attributed to the proliferated amounts of brittle

intermetallic phase that promote the brittle fracture of overall particles due to the uniform dispersion inside and at the boundaries of the agglomerated particles.

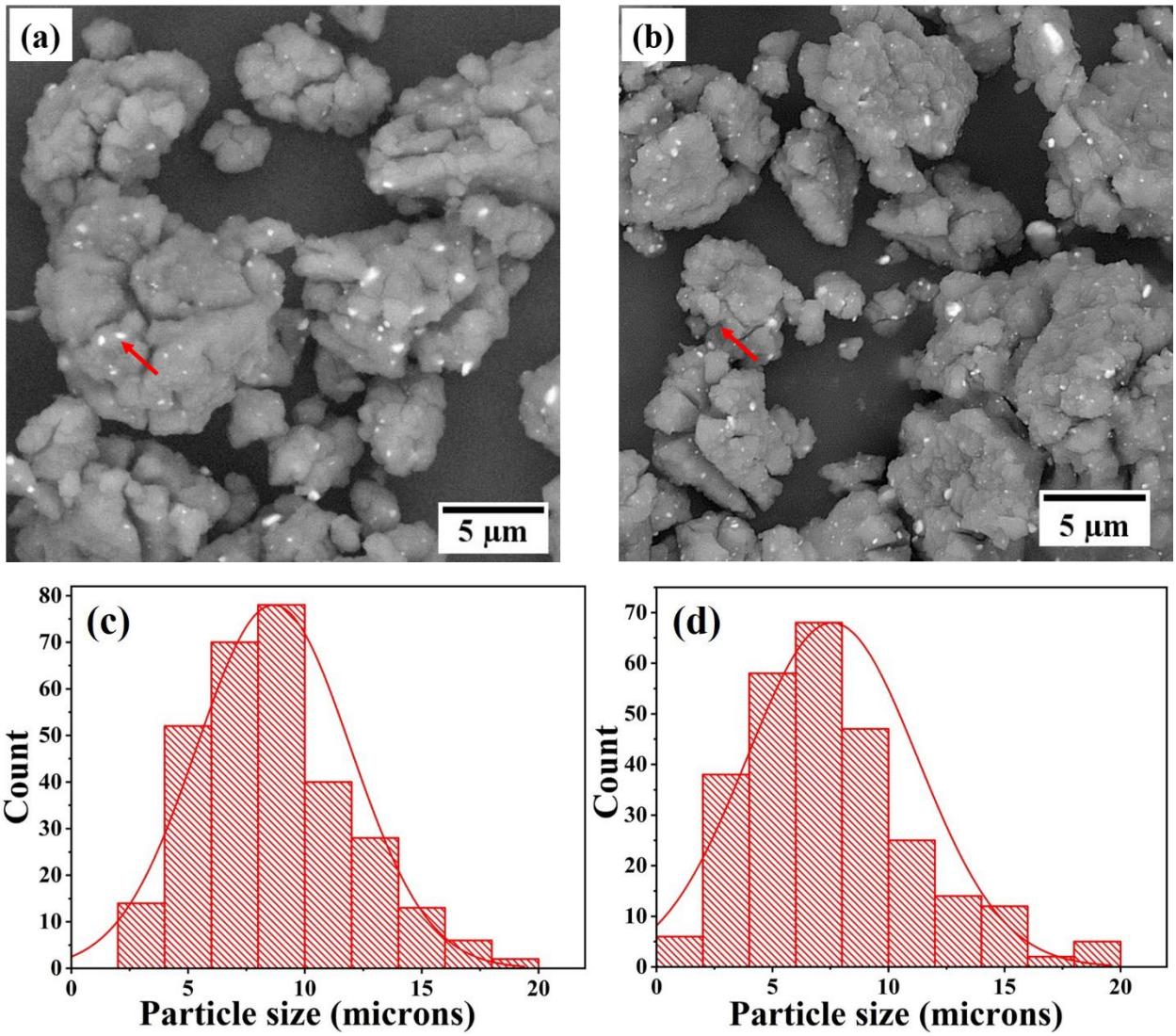

Figure 6.4. SEM-BSE images of powders and corresponding particle size distribution after 150 hrs of milling (a) & (c) $Mg_{98.82}Ni_{0.59}Gd_{0.59}$ (at. %) and (b) & (d) $Mg_{97.56}Ni_{1.22}Gd_{1.22}$ (at. %).

Figure 6.5 shows the SEM-BSE micrograph of the as-extruded sample after hot compaction. **Figures 6.5a** and **6.5c** represent samples with 7hrs of holding time and **Figures 6.5b** and **6.5d** with holding time of 9 hrs. Uniform dispersion of second-phase particles with sizes ranging from nano to sub-micron scale was observed in both conditions. A cluster of second-phase particles was also observed (Blue arrow in Figure 6.5c). The undissolved NiGd particle reacted with the Mg-matrix and formed this cluster of second phases.

Even though some porosity was observed at 7hrs of holding condition (shown with a green arrow in **Figure 6.5a**), the increase in the hot compaction time to 9 hrs and subsequent extrusion reduced this porosity to a greater extent (**Figure 6.5b**). Some of the second phase particle morphology was changed from round to plate/needle shape (indicated with a yellow arrow in **Figure 6.5d**). The distribution of elements was observed using SEM-EDS mapping in the 7hrs hot compacted and extruded sample and is shown in **Figure 6.6**. The white particles are rich in Gd (**Figure 6.6d**), whereas Ni (**Figure 6.6c**) is distributed uniformly. Hence, different sizes of Mg_5Gd particles and nanometer-scale Mg_2Ni particles were present in this sample. The EDS plot of the total area is close to the alloy composition considered in this study (**Figure 6.6f**). The slight deviation is due to the particle density present in the current magnification and lower magnification area analysis gave better composition. With an increase in the compaction time, needle-shaped particles were observed (**Figure 6.5d**).

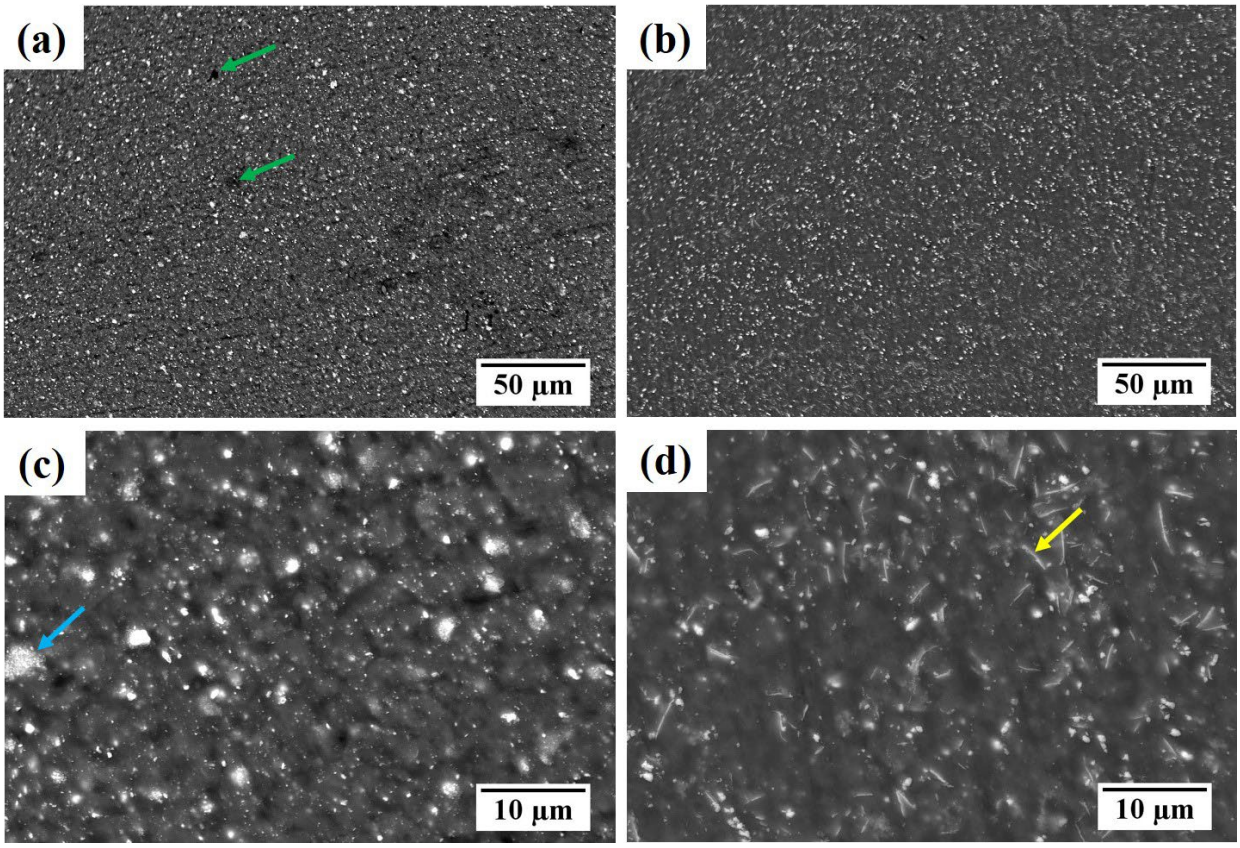

Figure 6.5. SEM-BSE micrographs of as-extruded $Mg_{97.56}Ni_{1.22}Gd_{1.22}$ (at. %) alloy at two different compaction times (a) & (c) 7 hrs and (b) & (d) 9 hrs

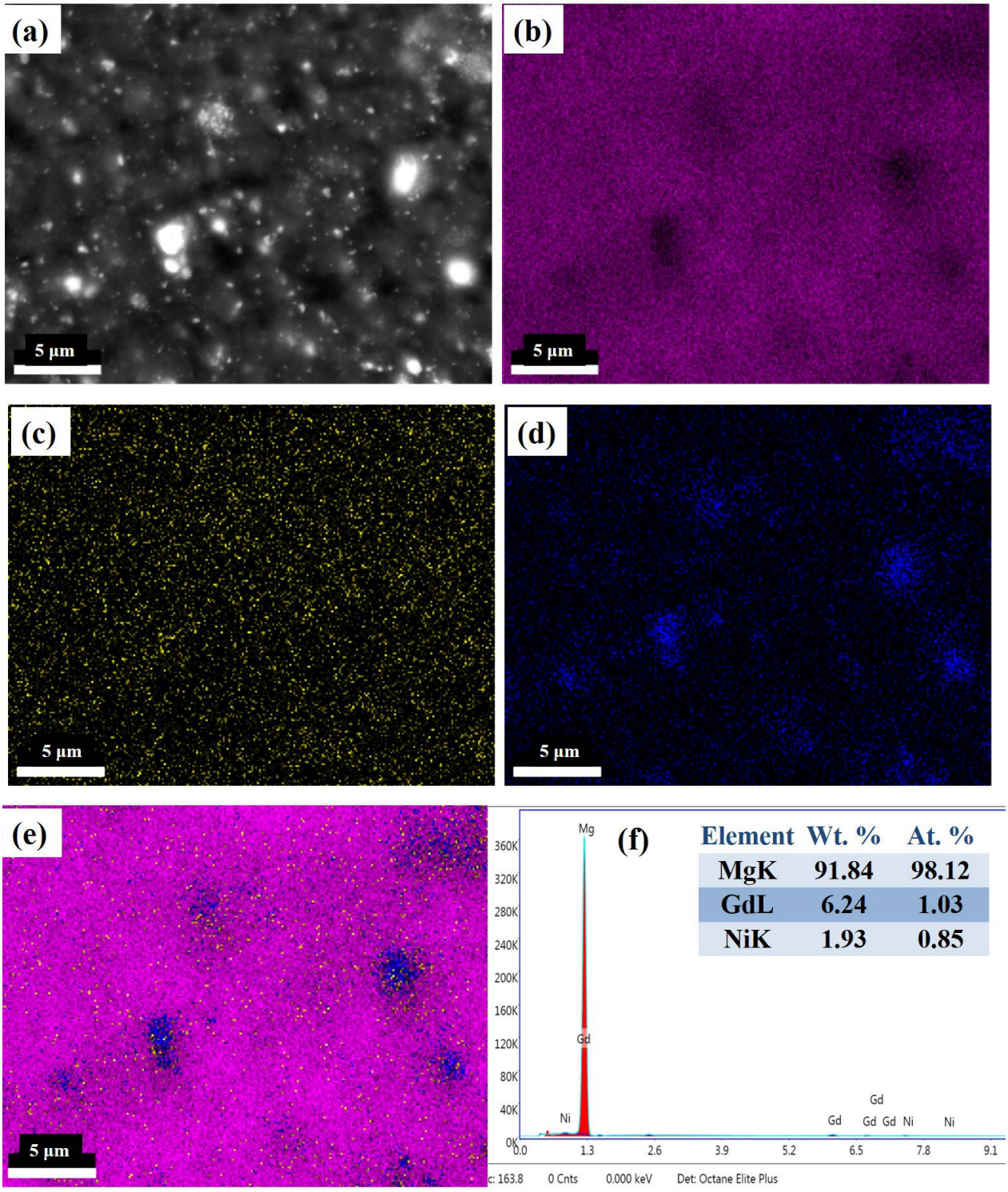

Figure 6.6. SEM-EDS elemental mapping of $Mg_{97.56}Ni_{1.22}Gd_{1.22}$ (at. %) alloy: hot compaction (7h) and extruded (a) SEM-BSE image, (b) Mg, (c) Ni, (d) Gd and (e) area EDS spectrum.

6.3.2 Transmission Electron Microscopy:

Figures 6.7 and **6.8** shows the uniform dispersion of minute second-phase particles within the magnesium matrix of $Mg_{97.56}Ni_{1.22}Gd_{1.22}$ (at. %) alloy after various processing conditions. Mostly, nano-scale grains were observed at lower processing times (**Figures 6.7a** and **6.7d**) and with increasing time, grain growth took place (**Figures 6.7c and 6.7f**). At the maximum processing time, the alloys exhibited a bimodal microstructure comprising of fine dynamically recrystallized grains with arbitrary orientations and coarse hot-worked grains along the extrusion direction. Most of the grains are in the sub-micron range, still occasionally, grains having 1 μm size (**Figure 6.8**) can be observed, indicating that the second phase particles are very effective in pinning the grain boundaries and restricting the grain growth.

The second phase particles were observed both at grain boundaries and within the bigger grains (**Figures 6.7f & 6.8b**). Three types of particles were observed: cuboid particles (5 to 20 nm), needle-shaped particles, and bigger cuboid particles. **Figure 6.8c** shows the BF image, micro-diffraction ([011] zone axis), and EDS analysis of nano cuboid particles. The particle has an FCC structure with an average lattice parameter of 0.43 nm and contains some Gd in it. Hence, it can be concluded that the particles are MgO with some Gd in them, consistent with the XRD observation (**Figure 6.3**). More analysis needs to be done in order to observe the Gd_2O_3 particles whose peaks are present in the XRD plot. One edge of the needle-shaped particles was found to be very close or starting at the edge of the cuboid particles (**Figure 6.8d**), indicating that the cuboid particles act as a preferential nucleating site for other particles.

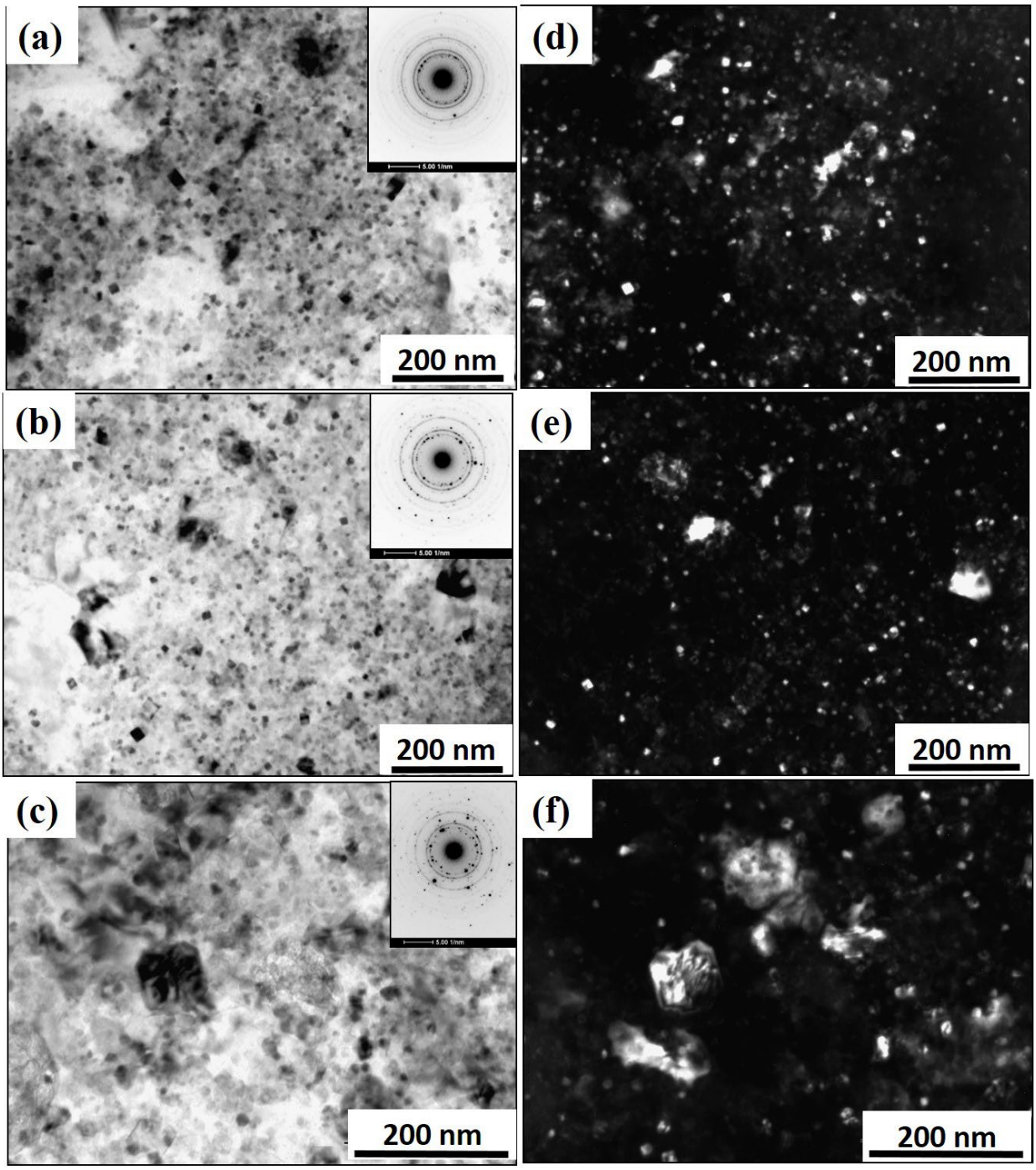

Figure 6.7. TEM–bright and dark field images of $Mg_{97.56}Ni_{1.22}Gd_{1.22}$ (at. %) alloy samples hot compacted for different holding times (a) 5, (b) 7, and (c) 9 hrs.

The formation of MgO and its effect on the matrix grain growth has been studied by several authors [10,12-14]. Since Mg is highly reactive with oxygen, especially when the grain

size is at nanometer size and any presence of oxygen traces during the milling or subsequent consolidation leads to MgO formation [8]. Hence, it is unavoidable during the powder metallurgy processing route. MgO was found to effectively pin the grain boundaries and increase the activation energy barrier, thereby reducing its growth, e.g., Wang et al. [13] studied the hot-pressed AZ31 alloy after mechanical milling of the powder in a hydrogen atmosphere. Even after exposing the alloy to 400 ℃ for 600 min, the matrix grains have only grown from 65 nm to 165 nm.

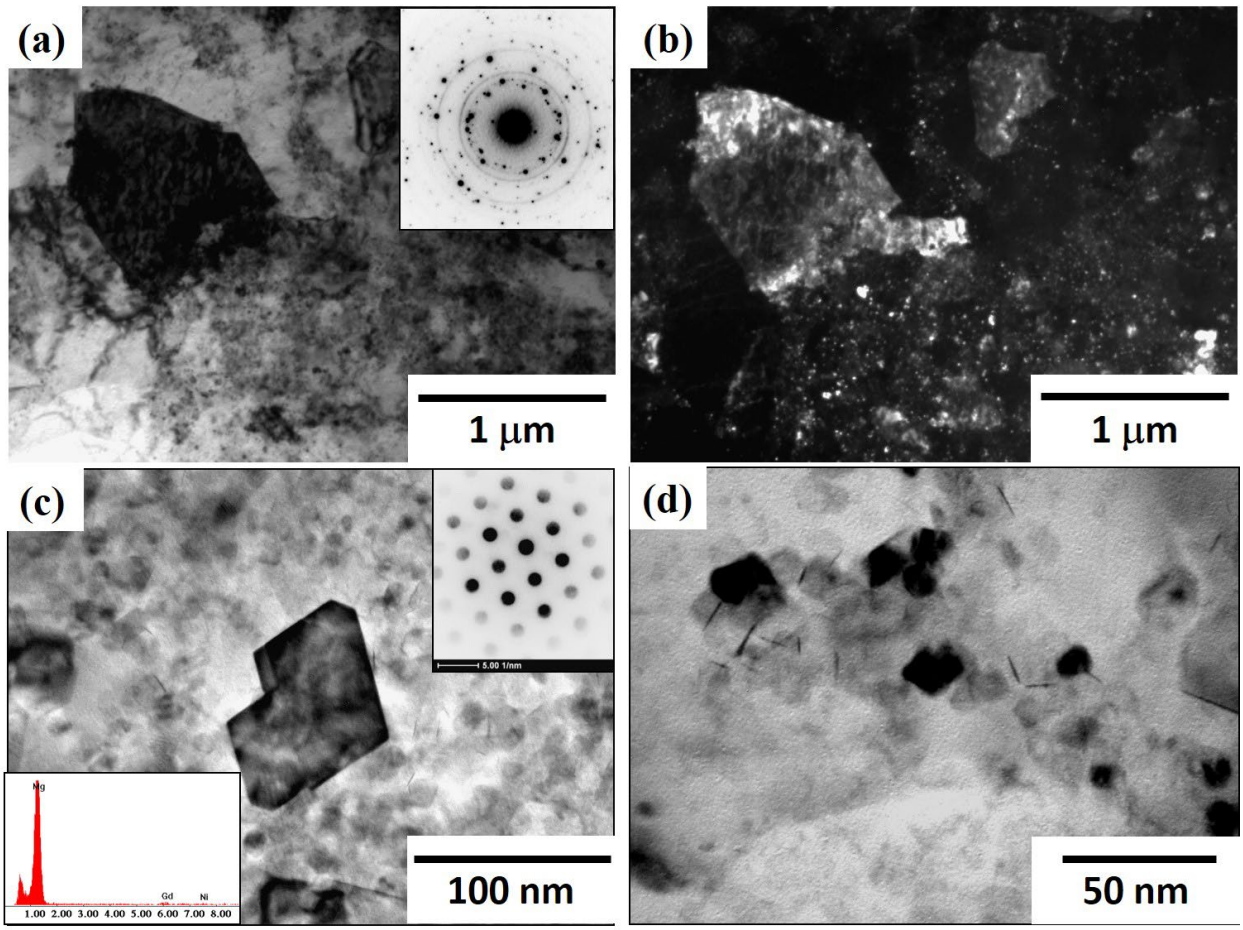

Figure 6.8. TEM images of 9 h hot compacted and subsequently extruded sample: (a) bright-field image, (b) dark-field image of the corresponding region, (c) high magnification image showing the MgO particles, and (d) needle-shaped particle formation at the edges and faces of cuboid particles.

The presence of other nano-oxides or nano intermetallic phases along with MgO was found to increase the grain growth resistance even further [10,12]. The RE elements and transition metals have low diffusivity in the Mg, their growth rates are very small and they can also act as effective grain growth pinning agents [15]. Hence, the current results concur with the reported data that the presence and uniform distribution of MgO, Gd_2O_3, Mg_5Gd and Mg_2Ni lead to an increased grain growth resistance.

6.4 Compression testing of extruded alloys:

Compressive stress-strain plots of differently processed alloys tested at room temperature are depicted in **Figure 6.9** and the corresponding mechanical properties are tabulated in Table 6.2. The strength of most of the alloys was observed to be far more stellar than the cast and extruded magnesium alloys (Chapters 4 and 5) [16-18]. Good amount of elongation (%) is also observed in the current alloys and is a significant result for magnesium alloys prepared through the powder processing route via mechanical alloying. The highest strength was exhibited by the alloy $Mg_{97.56}Ni_{1.22}Gd_{1.22}$ with a holding time of 5h, i.e., 804 MPa, and 877 MPa of yield strength and ultimate strength respectively with a total elongation of 3.75%. $Mg_{97.56}Ni_{1.22}Gd_{1.22}$ alloys portrayed better strength values in comparison with $Mg_{98.82}Ni_{0.59}Gd_{0.59}$ alloys at the corresponding compaction holding times.

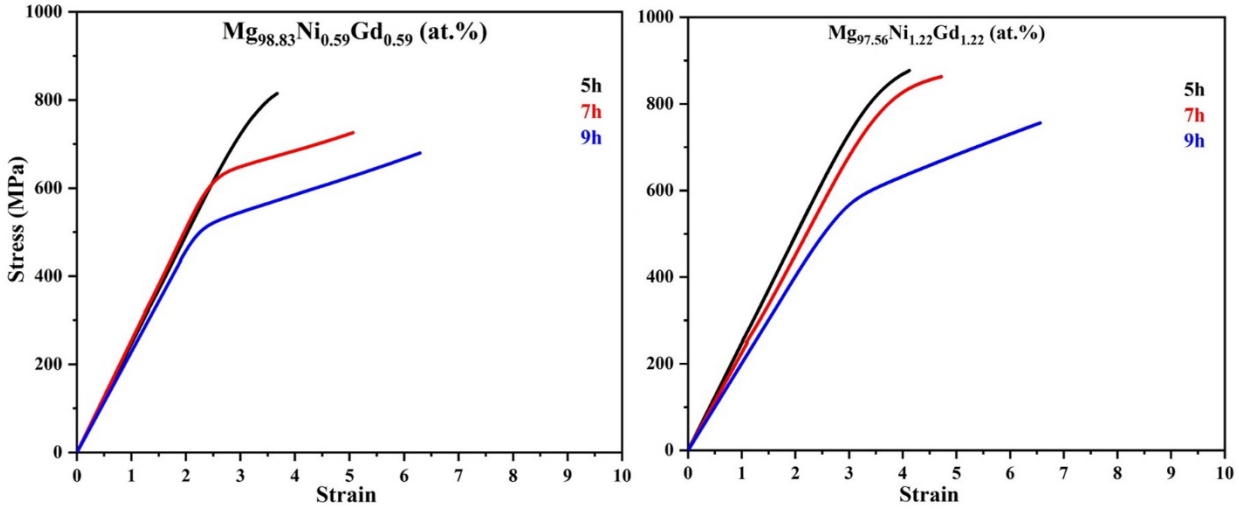

Figure 6.9. Compression stress-strain curves of extruded alloys at room temperature (a) $Mg_{98.82}Ni_{0.59}Gd_{0.59}$ (at. %) and (b) $Mg_{97.56}Ni_{1.22}Gd_{1.22}$ (at. %).

Table. 6.2. Mechanical properties of alloys after extrusion evaluated through Compression Testing at room temperature.

Alloy	Compaction (hrs.)	0.2% Yield strength (MPa)	Ultimate tensile strength (MPa)	Total elongation (%)
$Mg_{98.82}Ni_{0.59}Gd_{0.59}$	5	765±3	815±3	3.6±0.2
	7	629±3	726±3	5.1±0.1
	9	508±2	680±3	6.5±0.4
$Mg_{97.56}Ni_{1.22}Gd_{1.22}$	5	804±4	877±2	3.8±0.1
	7	730±2	862±2	4.6±0.3
	9	575±1	756±1	6.7±0.3

The 5 hrs compacted samples displayed the best mechanical properties in both the alloys. $Mg_{98.82}Ni_{0.59}Gd_{0.59}$ alloy 5 hrs sample with 765 MPa as yield strength and 815 MPa as strength before failure, performed inferior to 5 hrs sample of $Mg_{97.56}Ni_{1.22}Gd_{1.22}$ alloy. The reduction in the yield stress was comparatively high in the $Mg_{98.82}Ni_{0.59}Gd_{0.59}$ samples than that of $Mg_{97.56}Ni_{1.22}Gd_{1.22}$ alloys with increasing holding time. In $Mg_{98.82}Ni_{0.59}Gd_{0.59}$, 7 hrs had 21.6% and 9 hrs had 50.6% reduction with respect to 5 hrs alloy, while in $Mg_{97.56}Ni_{1.22}Gd_{1.22}$, 7 hrs had 10.1% and 9 hrs had 39.8% decrease compared to 5 hrs alloy. This can be attributed to the increased alloying content giving rise to a relatively high volume of secondary phases in the $Mg_{97.56}Ni_{1.22}Gd_{1.22}$ alloys than that of $Mg_{98.82}Ni_{0.59}Gd_{0.59}$ alloys.

A high yield strength of 804 MPa with small elongation was observed for the alloy with a short processing time, which might be due to the presence of nanocrystalline Mg-grains (50 nm), uniformly dispersed nano secondary intermetallic phases (10 to 20 nm) and nano-oxide particles. With increasing the processing time, the growth of several grains was observed. Due to the Zener pinning effect by the nano-intermetallic particles and oxide particles at the grain boundaries, the growth was sluggish, and only a small volume fraction of ultra-fine grains (100 nm) was observed. This has led to a decrease in the yield strength of the material to 730 MPa but increased the elongation of the material slightly. A slight strain hardening behavior could be observed due to the presence of nano-secondary particles inside the ultra-fine matrix grains (**Figure 6.7**).

The yield strength was further dropped to 575 MPa with the highest processing times, where a bimodal grain size distribution was observed (**Figure 6.8**), i.e., large grains having nearly 1μm, ultrafine grains (250-500 nm) and uniform dispersion of various sized particles. Even though the yield strength decreased, the elongation increased significantly and exhibited a better strain-hardening behavior. The strength of the material depends upon various microstructural features such as grain size & size, shape and distribution of second-phase particles, and the distribution of other defects [3,14,19-21]. The highest strength values were found when the grain size was decreased to the nano-crystalline regime [19] and uniform dispersion of nano second-phase particles in the matrix and at the grain boundaries [22,23]. Since most of the operations involve high temperatures, emphasis has been made on incorporating these secondary phases, which are stable and resistant to coarsening at the processing temperatures [5,8,24,25]. The secondary phases containing transition elements &/or rare earth elements and oxide particles were found to be better suited for this purpose [5,8,24-27].

Zhang et al. [12] observed a yield strength of 382 MPa with 15% elongation for the ZK60 alloy fabricated through powder metallurgy and extrusion, having a grain size of 0.45 μm with fine dispersion of nano-MgO particles and $MgZn_2$ phases. The enhanced strength was explained in terms of resistance to dislocation motion by creating more boundaries (ultra-fine grain size), Orowan strengthening due to the dispersion of MgO particles in the matrix and coefficient of thermal mismatch between nano-magnesia and matrix, due to which dislocations density increased. Matsuda et al. produced $Mg_{97}Zn_1Y_2$ (at. %) alloy using mechanical alloying and extrusion process and found a high compressive yield strength of 616 MPa with 4.2% plastic strain values. The average grain size of 200 nm and uniform dense dispersion of MgO and Y_2O_3 particles was attributed to the highest strength levels [10]. It was noted that LPSO phase formation was not observed during this process, whereas the same composition shows a pronounced metastable LPSO phase in the casting process [1]. Recently, an ultra-strong $Mg_{85}Zn_6Y_9$ (at. %) alloy having 865 MPa as the strength was prepared by high-energy ball milling for a short duration, subsequent consolidation by spark plasma sintering (400 ℃) and extrusion (500 ℃) processes [2]. The microstructure of this alloy was found to contain a heterogeneous mixture of ultra-fine grain LPSO-containing matrix, micron-scale LPSO phase and uniformly dispersed coherent Y-O-Si nanoparticles. It was postulated that all the strengthening mechanisms, i.e., Hall-Petch strengthening due to UFG, dispersion strengthening

due to micron-scale LPSO phase, and Orowan strengthening due to the nano dispersoids were responsible for the resultant strength [2]. The effect of nano-dispersed MgO in the Mg matrix was studied by Cai et al. by varying the MgO contents [14]. High compressive yield strength of 688 MPa was achieved only after adding 20 vol% MgO and performing the consolidation at a high pressure of 6 GPa and 500 °C. In all the studies, it was observed that the grain growth was sluggish, so a high temperature had to be applied to achieve a good density material. The reason behind sluggish grain growth was found to be due to the presence of MgO particles at the grain boundaries, thereby pinning the grain boundaries.

Bimodal grain size distribution was found to give the best results, albeit with lower strength and good elongation, e.g., Xu et al. fabricated Ultra-Strong and Ductile Mg-Gd-Y-Zn-Zr alloy with bimodal microstructure with 466 MPa tensile yield strength and 14% elongation developed via hot extrusion and artificial aging [28]. High ductility was ascribed to the presence of dynamically recrystallized grains and an increment in the number density of dislocations due to the interactions between the dislocations and precipitates on basal and prismatic planes. Hence, in concurrence with the earlier observations, the reasons for the high compressive yield strength of the current alloys were due to the refinement of grain size to nano and ultra-fine grain size regime, uniform dispersion of secondary phases (Mg_5Gd, Mg_2Ni) and thermally stable and homogenously distributed oxide particles. At the same time, reasonable total elongation and good strain hardening were due to the bimodal grain size distribution and obstruction of dislocations by the fine dispersed (cuboidal MgO, Mg_5Gd, and Mg_2Ni) particles in them.

The total elongation improved with the increase of holding time in both alloys. This can be ascribed to the enhanced grain growth that occurred at prolonged exposure to the holding temperature. As given in the table, the elongation values were very much identical in both alloys for the corresponding compaction holding times. A slightly better total elongation was observed in NiGd0.5 ($Mg_{98.82}Ni_{0.59}Gd_{0.59}$ (at. %)) alloys may be due to the less secondary phases that act as barriers for the dislocation movement.

6.5 Summary:

A novel Mg–Ni–Gd alloy with a high strength was developed through a powder metallurgy process and the following main conclusions can be drawn:

A fine crystallite size of 47 nm is achieved after 150 hrs of milling, along with solid solution formation indicated by the shift in the magnesium peaks and change in lattice parameter values. Hot compaction and extrusion processes led to the formation of second-phase particles like Mg_5Gd, Mg_2Ni, Gd_2O_3, and MgO, which are more stable and resistant to coarsening at processing temperatures. Even after prolonged exposure to high sintering and extrusion temperatures, the grain sizes were still ultra-fine, attributed to the grain boundary pinning by secondary particles, especially MgO particles. Maximum compressive yield strength of 804 MPa was achieved for the 5 hrs hot-compacted sample due to the nano grain size and uniform dispersion of secondary phases. The strength dropped to 730 and 575 MPa for 7 and 9 h of compaction exposure respectively and the total elongation increased due to the formation of bimodal grain structure and dispersion of second phase particles inside the matrix. Second-phase particles and thermally stable oxide particles at the grain boundaries helped effectively pin the grain boundaries and restrict grain growth. The dispersoids were uniformly distributed and acted as barriers for dislocation movement leading to Orowan strengthening.

References:

[1] Kawamura, Yoshihito, et al. "Rapidly solidified powder metallurgy Mg97Zn1Y2Alloys with excellent tensile yield strength above 600 MPa." *Materials Transactions* 42.7 (2001): 1172-1176.

[2] Ding, Shuaijun, et al. "Achieving ultra-strong Mg alloys via a novel hierarchical long-period stacking ordered architecture." *Journal of Alloys and Compounds* 870 (2021): 159343.

[3] Mora, E., et al. "High-strength Mg–Zn–Y alloys produced by powder metallurgy." *Scripta Materialia* 60.9 (2009): 776-779.

[4] Lee, Taekyung, et al. "High-strength AZ91 alloy fabricated by rapidly solidified flaky powder metallurgy and hot extrusion." *Metals and Materials International* 25 (2019): 372-380.

[5] Cabeza, Sandra, et al. "Microstructure and Mechanical Behavior of Powder Metallurgy Mg 98.5 Gd 1 Zn 0.5 Alloy." *Metallurgical and Materials Transactions A* 45 (2014): 3222-3231.

[6] Zak, A. Khorsand, et al. "X-ray analysis of ZnO nanoparticles by Williamson–Hall and

size–strain plot methods." *Solid State Sciences* 13.1 (2011): 251-256.

[7] Ou, Keng-Liang, Chia-Chun Chen, and Chun Chiu. "Production of oxide dispersion strengthened Mg-Zn-Y alloy by equal channel angular pressing of mechanically alloyed powder." *Metals* 10.5 (2020): 679.

[8] Fecht, H-J. "Nanostructure formation by mechanical attrition." *Nanostructured Materials* 6.1-4 (1995): 33-42.

[9] Liu, Wei, et al. "Precipitation behaviors of 14H LPSO lamellae in Mg 96 Gd 3 Zn 0.5 Ni 0.5 alloys during severe plastic deformation." *Journal of Materials Science* 52 (2017): 13271-13283.

[10] Matsuda, Mitsuhiro, Yoshihito Kawamura, and Minoru Nishida. "Production of high strength Mg97Zn1Y2 alloy by using mechanically alloyed MgH2 powder." *Materials transactions* 44.4 (2003): 440-444.

[11] Chiu, Chun, and Hong-Min Huang. "Microstructure and properties of Mg-Zn-Y alloy powder compacted by equal channel angular pressing." *Materials* 11.9 (2018): 1678.

[12] Zhang, Zhenya, et al. "Microstructure and tensile properties of ZK60 alloy fabricated by simplified rapid solidification powder metallurgy (S-RS P/M) process." *Journal of Materials Science & Technology* 26.2 (2010): 151-155.

[13] Wang, Xin, et al. "Grain growth kinetics of bulk AZ31 magnesium alloy by hot pressing." *Journal of Alloys and Compounds* 527 (2012): 193-196.

[14] Cai, Xuecheng, et al. "Thermally stable and strong bulk Mg–MgO in situ nanocomposites by reactive cryomilling and high-pressure consolidation." *Journal of materials science* 53 (2018): 6613-6625.

[15] Zhou, Bi-Cheng, et al. "Diffusion coefficients of alloying elements in dilute Mg alloys: A comprehensive first-principles study." *Acta Materialia* 103 (2016): 573-586.

[16] Yamada, Kentaro, et al. "Alloy development of high toughness Mg-Gd-Y-Zn-Zr alloys." *Materials transactions* 47.4 (2006): 1066-1070.

[17] Homma, T., N. Kunito, and Scr Kamado. "Fabrication of extraordinary high-strength magnesium alloy by hot extrusion." *Scripta Materialia* 61.6 (2009): 644-647.

[18] Huang, Hua, et al. "Fabrication of ultra-high strength magnesium alloys over 540 MPa with low alloying concentration by double continuously extrusion." *Journal of magnesium and alloys* 6.2 (2018): 107-113.

[19] Yu, Huihui, et al. "Hall-Petch relationship in Mg alloys: A review." *Journal of Materials Science & Technology* 34.2 (2018): 248-256.

[20] Zhang, Zhi, et al. "Toward the development of Mg alloys with simultaneously improved strength and ductility by refining grain size via the deformation process." *International Journal of Minerals, Metallurgy and Materials* 28 (2021): 30-45.

[21] Guo, Huijun, et al. "The preparation and mechanical properties of nano-magnesium alloy bulks." *Journal of Alloys and Compounds* 819 (2020): 153253.

[22] Trojanová, Z., et al. "Strengthening in Mg–Li matrix composites." *Composites Science and Technology* 67.9 (2007): 1965-1973.

[23] Tahreen, N., et al. "Strengthening mechanisms in magnesium alloys containing ternary I, W and LPSO phases." *Journal of materials science & technology* 34.7 (2018): 1110-1118.

[24] Wang, Shihao, et al. "The nature of native MgO in Mg and its alloys." *Metallurgical and Materials Transactions A* 51 (2020): 2957-2974.

[25] González, Sergio, et al. "Influence of processing route on microstructure and mechanical properties of two Mg–Ni–Y–RE alloys." *Materials characterization* 64 (2012): 53-61.

[26] Kubásek, Jiří, et al. "Superior properties of Mg–4Y–3RE–Zr alloy prepared by powder metallurgy." *Journal of materials science & technology* 33.7 (2017): 652-660.

[27] Garcés, Gerardo, et al. "Development of long-period ordered structures during crystallisation of amorphous Mg80Cu10Y10 and Mg83Ni9Y8." *International journal of materials research* 97.4 (2022): 404-408.

[28] Xu, C., et al. "Deformation behavior of ultra-strong and ductile Mg-Gd-Y-Zn-Zr alloy with bimodal microstructure." *Metallurgical and Materials Transactions A* 49 (2018): 1931-1947.

7

Conclusions

The present study involves processing and characterization of Mg-Ni-Gd, Mg-Ni-Gd-Li, and Mg-Ni-Zn-Gd-Li alloys to understand the density, evolution of microstructure and its effect on mechanical performance. Initially, the casting route was used to optimize the microstructure with fine grain size and uniform dispersion of LPSO and Mg_3Gd phases. Subsequently, the powder metallurgy route was explored in order to create a bi-modal grain structure (nano + coarse grains) and uniform dispersion of second-phase particles. Detailed characterization was carried using SEM and TEM to understand the type, size, shape, and distribution of various microstructural features and their effect on the mechanical properties. The outcomes have been listed as follows:

1. Initially, the effect of Li content on the LPSO phase formation was explored in the Mg-0.5Ni-2.5Gd-xLi (x = 0, 1, 5, 10, 15, and 25 at. %) alloy system. The alloys were successfully cast using a vacuum induction melting furnace. In as-cast state, the eutectic phase existed in all the alloys as a quasi-continuous network along the dendritic boundaries

of α-Mg, Mg_3Gd, and LPSO phases. In addition, 15 and 25 at. % Li alloys contain β-Li phase as well whose volume fraction experienced a raise with increasing Li. The volume fraction of the LPSO was found to vary with an increase in the Li content, i.e., initially, it increases up to 5 at. % Li and subsequently, its volume fraction dropped when compared to the quasi-continuous eutectic phase. Extrusion at 400^{o}C led to grain size refinement due to dynamic recrystallization, completely eliminated the eutectic network, and resulted in the formation of lamellar LPSO/ blocky LPSO and Mg_3Gd particles. Up to 5 at. % Li, the LPSO and Mg_3Gd particles were uniformly dispersed in the microstructure and at high Li contents, most of the secondary phases (blocky LPSO, Mg_3Gd) were present along the grain boundaries of α-Mg and β-Li boundaries. High yield strength of 302 MPa, ultimate strength of 347 MPa, and 5% elongation was achieved in the 5 at. % Li alloy. The major contributors for the enhanced strength levels are grain size strengthening due to the fine grain size (around 2 microns), and precipitation strengthening as a result of the uniform distribution of the Mg_3Gd phase and LPSO phases. Whereas, a yield stress of 167 MPa, ultimate strength of 188 MPa and a tensile ductility of 37.5% was attained in 25Li alloy. The high elongations were found to be because of the presence of soft β-Li bcc phase.

2. Since, high Li content alloys possess low density but lack good strength values due to improper distribution of LPSO phases, a small amount of Zn (0.5 at. %) was added in place of Gd to the high Li containing alloys. Hence, the microstructure evolution and mechanical properties of cast and extruded Mg-0.5Ni-0.5Zn-2Gd-xLi (x = 15, 23, and 30 at. %) alloy system were studied using different techniques to evaluate the effect of Zn and Lithium on the formation of LPSO and other secondary phases like Mg_3Gd. Similar to the Mg-0.5Ni-2.5Gd-xLi alloys, in the as-cast state, a eutectic phase was observed forming a quasi-continuous network along the dendritic boundaries of α-Mg, Mg_3Gd, and LPSO phases. Lamellar LPSO phase was observed up to 23 at. % Li in the as-cast state and it is being changed by blocky LPSO at 30 at. % Li in the as-cast condition. Upon solutionisation treatment the quasi-continuous network of 15 at. % Li and 23 at.% Li alloys transformed into discontinuous structures having lamellar LPSO and Mg_3Gd particles along with the formation of solid solutions of α-Mg and β-Li alloys. However, 30 at.% Li still shows the quasi-continuous network even after the solutionisation treatment with reduced eutectic volume fraction and increased blocky LPSO phases. The hot extrusion process performed at

200 ℃ or 300 ℃ led to a refinement in grain size due to dynamic recrystallization and the crushing, breaking, and uniform dispersion of second-phase particles (Mg_3Gd and LPSO phases). A high yield strength of 270 MPa, ultimate tensile strength of 320 MPa and a tensile elongation of 18% with good strain hardening behavior was achieved in 15Li alloy extruded at a temperature of 200 ℃, which can be ascribed to the fine grain size (sub-micron grains), and uniform distribution of the Mg_3Gd phase and LPSO phases inside the matrix. 30Li alloy showed a good tensile ductility of 38%, albeit with a competent yield strength values of 201 MPa due to the presence of soft β-Li phase and partial distribution of Mg_3Gd particles inside the matrix.

3. Nanocrystalline $Mg_{98.82}Ni_{0.59}Gd_{0.59}$ and $Mg_{97.56}Ni_{1.22}Gd_{1.22}$ (at. %) alloys were prepared through a powder metallurgy route to achieve a high strength than the as-cast and extruded alloys. A fine crystallite size of 47 nm is achieved after 150 hrs of milling, along with solid solution formation by mechanical milling of Mg and NiGd powders. Hot compaction (550 ℃) and subsequent extrusion (500 ℃) process were carried out to achieve a good dense alloy rod. These processes led to the formation of nano second-phase particles like Mg_5Gd, Mg_2Ni, Gd_2O_3, and MgO uniformly distributed throughout the matrix. It was found that the second phase particles were more stable and resistant to coarsening even after processing at elevated temperatures and longer periods during compaction and extrusion processes. Similarly, the matrix grains exhibited a bimodal grain size distribution having grain size ranging from nanometer to sub-micron levels. Even after prolonged exposure to high sintering and extrusion temperatures, the grain sizes were still ultra-fine, attributed to the grain boundary pinning by secondary particles, especially MgO particles. Maximum compressive yield strength of 804 MPa and compressive total elongation of 3.8% was achieved and the enhanced strength levels are found to be due to the nano grain size and uniform dispersion of oxide and intermetallic phases. The dispersoids were uniformly distributed and acted as barriers for dislocation movement leading to Orowan strengthening. The strength dropped to 730 and 575 MPa with increased processing times at elevated temperatures, but the total elongation increased due to the formation of bimodal grain structure and dispersion of second phase particles inside the matrix.

Scope for Future Work

The current study shed some insight into the processing of high strength Mg alloys, where proper tuning of the microstructure results in the enhanced mechanical properties. Based on the observations made from the present investigation, a number of research problems can be envisioned. Some of them are listed below.

- More detailed characterization of microstructure in terms of their grain size, phase distribution and their influence on mechanical properties needs to be examined
- Performing further high-end characterization like HRTEM-HAADF to precisely identify the type of LPSO phases and their periodicity of arrangement of atoms, formed in these alloy systems.
- As Ni is an expensive element, relatively cheaper alloying element such as Cu on the generation of LPSO phase and subsequent influence on the mechanical performance of the alloys through both casting and powder metallurgy routes can be explored.
- Further experimentation to improve the limited ductility achieved in the powder metallurgy alloys can be a viable preposition by either tuning the grain size or by proper addition of other alloying elements such as Li.
- The current study only concentrated on the room temperature mechanical properties of the alloys. Other properties such as high temperature mechanical behavior, fatigue properties and damping ability etc. can be conducted on these Mg alloys to find their suitability for the real-world applications.
- The strength of the alloys can be further improved by performing severe plastic deformation processes like rolling, equal channel angular pressing (ECAP), multi-axial forging (MAF) etc. by refining the grain structure.
- Corrosion studies can be undertaken to understand their behavior under various corrosive media such as aqueous and brine solutions.

List of Publications

Journal Publications:

1. **Ravikanth Reddy, C.**, and B. Srinivasarao. *"Development of High-Strength Mg-0.5Ni-2Gd-xLi (x= 0, 1, 5, 10, 15, 25 at.%) Alloys with Long-Period Stacking Ordered Structure through Hot Extrusion."* Journal of Materials Engineering and Performance. 1-10 (2022) (**Impact factor: 2.099).**
2. **Ravikanth Reddy, C.,** K. Satya Prasad, and B. Srinivasarao. *"Microstructure and mechanical properties of Mg–Ni–Gd alloy synthesised by powder metallurgy."* Powder Metallurgy. 1-8 (2023). (**Impact factor: 2.228).**

International Conferences:

1. **C. Ravikanth Reddy and Bonta Srinivasa Rao,** Microstuctural study of high strength Mg-Ni-Gd alloys processed through Mechanical alloying and Hot extrusion, International Conference on Powder Metallurgy (PM-22), April-2022
2. **C. Ravikanth Reddy and Bonta Srinivasa Rao,** Fabrication of high strength Mg-Li alloys through hot extrusion, IIM-NMD-ATM, Nov-2019. **(Best Poster award)**
3. **C. Ravikanth Reddy and Bonta Srinivasa Rao,** Effect of LPSO on microstructure and mechanical properties of Mg-Li Alloys processed through Hot Extrusion and Rolling, ICAM5, NIT Warangal, Sept-2019.
4. **C. Ravikanth Reddy and Bonta Srinivasa Rao,** Development of high strength Mg-Ni-Gd alloys through mechanical alloying, ISMANAM, July-2019.
5. **Kiranchand GR, C. Ravikanth Reddy and Bonta Srinivasa Rao,** Development of high strength Mg-LPSO composite by powder metallurgy, IIM-NMD-ATM, Nov-2017**. (Best Poster award)**

About the author

The author was born in Kurnool, a town in Andhra Pradesh state, India on 22nd July 1988. After completion of his B. Tech in Mechanical engineering in the year 2010 from G. Pulla Reddy Engineering College (GPREC), Kurnool: He joined for his M. Tech in Metallurgy discipline at National Institute of Technology Tiruchirappalli, Tamilnadu, India in the year 2010. After successful completion of his M. Tech in the year 2012, the author worked as tenured assistant professor at G. Pulla Reddy Engineering College (GPREC), Kurnool for a period of 3 years before joining National Institute of Technology Warangal, Telangana, India to pursue his doctoral program. The author published several papers in international journals and presented his research work in international conferences.